TECHNISCHE UNIVERSITÄT MÜNCHEN
Institut für Luft- und Raumfahrt

Conceptual Design Methods of Electric Power Architectures for Hybrid Energy Aircraft

Patrick Christoph Vratny

Vollständiger Abdruck der von der Fakultät für Maschinenwesen der Technischen Universität München zur Erlangung des akademischen Grades eines

Doktor-Ingenieurs (Dr.-Ing.)

genehmigten Dissertation.

Vorsitzender:	Prof. Dr.-Ing. Volker Gümmer
Prüfer der Dissertation:	1. Prof. Dr.-Ing. Mirko Hornung
	2. Prof. Dr.-Ing. Eike Stumpf

Die Dissertation wurde am 21.06.2018 bei der Technischen Universität München eingereicht und durch die Fakultät für Maschinenwesen am 21.12.2018 angenommen.

Acknowledgments

This work was mostly performed during my time in the Visionary Aircraft Concepts group at Bauhaus Luftfahrt in Munich. I would like to thank my supervisor, Prof. Dr.-Ing. Mirko Hornung, for the opportunity and his long year support. I would also like to thank Prof. Dr.-Ing. Eike Stumpf for kind acceptance of the second assessment of this work. Furthermore, I would like to thank Prof. Dr.-Ing. Volker for his friendly chairmanship.

I would like to thank all my colleagues from Bauhaus Luftfahrt, in particular Philipp "Heinephipsie" Heinemann and Dr. Clèment Pornet, for the exceptionally working atmosphere and numerous inspiring discussions. My special thank is to to my second family Dr. Michael "Schmidty" Schmidt, Ulrich "Klinge" Kling and Sascha "Saschmeister" Kaiser from the Visionary Aircraft Concepts Group and Anne "Schusti" Schuster for their friendly and motivating support over the years. Their competent advice has significantly contributed to the success of this work.

Finally, I would like to thank my long-standing friends for their motivating support. My greatest thanks go to my mother, who, with her constant support has made a significant contribution to the successful completion of this work.

Patrick Vratny
Munich, March 2019

Abstract

Ambitious future emission and noise reduction targets, unveiled by the European Commission with the Strategic Research and Innovation Agenda (SRIA) and the National Aeronautics Space Administration (NASA) with their N+3 goals for the aviation industry, encourage new radical aircraft concepts. A potential solution to fulfill these targets has been identified as the introduction of hybrid and universally-electric aircraft with an entry into service (EIS) for 2035+. Those solutions have the potential to increase the overall vehicular efficiency and decrease the required mission energy demand. A key element of such concepts is the design of the electric part of the power train including the underlying electric systems architecture with regard to efficiency and mass. Current research focuses on the design and optimization of hybrid-electric power trains, as universally-electric aircraft are penalized for the excessive weight of existing designs. Several system and aircraft level studies are available for such concepts. In view of hybrid-electric power trains with different energy supply options, the serial and parallel hybrid-electric topologies are the most promising. Other studies focus on the optimization of the gas turbine performance as a main power supplier of a hybrid-electric power train. The characteristics of the entire electric systems architecture have been considered as a black box in the most cases with constant efficiency values over the entire flight envelope. Sizing impacts of the electric architecture with regard to different shaft power and rotational speed demands of the electric motor and different transmission voltages during design and off-design have been neglected. For an overall performance estimation and optimization of a hybrid-electric power train the level of detail of both contributors are important. Another aspect to be considered is the mechanisms by which the hybrid-electric propulsion system should be operated during the mission to generate the lowest CO_2 emissions.

For that purpose a method is presented here which allows for the sizing of the electric system architecture on a conceptual design level covering sensitivities with regard to design system shaft power, rotational speed, and transmission voltage in dependency of the involved components. Therefore, electric component models are developed covering those basic sensitivities with regard to mass and efficiency characteristics in design and off-design. The developed component models include the main devices such as electric motors, batteries and transmission cables, and also power electronics such as converters and inverters. These models also consider initial mass and power estimations for protection devices and the thermal management system. The thermal management system is a central part which requires additional power but keeps the main components in their operating temperature limits. Furthermore, to project different technology developments to cover the targeted EIS year, the models are sensitive to different material options such as high temperature superconducting (HTS) and different semi-conductor materials. As a case study, battery supplied electric architectures are investigated using direct current as a main transmission voltage type. This electric architecture is further studied in a potential discrete parallel hybrid-electric (DPH) topology. This topology utilizes a dual energy supply in form of a geared turbofan (GTF) powered by a conventional kerosene based gas turbine that is assisted by electric ducted fans (EDF) supplied by batteries. Those different thrust systems are completely decoupled from each other. As a reference platform a short to medium range aircraft is used accommodating for 180 PAX at 1300 nm.

Based on the developed electric models, a design space exploration was performed to determine optimal system parameters and technology options on an electric architectural level. This design space exploration included a variation of different design motor shaft powers and speeds as well as transmission voltages. Furthermore, different operational strategies were investigated, including constant voltage versus variable voltage systems. The conclusion of this approach was that the variable voltage system architecture utilizing HTS electric motors is the most efficient and mass optimized architecture. In a subsequent study this architecture layout served as a basis for combining the EDFs with GTFs to investigate the hybrid-electric propulsion system on system level. Based on the reference thrust requirements, different sizing scenarios were considered for differing degrees of power hybridization. In this study, several motor sizing options have been discussed. It was identified that for a DPH power train, the EDFs should be sized for the top-of-climb (TOC) power demand at take-off rotational speed with the equivalent TOC power. This motor sizing option results in the best utilization of the electric system with regard to mass and efficiency. At the overall aircraft level this motorization option has been analyzed for four different hybridization strategies such as operating the GTFs in all flight phases in their optimal thrust specific fuel consumption point or operating the EDFs at constant maximum power. The objective of this study was to identify the most suitable mission hybridization strategy that offered the highest potential to decrease the required fuel burn, mission energy and generated CO_2. The results suggest that no single strategy offers an optimal solution but instead depending on the objective function different hybridization strategies should be recommended. For example, if an aircraft aims to generate the lowest CO_2 emissions for renewable electric energy, the strategy to operate the EDFs at a constant rate of maximum power is the best hybridization option. However, all strategies had in common that the hybrid-electric aircraft is heavier and requires more total mission energy than the corresponding non-hybrid-electric reference aircraft.

The overall conclusion out of the presented approach is that a pure hybridization on the power train level using a battery supplied hybrid-electric architecture with the considered technology assumptions offers insufficient overall vehicular efficiency to fulfill the environmental targets defined in the SRIA. For that reason, alternative integration options on overall aircraft level have to be considered which enable the new flexibility of such propulsion systems.

Contents

List of Figures

List of Tables

Nomenclature

List of Symbols

A	m^2	Area
a	$\frac{m}{s}$	Speed of Sound
α	deg	Angle
α	V	Breakdown Voltage
B	T	Magnetic Flux Density
C	Ah	Capacity
C	F	Capacitance
c_P	$\frac{J}{kg \cdot K}$	Specific Heat
D	m	Diameter
DCR	Ω	Direct Current Resistance
DCy	-	Duty Cycle
DR	-	Diameter Ratio
δ	m	Air Gap
E	Wh	Energy
E	$\frac{N}{m^2}$	Young’s Modulus
ϵ	-	Relative Dielectric Permittivity
ESR	Ω	Equivalent Series Resistance
f	Hz	Switching Frequency
F	N	Net Thrust
γ	-	Overshoot Tolerance
GR	-	Gear Ratio
h	m	Height
H	$A \cdot m^{-1}$	Magnetic Field Strength
I	A	Electric Current
J	$\frac{A}{m^2}$	Electric Current Density
J	$\frac{kg}{m^2}$	Moment of Inertia
k	-	Correction or Safety Factor
κ	-	Shape Factor
K_V	$\frac{rad}{s \cdot V}$	Motor Voltage Factor
L	H	Inductance
l	m	Length of Cable or Coil

LIR	-	Inductor Current Ratio
n	-	Number of Components
n	min^{-1}	Rotational Shaft Speed
n_R	-	Redundancy factor
N	-	Number of Windings in a Coil
η	-	Efficiency
ν	$\frac{Ns}{m^2}$	Dynamic Viscosity
m	kg	Mass of a Component or System
Ma	-	Mach Number
μ	-	Permittivity
ω	Hz	Rotational Speed
P	W	Electrical or Mechanical Power
p	-	Number of Pole Pairs
$\mathit{\Phi}$	Wb	Magnetic Flux
ϕ	-	Power Factor
Q	Nm	Torque
R	$\mathit{\Omega}$	Electrical Resistance
$R_{p,0.2}$	$\frac{N}{m^2}$	Maximum Yield Strength
r	m	Radius
ρ	$\frac{kg}{m^3}$	Material Density
$\bar{\rho}$	$\frac{kW}{kg}$	Specific Power
σ	$\frac{N}{m^2}$	Available Shear Stress
SOC	-	State-of-Charge
t	s	Time
t	m	Thickness
T	s	Period
T	K	Temperature
τ	$\frac{N}{m^2}$	Shear Stress
$\mathit{\Theta}$	-	Modulation Index
TSP	-	Thrust Split
TSPC	$\frac{W}{N}$	Thrust Specific Power Consumption
U	V	Voltage
V	m^3	Volume
v	$\frac{m}{s}$	Speed
$\dot{V}$	$\frac{m^3}{s}$	Volumetric Flow
w	m	Width

List of Subscripts

Aero	Aerodynamic
Air	Air
AirGap	Rotor Air Gap
Arm	Electric Motor Armature

Bat	Battery System Level
Bearing	Bearing
Boost	Boost Converter
Buck	Buck Converter
C	Collector/Capacitor/Conductor
c	Critical
Cables	Cable related
Cell	Battery Cell Level
Coil	Coil
Comp	Component
Cond	Conduction
Conductor	Cable Conductor
Cont	Controller
Conv	Converter
Cool	Cooling System
Core	Stator Core
Corr	Corrected
Cryo	Cryooolin‌g System
D	Diode
Design	Design Point
E	Emitter
Elec	Electric System
End	End of Simulation or Component
F	Forward
Fan	Fan related
FCM	Fault Current Multiplier
Fuel	Fuel
GB	Gear Box
Hydr	Hydraulic
i	Inner/Internal
I	Electric Current related
In	Input
Ind	Inductor
Ins	Insulation
Inv	Inverter
Iron	Iron
L	Loss
Length	Component Length
load	Load
Mag	Magnet
max	Maximum Value
Mot	Electric Motor
Nom	Nominal

norm	Normalized
OC	Open Circuit
Off	Off State
On	On State
Opt	Optimum
Out	Output
Parallel	Parallel Connection
Phases	Phases
Power	Power
Prop	Total Propulsion System
prop	Propulsive
PS	Power Switch
Ref	Reference Point or Value
Rel	Relative
Req	Required
ripple	Voltage or Current Ripple
RMS	Root Mean Square
Rot	Rotor
S	Safety
SC	Semi-Conductors
Sec	Secondary
Series	Series Connection
Serv	Services
Shaft	Shaft
Sheath	Sheath
sink	Sink
Slot	Stator Armature Slot
Stage	Gear Box Stage
Stator	Electric Motor Stator
Stray	Stray Load
SW	Switching
T	Terminal
Target	Target Point or Value
Tech	Technology
Teeth	Teeth
th	Thermal Heat
Tr	Transistor
Trans	Transmission
Tot	Total
V	Voltage related/Void

List of Acronyms

AC Alternating Current

ACARE Advisory Council for Aviation Research and Innovation in Europe

AEA All-Electric Aircraft

AEO All Engines Operative

ASM Asynchronous Motor

ATLeR Aircraft Top Level Requirements

BCU Battery Control Unit

CCE Composite Cycle Engine

CIPH Cycle Integrated Parallel Hybrid

CO_2 Carbon Dioxide

DC Direct Current

DCR Direct Current Resistance

DPH Discrete Parallel Hybrid

EASA European Aviation Safety Agency

EDF Electric Ducted Fan

EIS Entry-Into-Service

EMCB Electromechanical Circuit Breakers

EMF Electromagnetic Field

EPS Energy and Power Supply

ESAR Energy Specific Air Range

ESR Equivalent Series Resistance

EU European Union

EV Electric Vehicle

EWIS Electrical Wiring Interconnection System

FAA Federal Aviation Administration

FoM Figure of Merit

GHG Global Greenhouse Gas Emissions

GR Gear Ratio

GTF Geared Turbofan

HCB Hybrid Circuit Breaker

$\mathbf{H}_E$ Degree of Energy Hybridization

$\mathbf{H}_P$ Degree of Power Hybridization

HTS High Temperature Superconducting

IATA International Air Transport Association

ICE Internal Combustion Engine

IGBT Insulated Gate Bipolar Transistor

LIR Inductor Current Ratio

MEA More Electric Aircraft

MIPH Mechanical Integrated Parallel Hybrid

MOSFET Metal-Oxide Semi-conductor Field Effect Transistor

MTOW Maximum Take-Off Weight

NASA National Aeronautics Space Administration

NdFeB Neodymium-Iron-Boron

$\mathbf{NO}_x$ Nitrogen Oxides

OBI One Battery Inoperative

OEI One Engine Inoperative

OMI One Motor Inoperative

PM Permanent Magnets

PMAD Power Management and Distribution

PMSM Permanent Magnet Synchronous Motor

PS Power Switch

PWM Pulse Width Modulation

Si Silicon

SiC Silicon-Carbide

SOA State-of-the-Art

SOC State-of-Charge

SRIA Strategic Research and Innovation Agenda

SRM Switched Reluctance Motor

SSCB Solid-State Circuit Breakers

SSPC Solid-State Power Controllers

TO Take-Off

TOC Top of Climb

TSFC Thrust Specific Fuel Consumption

TSP Thrust Split

TSPC Thrust Specific Power Consumption

UEA Universally-Electric Aircraft

UML Unified Modeling Language

VSI Voltage Source Inverter

1 Introduction

The International Air Transport Association (IATA)[1] forecasts that the average annual growth rate of air traffic is about 4.8% per year until the year 2030. The two main aircraft manufactures Airbus [2] and Boeing [3] are also expecting an increased growth of air traffic in the next decades. This continuously increasing aircraft demand would in turn amplify the aviation generated Global Greenhouse Gas Emissions (GHG). According to the European Union (EU), the transportation sector accounts for 28% of the total European CO_2 emissions generated [4]. From this 28%, the civil aviation sector was responsible for 13% of the generated CO_2 emissions in Europe in 2016 and 3.6% of the total generated CO_2 emissions [4]. The aviation industry has to adjust for the increased needs of air transport with additional aircraft. It is important to take into account the negative impact this will have on emissions, especially, with regard to Carbon Dioxide ($\mathrm{CO_2}$) and Nitrogen Oxides (NO_x).

Similar trends are expected in other regions such as Northern America and Asia. Several organizations such as the EU and the National Aeronautics Space Administration (NASA) have unveiled challenging emission targets to reduce the generated CO_2, NO_x as well as perceived noise levels for future transport aircraft. For example, the Advisory Council for Aviation Research and Innovation in Europe (ACARE) has summarized their emission targets in the Strategic Research and Innovation Agenda (SRIA) [5] aiming at a reduction of 60% of CO_2 kg per passenger nautical mile for the year 2035. This should be reached by reducing the overall energy consumption due to improvements in airframe and propulsion needs (both contributing each to 30%) including customer power needs, adaptations in air traffic management and infrastructure and airline operations (based on the datum year 2000 [5]). For an Entry-Into-Service (EIS) year of 2050 the CO_2 kg per passenger nautical mile should be further decreased to 75% [5]. The different targets are summarized in Table 1.1.

The improvements performed on an aircraft level in recent years have shown that the main contributor and performance lever for fuel burn reduction is the energy and propulsion system. This can be also recognized with the new aircraft derivatives of the two big aircraft manufacturers, Airbus with the A320 NEO (new engine option) and Boeing with the B737 MAX. For example, the A320 NEO is equipped with the Geared Turbofan (GTF) PW1000G, which allows for fuel saving potentials of up to 15% [6]. On an airframe side there are currently some incremental improvements being performed with the introduction of carbon fiber reinforced polymer, as shown with the B787 and the A350, or the introduction of sharklets at the A320 or the split scimitar winglet on the B737 MAX [7]. The propulsion system seems

Table 1.1: Timely specified emission reduction targets by the ACARE with reference year 2000 [5]

Goals and Key Contributions	**2020 (Vision)**	**2020 AGAPE**	**2020 SRIA**	**2035 SRIA**	**2050 SRIA**
CO_2 objective vs 2000	-50%**	-	-	-	-75%**
CO_2 vs 2000 (kg/pass km)*	-50%	-38%	-43%	-60%	-75%
Airframe energy need (Efficiency)	0.75	0.85	0.80	0.70	0.32
Propulsion and power energy need (Efficiency)	0.80	0.80	0.80	0.70	
ATM and Infrastructure	0.88	0.95	0.93	0.88	0.88
non Infrastructure-related Airlines ops	0.96	0.96	0.96	0.93	0.88

* comparison with same transport capability aircraft and on a same mission in term on range and payload

** ACARE 2020 and ACARE 2050 High Level Goals for airframe, engine, systems and ATM/operations

also to be a potential candidate for further overall vehicular improvements for future transport aircraft. Inspired by the automotive industry, which is confronted with similar emission reduction targets, hybrid-electric and full electric vehicles are a promising option to tackle the targets specified in Table 1.1. With the advances made over the last decades in electric component technologies, propulsion options are becoming more alluring to the aviation industry. One characteristic of hybrid-electric vehicles is the separation of Energy and Power Supply (EPS) and power consumers (e.g. motors), which offers new degrees of freedom integrating a propulsion system within the airframe. Hybrid-electric propulsion systems can be also treated as a potential key technology, which can efficiently enable other technologies (e.g. boundary layer ingestion)[8]. Such intentions may be already implied in the SRIA targets, where the energy savings for propulsion and airframe are a combined target of 68%.

1.1 Challenges of Disruptive Power Trains

Aircraft design is a multi-disciplinary design optimization between the structural, aerodynamic and propulsive disciplines to optimally fulfill a certain transportation task. Focusing on the propulsive discipline, the last decades have already shown progress in increasing the propulsive and core efficiencies. Conventional kerosene supplied power plants with the classical power plant architecture consisting of axial compressors, combustion chambers and turbines are slowly reaching the Carnot efficiency limit [9], the conversion of chemical into mechanical power. To exceed this limitation of evolutionary component developments, new architectures will be required. Also new and novel arrangements of the propulsion (sub-)components will be necessary to accomplish advanced engine architectures. One possibility to increase propulsive efficiency is to increase the bypass ratio of the engine, defined as the ratio of the airflow of the fan to the airflow of the core engine. This option results in bigger fan diameters [10]. In past designs of such engines, the fan was directly powered by the low pressure turbine, which implies that with increasing fan diameter, the rotational speed (and in turn the low pressure turbine speeds) had to be reduced to meet maximum tip speed requirements. This resulted in larger dimensions of low pressure turbines. The introduction of a gear box system between the low pressure spool and the power shaft of the fan allows for a decoupling of the rotational speeds of the turbine and the fan. Nevertheless, higher bypass ratios come with airframe installation penalties, such as higher nacelle drags [10] or larger landing gear struts [11] damping the increased engine performance. Other progress is performed via the introduction of new material technologies, which allowed for higher burner exit temperatures and increased the useful enthalpy of the thermodynamic cycle. However, with higher temperatures NO_x emissions increased [10]. Therefore, other options are forcing the implementation of heat exchangers to recover heat losses from the turbine station and return it to a previous cycle station. Here, the temperature levels stay the same, but due to the heat recovery the compressor power can be reduced [10]. Also new cycle options are investigated, such as the potential of the Composite Cycle Engine (CCE)[12]. The CCE implements a piston engine between the compressor stages of the conventional engine, which increases the temperature and pressure level [12]. These concepts have the advantage that they are using technologies that are already well known in the aviation industry, but are still limited by the Carnot efficiency. To overcome the problem of the Carnot efficiency, the usage of new types of energy with higher exergetic energy can be a solution. This form of energy could be, for example, electric energy stored in batteries. New energies offer new degrees of freedom with regard to overall system optimization. For that purpose, hybrid-electric (a combination of at least two different energy sources) and universally-electric vehicles are of interest. These power train options can significantly improve the overall system efficiency by using higher exergetic energy sources.

Airborne vehicles operate at different flight altitudes, air densities and temperature levels. One big challenge of linking an electric system with a propulsor (fan or propeller) is the power lapse of the propulsor in decreasing air density (or increasing flight altitude), which an electric system is not showing, in the first instance. In a conventional power plant system the propulsor and the air-breathing core engine show a complementary power lapse over the flight altitude [13]. Therefore, the performance matching of the sizing points between the fan and the core engine can be tailored in a more optimal way. An electric system can theoretically deliver maximum power independently from the air density. For an optimal system design, the overall system trade-offs have to be identified with respect to the main design drivers satisfying the Aircraft Top Level Requirements (ATLeR).

Another challenge of electric aircraft concepts is the provision of the required power. In a conventional propulsion system the power is supplied in the form of kerosene, which is pumped from fuel tanks via fuel pipes to the combustion chamber of the power plants. This fuel system is independent of the design thrust and design power of the engines, respectively, and the mass is only determined by the required volume or mass flow of the kerosene. The pressure loss within the fuel pipes is negligible. Torenbeek proposes that the fuel system mass can be estimated with the stored fuel volume [14]. In hybrid-electric or universally-electric system architectures an electric transmission system or Power Management and Distribution (PMAD) system is much more complex in design than a conventional fluid based transmission system. Such a PMAD system, which connects a power source with a power consumer, consists of several components such as converters, inverters or cables. These components are strongly dependent on the design power, which has to be transmitted, and influences the overall system mass as well as its efficiency. In some ways, these negative impacts can be counteracted via higher transmission voltages but, in the case of aerospace vehicles operating in high altitudes, those higher voltages can cause lightning arcs due to the lower air density. This effect was discovered and investigated by Paschen and is described in detail in Paschen's law [15].

New types of methods are required to cover the new propulsion systems of aircraft preliminary sizing approaches. Conventional semi-empirical methods according to Torenbeek [14] or Raymer [16] are based on statistical data of kerosene supplied power plants, where mass is reduced during the flight as fuel is burned. Hybrid-electric, where a smaller portion of the fuel will be burned, or even universally-electric aircraft, where no mass is lost during the mission, require new methods to cover these aspects. Stückl [17, 18] or Pornet [19–21] have developed models for first investigations to deal with this kind of technology during the aircraft conceptual design phase. An open aspect of such hybrid-electric architectures, mainly of the electric architecture part, is the modeling of the masses and (off-design) performance for different types of technologies and a broad range of power demands.

1.2 Research Objectives

Based on the described challenges, when introducing a hybrid-electric power train with a secondary energy source for propulsion, the following research objectives occur:

- *What are optimal components and technologies for high power electric architectures?*
  For future (hybrid) electric transport aircraft it is important to identify the most suitable components and technologies for specific power and voltage classes. This also includes normal conducting and advanced conducting systems.

- *What are design drivers on system level?*
  Within an electric power train there are different components involved to ensure a redundant transfer of power from sources to loads. This thesis should give a further insight to how these components can be optimally linked together and the impact an exchange of a component or the choice of the system voltage has on the overall system performance and mass.

- *What is the best hybridization strategy to operate a hybrid-electric system in off-design?*
  After the identification of the best design point how the individual components are operated during the mission must be identified. This includes aspects such as an optimum operation of the gas turbine and/or the electric system.

- *What is the system impact when optimizing an electric power train at the aircraft level?* An optimization must be performed at both system and overall aircraft level. A central point is the identification of driving parameters of the electric system architecture. A key objective is to identify if an efficiency or a mass optimized electric system enables a higher overall vehicular efficiency.
- *Can a pure hybridization on power train level fulfil the SRIA targets?* The main focus of this research question is to identify if a hybridization on pure power train level including an optimized operational behavior is able to satisfy the SRIA goals or if aerodynamic or structural improvements are necessary, which this new power train may enable.

1.3 Organization of Thesis

To achieve the results mentioned in the previous section, the organization of the thesis is structured as follows:

- *State-of-the-Art of Hybrid-Electric Aircraft:* In Section 2 the current State-of-the-Art (SOA) of hybrid-electric as well as universally-electric propulsion systems and aircraft concepts is outlined. This section includes a recapitulation of existing modeling approaches. It gives also an overview of current certification options and which gaps still exist to evaluate a hybrid-electric power train. With the gained knowledge the research questions are refined.
- *Sizing Methods for Electric Components:* Section 3 describes possible component candidates and the necessary modeling approach for each required electric component, which can be suitable for high power application. The models cover aspects for mass and efficiency, including a first order sensitivity with regard to the system voltage.
- *Sizing Methods for Hybrid-Electric Power Architecture:* In this section the general options of a (parallel) hybrid-electric architecture are discussed. This includes the arrangement of the previously developed models to a full electric power architecture, covering the current certification aspects. Also the conventional part of the gas turbine will be discussed. In the next step, the suitable assessment parameters or Figure of Merits (sFoMs) will be defined. This section outlines which options are possible to arrange the different components to fulfill a certain transportation task. The potential design space will be explored with the help of a morphological box and the most promising architectures will be assessed according to the defined FoM. The main contribution of this thesis is to identify optimal system parameter trends and proposals for mass and efficiency optimized systems.
- *Application to Hybrid-Electric Power Trains:* Section 5 deals with the assessment of the most promising architectures on overall system as well as aircraft level from the previous section, which is covered with trade factors. After the description of the

reference platforms including critical sizing scenarios, the hybrid-electric architectures are sized for different degrees of power hybridization. This section includes the results of the solely battery supplied electric power train, the mass and performance when linking the architecture with a propulsor and, finally, the hybrid-electric power train performance.

- *Discussion:* The generated results for the most promising hybrid-electric power train will be critically discussed in Section 5.4. This includes the impact of critical components and parameters and how those assumptions influence the overall aircraft performance. The evaluation will be performed with the help of sensitivity studies.
- *Conclusion and Outlook:* The last Section 6 reviews the developed approach of sizing and performance of electric system architectures in a hybrid-electric power train environment. A key element is the evaluation, if the research questions set in Section 1.2 are achieved. Furthermore, additional open issues will be discussed, which require a deeper analysis in future work.

2 State-of-the-Art of Hybrid-Electric Aircraft

In this section, an overview of current methods and concept studies are given with regard to hybrid energy power trains for aircraft applications. Hybrid energy here is defined as the combination of at least two controllable, different energy sources which are able to supply the power train of a vehicle. Due to the high set of possible combinations that hybrid-energy concepts offer, the design space for the following considerations will be limited to chemical energy storage, such as kerosene and electrochemical storage devices, such as batteries.

2.1 Overview of Hybrid and Universally-Electric Power Trains

Hybrid-electric and universally-electric vehicles are a promising solution to reduce GHG emissions by optimizing the operating area of the individually involved components. Such power trains are already in service in ground-based vehicles, primarily in the automotive sector where several variants of hybrid-electric and fully electric cars are available [22]. Silvas et al. [22] summarized different topologies used in ground based vehicles. In the automotive sector, the degree of electrification is classified by four main types depending on the purpose for which the electric system is intended. These four types are defined as micro, mild, full and plug-in hybrid vehicles [23]. In *micro-hybrid* vehicles the electric system is not directly assisting the power shaft of the wheels. This system is used only to start the engine and to recuperate the braking energy. The *mild-hybrid* topology[1] allows for a support of the Internal Combustion Engine (ICE) by the electric system. This electric system is not capable to power the entire vehicle. The third hybrid category of ground-based vehicles is the *full hybrid*, where the electric system is sized to power the entire vehicle. This category also includes the standard known parallel and serial hybrid topologies. According to [24] cars are normally arranged in the parallel hybrid topology, where an ICE is in direct traction mode and is assisted by a battery supplied electric motor. Looking to higher power classes, like in electric busses or even ship propulsion systems [25, 26], the serial topology dominates. For

---

[1] In this thesis it will be differed between topology and architecture. Topology describes the arrangement of the components on a more global level, while architecture will already cover aspects how the components are connected in a redundant and fault tolerant way.

busses, this topology type offers the possibility of energy harvesting during braking actions. This energy is normally used to recharge a battery.

In the aviation sector, the research focus aims for an increased electrification of the subsystems by eliminating pneumatic and hydraulic systems. Such an approach has been demonstrated with the Boeing B787 [27]. This electrification option would most likely represent a micro-hybrid electric vehicle. In contrast to ground-based (hybrid) electric vehicles, the defined electrification classifications in aircraft design have not succeeded. For example, the B787 is classified as More Electric Aircraft (MEA) [28]. The bleed-air system of the B787 has been replaced by an electric one and one hydraulic circuit is supplied by electric power instead of a hydraulic pump mounted at the engines [27]. If all pneumatically and hydraulically powered systems are replaced by an electrical complementary system (e.g. only mechanical power off-takes at the engines) it is defined as All-Electric Aircraft (AEA). The main purpose for this type of electrification is to increase the overall system efficiency. For this kind of "hybridization" different studies have investigated optimal system architecture designs linking different loads in an efficient, redundant and mass optimized way [29].

The next step after the electrification of the subsystems is performed by the electrification of the power train. In the ultra-light or general aviation sector, representing the low power (low kilowatt) system aircraft class, several flying aircraft have been achieved. The first reported maiden flight of an entire electric aircraft was performed in the early seventies. Fred Miltitky electrified the light-plane type HB-3 of the manufacturer HB-Flugtechnik with a 10 kW electric motor and nickel-cadmium batteries, which allowed for an overall flight time of nine minutes [30]. In general, the electrification of low power aircraft (as they appear in the general aviation segment) is, from current technology standards, the most promising use case. In the last years several manufacturers offered Universally-Electric Aircraft (UEA) supplied solely by batteries such as the Pipistrel Taurus G4 [31], PC-Aero Elektra One [32], Airbus E-Fan [33] or Siemens Extra 330LE [34]. In the area of transport aircraft representing higher power classes only conceptual studies have been performed. These concepts cover turbo-electric, hybrid-electric and UEA power trains. The VoltAir [17] and the Ce-Liner [35] are representatives of UEA concepts. Hybrid-electric and turbo-electric aircraft studies are performed by Pornet et al. [20] with the BHL Twin-Fan and Quad-Fan [21], Bradley et al. [36] with the Boeing SUGAR Volt study and Armstrong et al. [37] with the NASA N+3 blended wing body concept.

According to the multitude of different options that electrified power trains offer, the EU has published a definition how hybrid-electric power train can be defined [38]:

> *"'hybrid electric vehicle' means a hybrid vehicle that, for the purpose of mechanical propulsion, draws energy from both of the following on-vehicle sources of stored energy/power:*
>
> - *a consumable fuel,*
> - *an electrical energy/power storage device (e.g. battery, capacitor, flywheel/generator, etc.)"*

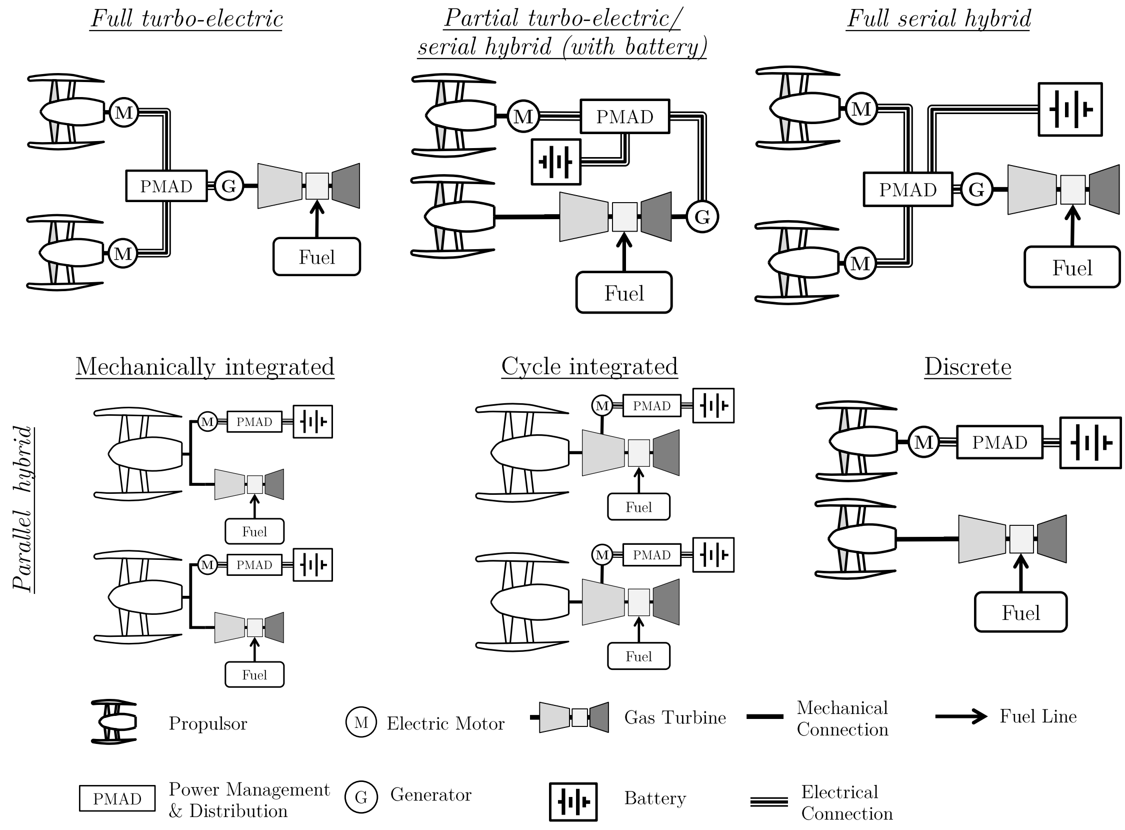

Figure 2.1: Topologies of hybrid-electric power trains (based on [39])

Based on this definition, the different topologies determined with this analysis of all different vehicles and concepts can be clustered in three main topologies that may be used to power an aircraft. In case of hybrid-electric power trains, those topologies can be classified in the categories serial, parallel and serial-parallel hybrid as shown in Figure 2.1. The main difference between these topologies is the type of power transmission. A turboshaft power plant converts partially or entirely its mechanical power with the help of a generator into electric power to supply a thrust producing device. If no second energy source is used, this topology is referred to a **turbo-electric** topology as shown by [37]. According to the definition from the EU, this topology type is not a representative of a hybrid-electric power train due to the missing second energy type. NASA concept STARC-ABL [40] or DisPURSAL [41] developed a variant called *partial turbo-electric* where only a portion of the gas turbine power is converted into electrical power. The addition of a battery to assist this topology is referred to a (partial) **serial hybrid** topology. The advantage of a turbo-electric or even serial hybrid-electric topology is that power consumers (e.g. propulsors) are completely mechanically decoupled from power sources. In case of the turbo-electric topology the electric system acts as electric “gear box” to be able to variably control this decoupling. This enables an optimum operation of those sources with regard to efficiency within their individual operating envelopes. The disadvantage of this topology is that the entire electric transmission chain has to be sized for at least the total propulsive power and that the optimized and more efficient operation of the power sources have to (over-)compensate the efficiency losses caused by the transmission chain. Another special variant of an electric power train beside the turbo-electric is the universally-electric topology for UEA. UEA means in this context that the entire power for all systems including the propulsion system is supplied by electric means (i.e. battery or fuel cells). This nomenclature was introduced by Isikveren et al. [35], while the nomenclature of AEA only refers to the subsystem level. For this power train several detailed system and aircraft level assessments have been performed [18, 35]. The advantage of the UEA power train is that it offers inner efficiencies higher than 90% for battery supplied architectures [35]. The disadvantages of these concepts are the high mass penalties caused by the battery system, which overcompensate the increased power train efficiencies. Even with radical assumptions for the battery system, mission ranges up to 1000 nm are challenging [18, 35].

The second type of topology is the **parallel hybrid** topology. This is categorized by the capability that the electric system and the ICE or gas turbine can deliver mechanical power at the same time. The parallel hybrid topology offers high flexibility in combination of different components of the total power train. The most common is the *Mechanical Integrated Parallel Hybrid (MIPH)*. In this configuration, the power shaft of an ICE is mechanically coupled with the propulsor and an electric system assists the power plant on the same power shaft or coupled via a mechanical gear box system. The advantage of this variant is that the electric part does not need to be sized for the entire propulsive power. The disadvantage is that the gas turbine cannot be operated independently of the propulsor. Furthermore, the amount of supplied electric power is strongly coupled with the operating point of the power plant during operation considering the operational margins of the involved turbo components. Another type of the parallel hybrid topology is the *Cycle Integrated Parallel Hybrid (CIPH)* proposed by Schmitz [42] and investigated in more detail by Vratny et al. [43]. In this configuration the electrification does not directly assist the power shaft of the engine but electrifies parts or the entire compressor stages which are normally powered by the turbine. This decoupling of the compressor and the turbine section allows for an independent operation of each other and, furthermore, offers new degrees of freedom when controlling a power plant. The amount of electrification cannot be chosen arbitrarily similar to the MIPH. Considering all sizing points within the flight envelope, some constraints like surge and choke margin of the compressor or the installed electric power can limit the operational behavior [43].

A potential third type of a parallel hybrid is the Discrete Parallel Hybrid (DPH) topology defined by Schmitz [39] and investigated in detail on aircraft level by Pornet [19]. In this configuration, a conventional (pure kerosene supplied) GTF and a fully Electric Ducted Fan (EDF) are operated side by side. Both systems are supplied by their dedicated power sources and are not coupled. Therefore, these systems can be controlled independently of each other within their individual operational limits. This allows for an optimal degree of hybridization in each flight phase. The disadvantage of this kind of configuration is that it requires at least three propulsors, if an asymmetric[2] distribution needs to be avoided as shown by Isikveren et al. [44].

Based on the analyzed topologies a (hybrid) electric topology consists in general of three main contributors as shown in Figure 2.2. The *EPS* is responsible for the conversion of the stored energy into usable power and can be a gas turbine and/or a battery system. The *PMAD* system has the function to transfer the generated power of the EPS in a safe and redundant way. This is performed via various components such as cables, switches, fuses, converters and inverters. The third main contributor is the *power converter* system, which includes all systems necessary to convert one power type to another. This system includes the electric motors responsible for the conversion of electrical into mechanical power, the thrust producing devices as well as the necessary thermal management system.

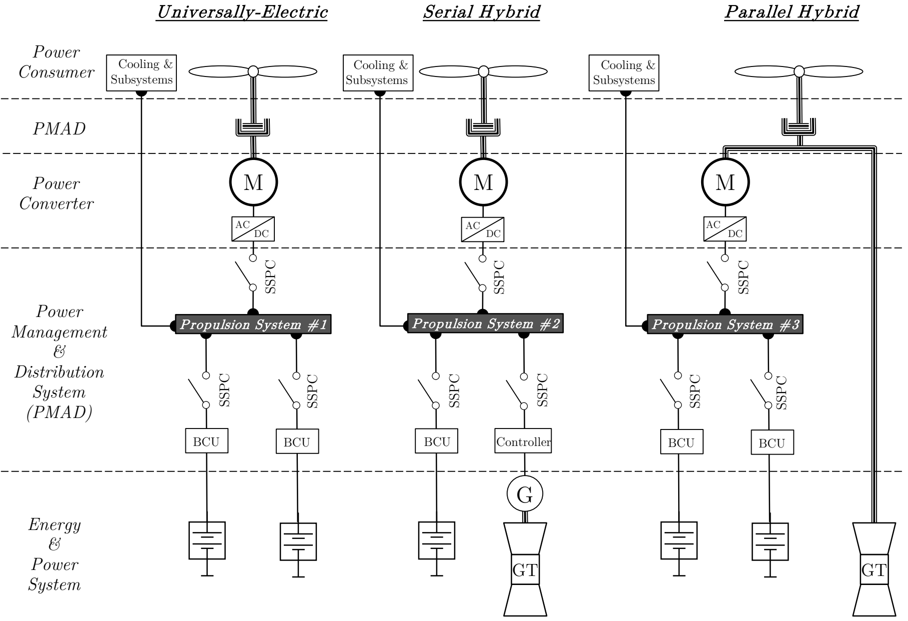

Figure 2.2: Typical components of universally-electric and hybrid-electric architectures

2.2 Current Design Methods for Hybrid-Electric Power Train Systems

In general, (hybrid) electric power trains can be described via two parameters which cover all possible combinations proposed by Lorenz et al. [24]. The first descriptor defined in Equation (2.1) is the Degree of Power Hybridization (H_P)

$$H_P = \frac{P_{Elec,Shaft,Tot}}{P_{Elec,Shaft,Tot} + P_{GT,Shaft,Tot}} \tag{2.1}$$

---

[2] Asymmetric means in this case a conventional power plant on one wing side and an electric powered system on the other wing side.

The H$_P$ is the ratio of the total installed electric motor shaft power, $P_{Elec,Shaft,Tot}$, to the total installed shaft power. A H$_P$ of 0 means that the power train is powered by conventional (mechanical) power conversion, and a H$_P$ of 1 means that the power transmission is completely performed electrically, like in the case of turbo-electric, serial hybrid or universally-electric topologies.

The second parameter beside the H$_P$ is the Degree of Energy Hybridization (H$_E$) defined in Equation (2.2) proposed by [24, 45]

$$H_E = \frac{E_{Elec}}{E_{Elec} + E_{Fuel}} \tag{2.2}$$

This descriptor is defined as the ratio of the installed electric energy, E_{Elec}, to the total installed energy including fuel in the form of chemical energy, E_{Fuel}. Analogous to H$_P$, a H$_E$ of 0 means that no electric energy is stored on board of the aircraft, which is equal to a conventional or a turbo-electric power train. A H$_E$ of 1 means that the entire energy is stored in form of electric energy (e.g. in batteries), which is the case for a UEA. This descriptor is also an important parameter for the optimization of the systems architecture at overall aircraft level. H_E implicitly depends on the electric transmission efficiency, η_{Elec}, as well as the utilization of the electric system during the mission. By combining the parameters H$_P$ and H$_E$ all possible (hybrid) electric topologies can generically be described, as summarized in Table 2.1. A drawback of this general approach is that all topologies can be covered, but not be uniquely identified, because the parallel and the partial serial hybrid topology are within the same value range. However, the parallel and partial serial hybrid-electric topologies offer the highest degrees of freedom for the design exploration according to Table 2.1.

Table 2.1: Parameter range for the different (hybrid) electric topologies

Topology	**Degree of Power Hybridization H_P**	**Degree of Energy Hybridization H_E**
Conventional	0	0
Partial Turbo-Electric	$0 < H_P < 1$	0
Turbo-Electric	1	0
Serial Hybrid	1	$0 < H_E < 1$
Parallel Hybrid	$0 < H_P < 1$	$0 < H_E < 1$
Partial Serial Hybrid	$0 < H_P < 1$	$0 < H_E < 1$
Universally-Electric	1	1

These hybrid-electric topologies are graphically represented in the hybrid-electric chart Figure 2.3 based on Lorenz et al. [24]. This figure includes aircraft representatives of hybrid-electric topology qualitatively marked with the parameters H_E and H_P.

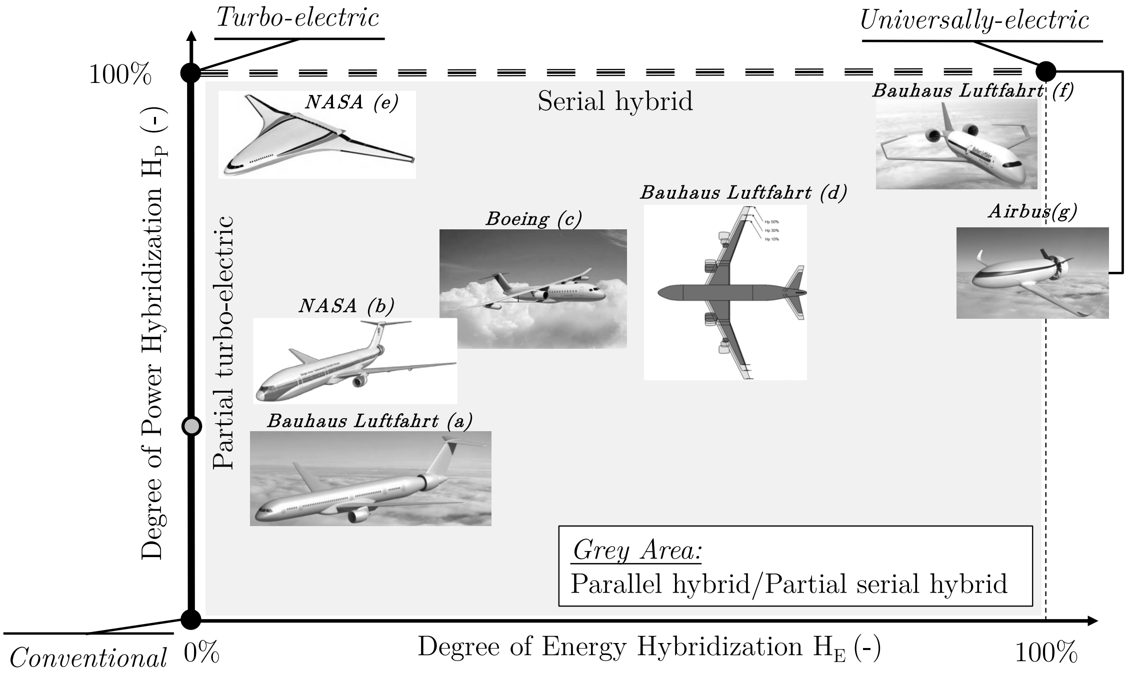

Figure 2.3: Hybrid chart with different potential turbo-electric, universally-electric and parallel hybrid-electric architectures; (a) Bauhaus Luftfahrt Dispursal [41], (b) NASA Starc-ABL [40], (c) Boeing Sugar Volt [36], (d) Bauhaus Luftfahrt Quad-Fan [21], (e) NASA N3-X [46], (f) Bauhaus Luftfahrt Ce-Liner [35], (g) Airbus VoltAir [17]

Based on the hybrid-electric topology and its intended purpose, the required electric power demand can be determined for the electric system sizing. In current aircraft conceptual designs, the electric system is part of the general subsystems including hydraulics, pneumatics and auxiliary power systems [14][16]. According to Torenbeek, the electrical system mass is a function of the cabin volume of the fuselage only [14]. The efficiency of such a system is not covered. Therefore, extensions of existing and even new methods are required to cover mass and efficiencies of electric power architecture used to power an aircraft. As described in the previous section, the implementation of an electric power train for aircraft propulsion is a new research topic. However, in other industries such as the marine sector electric power trains have been already investigated and are in a similar power class. Skinner et al. [47] have analyzed serial hybrid topologies in more detail for the marine and submarine sector. Rucker [25] has performed a study for a 16 MW permanent magnet generator and inverter combination for a turbo-electric ship propulsion system.

Depending on the numerous variants of the design parameters H_P and H_E, the architecture design and performance offer different properties and application scenarios. The most common way to estimate the mass of single components or component assemblies, such as the PMAD system is performed with the help of the specific power, $\bar{\rho}$, and the corresponding design power of the component, $P_{Comp,Design}$, as demonstrated with Equation (2.3) [17, 19, 35, 48, 49]

$$m_{Comp} = \frac{P_{Comp,Design}}{\bar{\rho}} \tag{2.3}$$

The system efficiency of the electric transmission chain is determined using the product of the single average component efficiencies shown in Equation (2.4) [19, 35, 48]

$$\eta_{Elec} = \prod_{i=1}^{n} \eta_{Comp,i} \tag{2.4}$$

The disadvantage of linear scaling approaches is that they cover only one design point at each technology level. Different electric architecture impacts such as a variation of the rotational speed, power demands or system voltages are not covered with these simplified methods in a broad design range. In off-design the electric architecture is treated in most cases, as a black box system with constant efficiencies during the entire mission e.g. Pornet [21] or Bonni et al. [50]. A first approach of more detailed investigations is performed for the electric motor [18, 39, 51] and the power supply [18, 52]. Schmitz [39] has considered the off-design efficiency characteristics of the electric motor via scaled performance maps. For the assessment at the overall aircraft level the efficiency of the battery model covers the impacts of actual State-of-Charge (SOC) and discharge current. However, the off-design characteristics of the remaining electric components in the PMAD such as power electronics and the impact of different design voltages are neglected. Furthermore, the PMAD system in those cases does not cover protection devices or fault current strategies, with the exception of the studies performed by Armstrong [37] and Stückl [18]. Stückl [18] has modeled in detail solely battery supplied universally-electric architectures covering different fault scenarios. This modeling approach also considers the required PMAD components and initial design voltage sensitivities. Nevertheless, the PMAD does not reveal an impact of a changing voltage or current demand on the power electronics in off-design. Armstrong et al. [37] published a comprehensive set of electric component models covering a mass and efficiency sensitivity with regard to the design voltage for a turbo-electric cryogenic power train. The off-design characteristics of the entire electric power train are not discussed in detail. An initial off-design performance chart of an electric power transmission as a function of the shaft speed and power has been exemplarily published by Bradley et al. [36] for a battery supplied electric architecture for the parallel hybrid-electric SUGAR Volt study. Based on this design chart, the efficiency of the battery supplied architecture varied between 10% and 90% (excluding the battery efficiency).

The different design possibilities and system performance estimations of different (hybrid) electric variants result in several design studies and methods that can be performed for the transport aircraft sector. An overview of the most important studies covering the critical methodologies and aspects of an electric architecture sizing for an electric power train are summarized in Table 2.2. These methods were analyzed for single aspects like *Design and Off-Design Performance*, *Architecture Sizing Scenarios* and *Voltage Impact*. This analysis covers further required considerations and implemented methods such as *Coupled Propulsor-Motor* combinations and performance or performed *Sensitivities at Aircraft Level.* The grey shaded area in this table marks the identified research gaps.

Table 2.2: Overview of relevant literature for hybrid and universally-electric system architectures and aircraft concepts. Grey area marks identified research gap at system level.

Application	**Component Power Estimation**	**Component Mass Estimation**	**Thermal Management Aspects**	**Electric Off-Design Performance**	**Voltage Impact**	**Coupled Propulsor-Motor**	**Battery Supplied Architecture**	**Architecture Sizing Scenarios**	**Sensitivities at Aircraft Level**	**Source**
Sizing Methods										
UEA	3	3	1	1	1	0	3	3	3	Stückl [18]
UEA	1	1	1	1	1	1	3	3	1	Vratny [52]
MIPH	1	1	0	1	0	1	1	0	3	Schmitz [39]
Turbo-electric	3	3	1	1	0	1	0	3	0	Armstrong et al. [37]
Turbo-electric for ship propulsion	1	3	0	1	0	0	0	0	0	Rucker et al. [25]
Aircraft Concepts										
UEA	3	3	1	1	1	0	3	3	3	Stückl et al. [17]
UEA	3	3	1	1	1	0	3	3	3	Isikveren et al. [35]
UEA	1	1	1	0	0	0	3	0	1	Hepperle [48]
DPH	3	3	1	1	1	0	3	3	3	Pornet et al. [21]
MIPH	1	1	3	1	1	0	3	1	3	Bradley et al. [36]
MIPH	1	1	1	0	1	0	1	0	3	Bogaert [49]

0 ... not covered
1 ... partially covered
3 ... fully covered
grey area marks identified research gap

The considered sizing methods for hybrid-electric power trains have performed very detailed analysis concerning the gas turbine design [43, 53, 54]. This includes, in detail, the design of the part load characteristics with regard to fuel flow and resulting net thrust for different flight altitudes, speeds and thrust lever positions [53]. The part load characteristics have been generated with the commercial gas turbine simulation tool GasTurb [55]. The assessment of hybrid-electric power trains has been performed to the level of detail of the involved subsystems. For a more sophisticated evaluation of the entire hybrid-electric power train in design and off-design, the electric systems architecture should cover a comparable fidelity-level such as the gas turbine, an identified open and essential issue.

2.3 Certification Requirements of Aircraft Electric Systems Architectures

In the previous section, the most important studies for electric architecture designs have been summarized. The majority of the studies only partially cover aspects concerning certification. Nevertheless, the current certification specifications for large passenger aircraft from the European Aviation Safety Agency (EASA) with the CS-25 [56] or the Federal Aviation Administration (FAA) with the Federal Aviation Requirements Part 25 [57] deal with fuel based propulsion systems, as well as, specifications for the electric system used for supplying the subsystems. Using electrical power for the primary power supply of the propulsion system is currently not covered by these specifications. Basic design criteria can be derived based on the existing certification requirements. This approach was already performed by Stückl [18] based on the EASA CS-25 requirements. In this study four important certification requirements have been identified on the power train level:

- ***CS 25.953 Fuel system independence***: "Each power train requires independent fuel system to be able to supply the other engine." [56]
- ***CS 25.1351 Generating system***: "Includes the entire electric architecture and includes (1) Power sources function properly when independent and when connected in combination; (2) No failure or malfunction of any power source can create a hazard or impair the ability of remaining sources to supply essential loads" [56]
- ***CS 25.1707 System Separation; Electrical Wiring Interconnection System (EWIS)***: "(d) Each EWIS associated with independent aeroplane power sources or power sources connected in combination must be designed and installed to ensure adequate physical separation and electrical isolation so that a fault in any one aeroplane power source EWIS will not adversely affect any other independent power sources. In addition: (1) Aeroplane independent electrical power sources must not share a common ground terminating location, and (2) Aeroplane systems static grounds must not share a common ground terminating location with any of the aeroplane independent electrical power sources" [56]
- ***CS 25.1357 Circuit protective devices***: "(a) Automatic protective devices must be used to minimise distress to the electrical system and hazard to the aeroplane in the event of wiring faults or serious malfunction of the system or connected equipment.(...) (b) The protective and control devices in the generating system must be designed to deenergise and disconnect faulty power sources and power transmission equipment from their associated busses with sufficient rapidity to provide protection from hazardous overvoltage and other malfunctioning." [56]

Aircraft requirements must be fulfilled by the system and also by the system dependent certification. For example, the classical One Engine Inoperative (OEI) case has to be covered when sizing the single components [56]. In a (hybrid) electric system, the power generation and the power consumer are mostly decoupled and the classical OEI must be further subdivided into scenarios that cover failure at the battery, which reduces the power generation output but still provides full thrust power. Such scenarios are defined in this thesis as the classical OEI, One Motor Inoperative (OMI) and One Battery Inoperative (OBI), with regards to the loss of an entire battery pack.

2.4 The Need for an Extended Method

The previously considered studies have shown that significant effort has been spent to investigate hybrid-electric and universally-electric propulsion systems for different application cases in the mobility sector including aviation. The main focus of these studies is turbo-electric propulsion systems that use a gas turbine as a main power conversion device for kerosene or solely battery powered propulsion systems for UEA aircraft.

Independently of the basic (hybrid) electric topology, the electric system of these concepts for high power application has been considered only as a point performance or as a simple black box system. A more detailed analysis was performed for a turbo-electric power architecture in the design case for a variation in voltage [37]. Stückl [18] also explored a sensitivity study for a certifiable electric system architecture concerning voltage variation for a UEA concept powered by batteries in the design point. An open question concerning the electric system is when combining the approaches to a parallel hybrid-electric topology, where a gas turbine and a battery powered electric system are within the sizing loop and are both contributing to the thrust generation. Specifically, the sizing and performance of the PMAD system is still an open issue for a broad range of different power and speed requirements of an electric motor covering design, as well as, off-design performances. These insights are required as a next step for a detailed flight performance optimization.

The focus in this thesis is set on electric power architectures suitable for parallel hybrid-electric topologies. For the design of this kind of power train concepts an extension of previous methods is required:

- A more detailed component modeling approach covering all relevant aspects for assessing electric system parameters suitable for aircraft conceptual design. This primarily includes the coverage of the component masses and efficiencies in design and off-design mode showing sensitivities with regard to chosen transmission power, voltage and switching frequencies.
- Identification of the impacts of different architecture design options such as different conversion strategies, protection systems, design voltages on the design and off-design performance including the entire thermal management system.

- With a more detailed design approach of the electric system architecture, more detailed investigations of the coupling effects with a propulsor can be performed. This includes the maximum available thrust in different flight states and the identification of limiting design parameters.

- When designing an electric systems architecture, it needs to be identified, if the system has to be mass or efficiency optimized (or both), and which factor is the critical sizing case at the overall aircraft level. After the identification of the critical architecture parameters it must be clarified how this design choice can be realized at the architecture level considering available technology options.

3 Sizing Methods for Electric Components

The following section describes the identification of suitable electric components for high power applications in the megawatt range. A generic Direct Current (DC) electric power architecture for propulsion applications is sketched in Figure 3.1. It consists of batteries, transmission cables and protection devices, converters, inverters and electric motors as well as cooling systems.

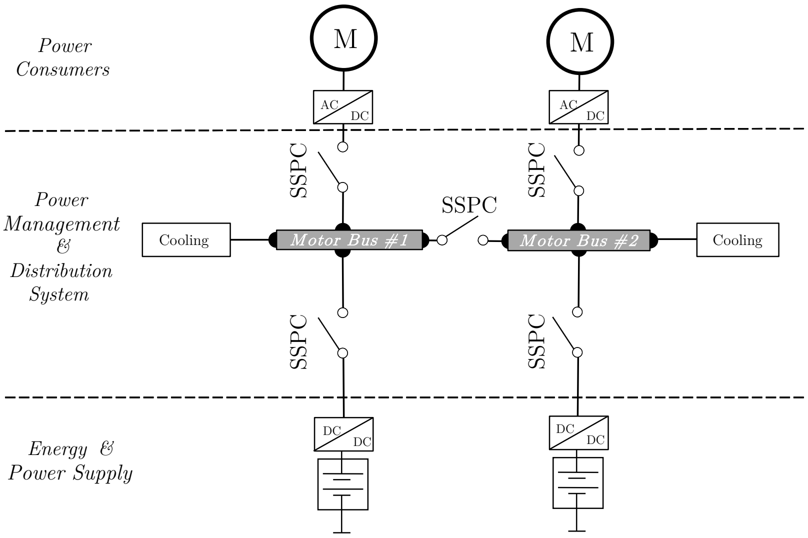

Figure 3.1: Generic DC electric power architecture covering the most important components [58]

For each single component performance models are generated covering design and off-design performance and the individual mass in the relevant design space. For all calculations it is assumed that the components are operating in quasi-stationary mode for performance estimations. This means that no transient behavior is taken into account in case of a power or electric current change. All components are modeled in a way that they have common input and output parameters as visualized in Figure 3.2.

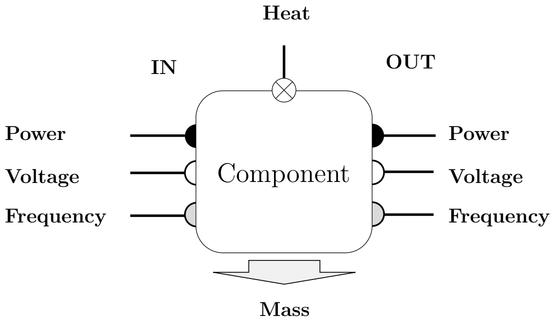

Figure 3.2: Basic component built-up covering all required input and output parameters

For the exchange of information between the different components the construct of a port is used. This concept is adopted from the Unified Modeling Language (UML), where a port is defined as an interface, which can provide (output) or require (input) certain information from or to the environment [59]. Therefore, the main input as well as output parameters of each single component are handled via power, voltage and frequency ports and additionally an output port heat. For the transmission of the electric current from the source to the loads a DC transmission is considered. The frequency port is only required for the electric motor and the inverter for a quasi-stationary application. Besides the performance each model delivers a specific heat demand, which is a function of the input and output requirements, and a certain mass in the component sizing case. The characteristics and masses are depending on the individual component and are described in the following subsections for each required component.

3.1 Battery

Batteries are used as main electric energy storage device for the electric power train. Fuel cell systems for power train applications are excluded from this study. The main reason for this approach is the low efficiency of a fuel cell system of around 65% at part load operation [60] in combination with their nominal operating temperature of around 60°C [61]. These properties have been identified as show-stoppers, mainly handling the wasted heat of a high megawatt fuel cell system. Therefore, this section provides an overview of battery developments in the last years and lists potential candidates for supplying a high power electric architecture. To identify the performance (voltage behavior and efficiency) of battery systems, the developed performance model is described including the off-design characteristics. Finally, an estimation of the entire mass of a battery system will be shown that is required for an overall aircraft level assessment.

3.1.1 Batteries as Energy and Power Storage Devices

Batteries are electrochemical storage and power conversion devices. A typical battery cell design consists of an anode and a cathode that are ionically connected by an electrolyte [62].

The combination of different materials of these three components defines the performance of a battery cell and can be optimized for energy storage and/or power capability. The voltage output of a battery can be determined with the help of the redox potential of the used elements. Based on the material combination of the anodes and cathodes a distinction between primary (not rechargeable) and secondary (rechargeable) battery cells can be made [63].

The discharge process of a battery cell is a chemical redox-reaction, where at the cathode a reduction and at the anode an oxidation takes place. The electrolyte allows for movements of ions, but not for electrons [62]. The electrons are conducted via an external circuit and are responsible for delivery of electrical work [62]. In contrast to primary battery cells this process is reversible for secondary cells allowing recharging and therefore reuse of the cells. In reality, the discharge and charge processes are not lossless. The mass transport of the electrons causes three different types of losses: convection, electrical mitigation and diffusion in a concentration gradient [64]. These losses are generating heat in a battery cell and are responsible for the voltage drop over a battery cell [62].

In Electric Vehicles (sEVs) normally rechargeable (secondary) battery cells are applied [63]. In conventional aircraft systems Nickel-cadmium batteries are used as a backup for electric subsystems and as start-up for the auxiliary power unit [65]. The B787 has introduced a new type of backup batteries based on lithium. Nickel-metal hydride and lithium based battery technologies are used [66] for electric power trains in hybrid and full EV in the automobile sector. Due to the high specific energy and specific power properties of lithium based batteries (compare Table 3.1) it can be assumed that future battery systems for EV will be also accommodated with these types of energy storage systems. For that reason, the described battery model will discuss lithium based battery cells.

Table 3.1: Overview of different battery types and their parameters taken from [66]

Battery Type	**Specific Energy** Wh/kg	**Specific Power** W/kg
Lead-acid	25-30	80-300
Nickel-cadmium	50-60	200-500
Nickel-metal hydride	60-70	200-1500
Lithium	60-150	80-2000
Zinc-air	200-300	70

The specific energy is defined as the ratio of the rated battery capacity to the battery mass and is an indicator of how much energy per unit mass may be stored [66]. Analogous, the specific power is the ratio of the rated peak power to the battery system mass and represents how much peak power can be delivered per unit mass [66]. Normally, the discharge behavior of a battery cell is strongly non-linear depending on the SOC of the battery cell and the discharge current (or *C-rate*). The SOC is an indicator of how much energy is still available in a battery cell. An equivalent for that definition is the depth of discharge defining of how much energy has already been released. The parameter *C-rate* represents the amount of electric current the battery is delivering at a given time and is based on the nominal capacity of the battery cell. The minimal *SOC* is implicitly a function of the cut-off voltage, U_{Cutoff}, and defines the end of the usable battery capacity. Therefore, U_{Cutoff} can be treated as the minimum voltage of a battery cell. Below this voltage the stored energy is not sufficient anymore to keep the electrochemical process operable. An example of the discharge behavior of a generic lithium-ion based battery cell is shown in Figure 3.3.

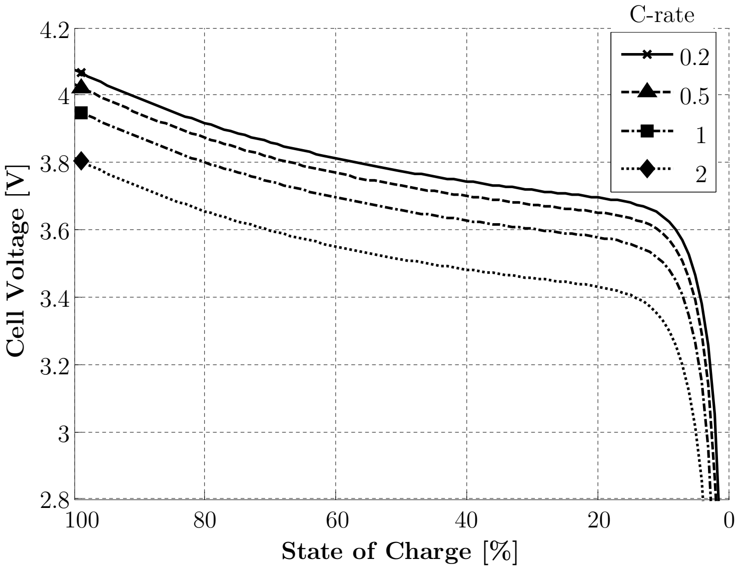

Figure 3.3: Example of a discharge behavior model of a generic lithium based battery cell. Model according to [67]

An entire battery pack is built up from multiple battery cells that are connected in series and/or parallel. The battery cells connected in series define the battery voltage and cells connected in parallel increase the capacity of the battery system at the defined system voltage. Depending on the design strategy, the battery cells connected in series can be grouped in a module. An example of this described setup is shown in Figure 3.4. Such a battery pack also includes a battery management unit or Battery Control Unit (BCU). A BCU is required to monitor the state of the single battery cells, to perform cell balancing in order to increase lifetime and to manage the safety of the battery [68]. In the scope of this work, the BCU is accounted for within the pack specific energy of the battery.

3.1.2 Battery Performance Simulation

As described in the previous section, a battery cell shows a strongly non-linear discharge behavior that is a function of the *C-rate* and actual *SOC* of the battery. A performance model based on a lithium-ion cell is required to estimate the necessary energy capacity for a certain power demand over a defined time span. This battery energy capacity is also

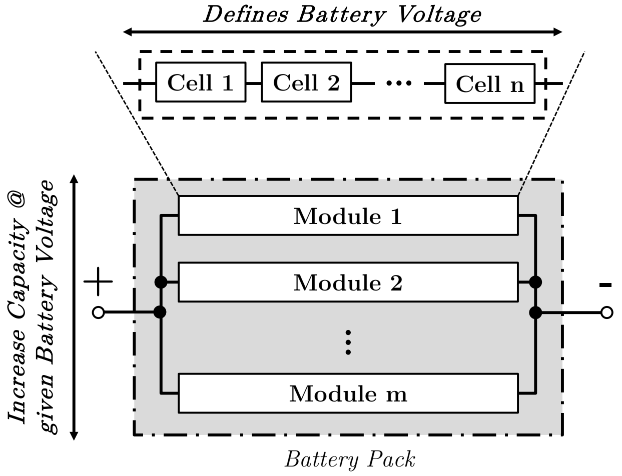

Figure 3.4: Battery pack design consisting of cells connected in series and parallel to reach specified design parameters based on [69]

an indicator for the overall battery pack mass. The sizing approach of the battery pack is visualized in Figure 3.5.

As starting point, the target battery pack output voltage, U_{Target}, and an initial battery energy capacity, E_{Bat}, is defined that determine the number of battery cells connected in series and in parallel as shown with Equation (3.1).

$$\begin{aligned} n_{Series} &= \left\lceil \frac{U_{Target}}{U_{Cell}} \right\rceil \\ n_{Parallel} &= \left\lceil \frac{E_{Bat}}{C_{Cell} \cdot U_{Target}} \right\rceil \end{aligned} \tag{3.1}$$

Finally, the number of modules in parallel is defined with an initial E_{Bat} in Watt hours and the battery cell nominal capacity, C_{Cell}, usually described in Ampere hours. U_{Target} of the battery pack can be defined at three different design points:

- begin of discharge
- end of discharge
- mean discharge voltage

Begin of discharge means that the target voltage should be reached at the beginning of the discharge of the battery at 100% *SOC*, while end of discharge means that the battery should deliver the target voltage at 0% *SOC*. In both cases the reference U_{Cell} is defined at U_{Cutoff}. Sizing the battery pack voltage for the *mean discharge voltage* case means that the average delivered voltage is equal to U_{Target} and U_{Cell} represents the nominal voltage of the battery

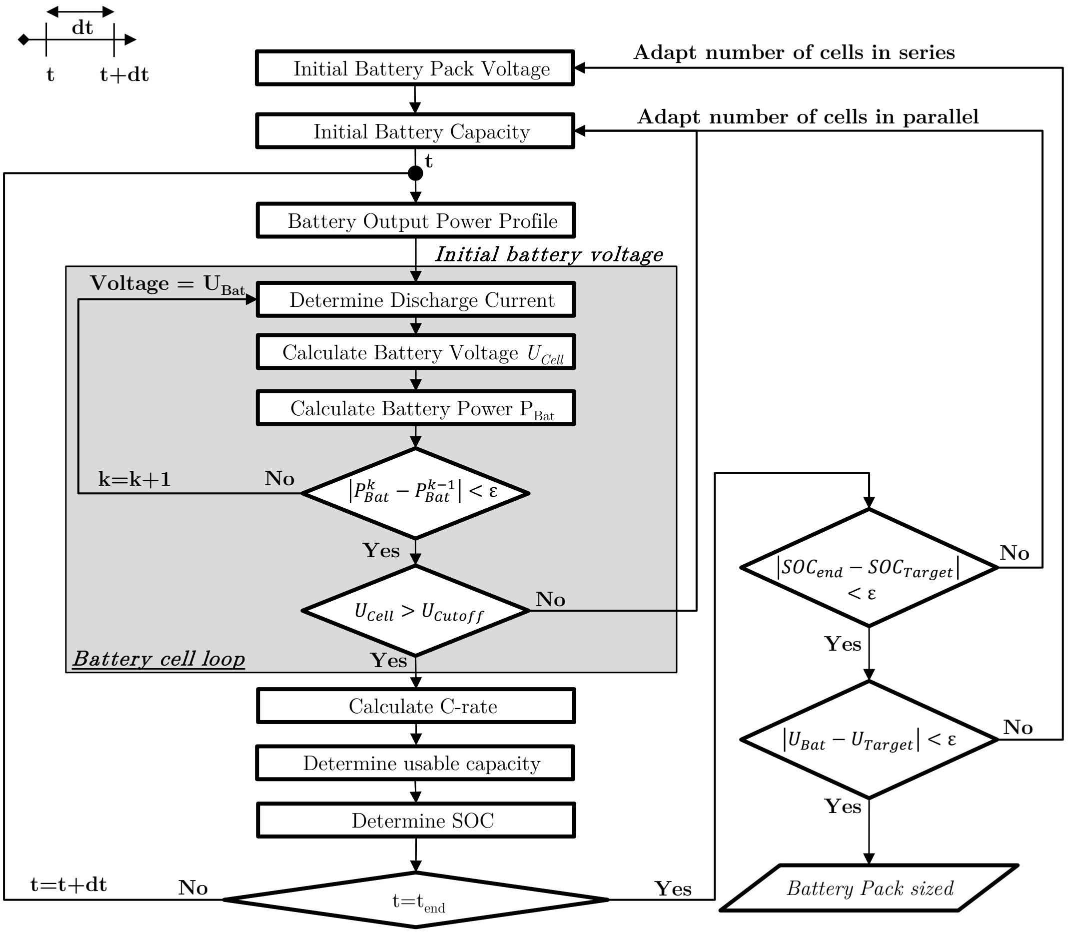

Figure 3.5: Battery pack sizing approach adapted from [69]

cell. This sizing case is strongly depending on the discharge profile. These different design points are important, when linking the battery to power electronics such as converters (see Section 3.3.2) or inverters (see Section 3.3.3), because it also influences the performance of these components.

Based on this configuration of the battery pack, the performance can be calculated for a required output power representing a discretized power profile (e.g. mission power profile). The discharge current for a certain time step, *t*, is calculated with Equation (3.2)

$$I = \frac{P(t)}{U_{Bat}(t) \cdot n_{Parallel}} = \frac{P(t)}{U_{Cell}(t) \cdot n_{Series} \cdot n_{Parallel}} \tag{3.2}$$

where P(t) is the current required power demand of the battery pack and U_{Cell} the corresponding cell output voltage, while U_{Bat} represents the battery output voltage. The cell voltage is depending on the open circuit voltage, U_{OC}, and the voltage drop over the internal resistance, $R_{i,Tot}$, according to Equation (3.3). $R_{i,Tot}$ is depending on the SOC and the discharge current. U_{OC} and $R_{i,Tot}$ are calculated with a polynomial regression as a function of SOC based on [70]. $R_{i,Tot}$ includes the single resistances (ohmic, activation and concentration losses) of a lithium-ion based battery cell. These dependencies require an iteration loop for each power step.

$$U_{Bat} = (U_{OC} - R_{i,Tot}(SOC) \cdot I) \cdot n_{Series} \tag{3.3}$$

With the actual battery voltage, the new battery output power, P_{Bat}, can be calculated and in turn a new U_{Bat} can be derived. This leads to a new discharge current until P_{Bat} meets the output power requirement. As convergence criterion ϵ a deviation between target and actual value is set to 10^{-6}.

$$P_{Bat} = U_{Bat} \cdot I \cdot n_{Parallel} \tag{3.4}$$

After the determination of the cell performance for the required power demand the resulting output voltage has to be higher than the cell specific U_{Cutoff}. Otherwise, the initial battery energy capacity was estimated too low and has to be increased in the next iteration loop. The SOC for the current time step can be finally calculated with Equation (3.5) including the discharge current of the actual time step divided by the nominal battery capacity.

$$SOC(t) = SOC(t-1) - \frac{I(t)}{C_{Nom}(t)} dt \tag{3.5}$$

With the voltage drop caused by $R_{i,Tot}$ of the battery, the discharge efficiency of the battery is determined with Equation (3.6).

$$\eta_{Bat} = 1 - \frac{I^2 \cdot R_{i,Tot}(SOC)}{U_{OC}(SOC) \cdot I} = 1 - \frac{U_i}{U_{OC}} \tag{3.6}$$

If all constraints are fulfilled, the battery pack capacity is determined out of this process and the pack is sized. The battery mass is estimated with the battery pack capacity using the specific energy, $\bar{\rho}_{Bat}$, of the battery pack shown in Equation (3.7).

$$m_{Bat} = \frac{E_{Bat}}{\bar{\rho}_{Bat}} \tag{3.7}$$

As baseline for the simulation of the battery cell and pack performance the assumptions shown in Table 3.2 are used.

Table 3.2: Parameters used to size a battery pack

Cell Parameter	**Value**
Nominal Voltage	3.7 V [67]
Maximum Voltage	4.2 V [67]
Cut-Off Voltage*	2.5 V
Nominal Capacity	2 Ah [67]
Battery Pack Parameter	**Value**
Specific Energy**	1000 Wh/kg [71]

* estimated based on charts by [67]

** theoretical value, used as a technology target for performance simulation at aircraft level

3.2 Electric Motor

An electric motor converts electric energy (with the help of magnetic and electric fields) into mechanical energy to drive for example a propulsive device. The following section provides an overview of the principle electric effects that occur in a motor and presents a simplified conceptual design method to size an electric motor. This section is mainly based on publication [72] of the author. The sizing approach (cf. Figure 3.6) is able to estimate the design and off-design efficiencies based on simplified scaling methods and masses of the total motor in a megawatt range.

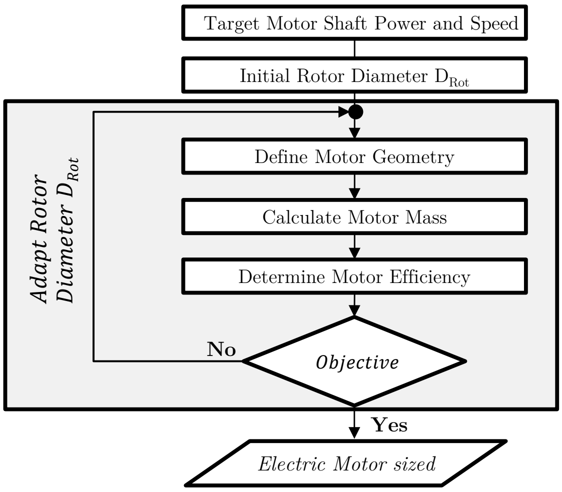

Figure 3.6: Principle sizing approach of an electric motor

3.2.1 Fundamentals of Electric Motors

A typical design of an electric motor comprises mechanical parts such as a rotor and a stator and electrical parts such as armature and electrical and magnetical fields. The stator is the fixed part and holds the armature and is normally embedded with the help of slots and teeth within the stator core. The armature consists of coils with several windings and is generating the Electromagnetic Field (EMF) with the help of an inverter-controller unit. The layout using slots and teeth assists to guide the generated EMF by the armature in an optimal way. The rotor transmits the required torque, Q, and rotational speed, n, via a shaft. The rotor core and the rotor armature are inducing an EMF, which is acting against the stator field. The rotor design layout is depending on the motor type. There is a geometrically imposed small air gap between the stator and the rotor that is mechanical necessary to allow the rotor to move. This air gap is impacting the electromagnetic performance of the motor. The smaller the gap can be designed the more efficient the electric motor can be operated. Another optimization field is the source quality of the supplied electric properties such as voltage, U, electric current, I, and the required frequency, f. These electrical parameters are responsible for the corresponding mechanical Q and n of the rotor shaft. The quality of these electric parameters can be controlled and additionally optimized via an electric control unit. This unit is in general anyway necessary to operate the motor within the operational envelope (see Section 3.3.3) for electric powered vehicles.

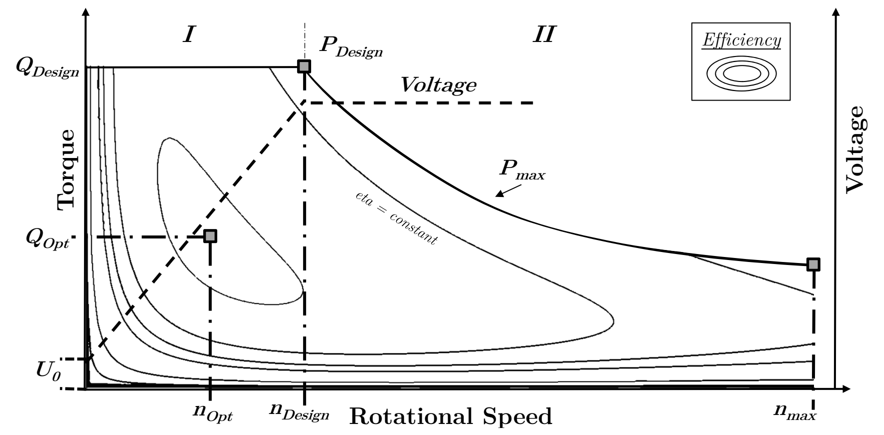

Figure 3.7: Generic performance chart of an electric motor based on [72]

The performance of an electric motor can be represented in a Q-n-diagram as schematically shown in Figure 3.7. The most important design parameters are marked, which are the design rotational speed, n_{Design}, the design torque, Q_{Design}, the maximum allowable rotational speed, n_{max}, and the schematic efficiency characteristics. Typically this (generic) performance map can be divided into two regions. The first region is equivalent to the constant torque region, where the maximum available output power is limited by the maximum electric current or mechanical torque. The second region constitutes the constant power region, where the torque decreases with increasing rotational speed. This region is also known as flux-weakening area. The sizing point P_{Design} is typically defined in the transition area between the two regions and is equivalent to the maximum power demand during the mission. This maximum mechanical power can be set in correlation with the electric power as shown in fundamental Equation (3.8)

$$\begin{aligned} P_{Design} &= Q \cdot \omega_{Shaft} = N \cdot B \cdot A \cdot I \cdot \omega_{Mot} \\ \text{with } \omega_{Shaft} &= 2\pi \cdot n_{Shaft} \end{aligned} \tag{3.8}$$

The Q and n_{Shaft} of the shaft is equal to the ideal electric power. This power can be calculated with the number of windings of one coil, N, the magnetic flux density, B, the conductor area of a winding, A, the electric current, I, and the motor angular velocity, ω_{Mot}. The angular velocity is depending on the number of pole pairs and, therefore, can be unequal to the mechanical rotational speed, ω_{Shaft}. Based on this equation, the mechanical torque can be written in form of

$$\begin{aligned} Q &= N \cdot B \cdot \omega_{Mot} = \frac{A}{l} \cdot N^2 \cdot I^2 \\ \text{with } B &= \mu \cdot H = \frac{I \cdot N}{l} \end{aligned} \tag{3.9}$$

where l, represents the coil length. Substituting the magnetic flux density, B, with the magnetic field strength, H, and the permittivity, μ, it can be recognized that the torque is only depending on the square of the electric current. Besides the electric current also the voltage, U, is an important design parameter and can be determined with Lenz's law shown in Equation (3.10)

$$\begin{aligned} U &= -N \cdot \frac{d\Phi}{dt} \\ U_{max} &= \Phi \cdot N \cdot \omega_{Mot} \\ \text{with } \Phi &= B \cdot A \end{aligned} \tag{3.10}$$

The voltage, U, depends on N and the change of the magnetic flux, Φ. Finally, the maximum voltage, U_{max}, can be determined with B and ω_{Mot}. In normal mode of operation when U_{max} is reached, the motor rotational speed can only be further increased when Φ is decreased, because A and N are fixed for a sized motor. This effect is also known as flux-weakening. Decreasing the magnetic flux can only be achieved when decreasing the magnetic flux density via the electric current. This in turn influences the available torque output in the same way. Equation (3.10) is also indicating that the motor speed correlates with the motor voltage. Normally, the motor voltage can be estimated using the voltage factor, K_V, for an existing motor. This approach is given in Equation (3.11) according to [73]

$$U = \frac{\omega_{Mot}}{K_V} \tag{3.11}$$

The terminal voltage can be calculated in the next step with Equation (3.12)

$$U_T = \frac{\omega_{Mot}}{K_V} + I \cdot R \tag{3.12}$$

Normally, K_V is determined through experimental measurements. In the first instance, the parameter K_V is estimated using the design point of the electric motor with $U_{T,Design}$, I_{Design} and the resistance of the coil, R, to cover the voltage characteristic as shown in Equation (3.13)

$$K_V = \frac{\omega_{Mot,Design}}{(U_{T,Design} - I_{Design} \cdot R)} \tag{3.13}$$

Using these relations it can be seen that the electric parameters I and U are dependent on the mechanical parameters Q and n. Table 3.3 summarizes how these parameters are linked when considering Equations 3.9 - 3.13.

Table 3.3: Scaling relations for the motor current and voltage in dependency of rotational speed and torque in region I and II adapted from [72]

	Region I	Region II
Voltage U	$\sqrt{Q}$,n	constant
Current I	$\sqrt{Q}$	

These simplified dependencies are based upon general physical considerations and are influenced by the way how the electromagnetic forces are generated. There are two main options common to generate the electromagnetic forces such as Permanent Magnets (PM) and induction via coils. For these possible options different electric motor architectures are available. For hybrid and also full EVs the most common ones are the Asynchronous Motor (ASM), the Switched Reluctance Motor (SRM) and the Permanent Magnet Synchronous Motor (PMSM). The individual advantages and disadvantages are assessed in Table 3.4.

Table 3.4: Eligible electric motor types adapted from [72] and [74]

Electric Motor Type	ASM	SRM	PMSM
Efficiency	0	0	+3
Torque Density	0	0	+1
Mass	0	+1	+3
Inverter Complexity	0	-3	-1

-3 strongly negative; -1 negative ; 0 neutral; +1 positive; +3 strongly positive

The most important parameters for an eligible electric motor type are the efficiency and mass characteristics for electric power trains. A well-designed electric motor should offer high efficiency at low mass. Based on Table 3.4 the PMSM shows the best trade-off between these properties. The most common PMSM configuration is the brushless PMSM, a type of a DC motor, where the rotor windings are replaced by PM like Neodymium-Iron-Boron (NdFeB) to generate the required magnetic field. Beside the PMSM, the most common electric machine mainly used in industrial applications is the ASM. The stator design is nearly identical to the PMSM and consists of slots housing the windings that are supplied by an external power source. The rotor of an ASM consists of copper bars and rings forming the armature, also called squirrel cage. The rotating magnetic field within the stator is inducing a counteracting field within this squirrel cage. This induction and in turn shaft rotation takes only place when the rotor receives an induced EMF from the stator. Due to this effect the rotor runs at a lower (asynchronous) speed than the stator and this is also affecting the efficiency.

The brushless PMSM design seems the most eligible candidate. From an efficiency point of view, a PMSM can reach values above 95% [75] mainly driven by the low rotor losses that are nearly zero. Furthermore, a PMSM is also characterized by high reliability and specific powers up to 5 kW/kg [34]. However, disadvantages of a PMSM are the idle losses during high speeds and low load [76], the high production costs and the complex control [74]. The idle losses can be neglected for aircraft applications and are only relevant for ground based vehicle. Another sizing constraint is the limitation of the rotor tip speed. According to [77] the tip speed is limited at maximum 250 m/s for PMSMs.

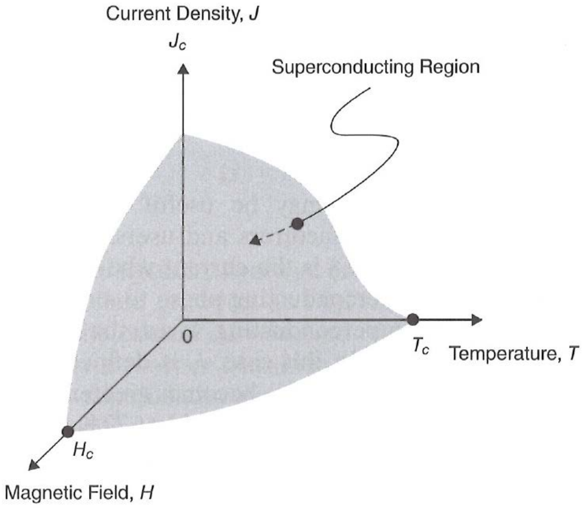

Figure 3.8: Generic critical surface description of a superconductivity material depending on the magnetic field, H, the current density, J, and the temperature, T taken from [78]

High Temperature Superconducting (HTS) motors seem to be a promising technology for high power applications in the megawatt range that are required for hybrid-electric transport aircraft. This motor type uses the physical effect of superconducting materials. These materials have the capability that they lose their ohmic resistance below a specific temperature. There are two different types of superconducting motors available: low temperature motors that have an operating temperature below 5 K and HTS motors having an operating temperature between 40 K [78, 79] for high-field and 77 K for low-field applications [78]. The superconductivity effect depends on the three inter-related parameters current density, J, magnetic field, H, and temperature, T generically shown in Figure 3.8. The extreme values, where superconductivity is still applicable, are referred to critical current density, J_c, critical magnetic field, H_c, and critical temperature, T_c [78]. If only one parameter exceeds its maximum, the material reverts to its normal conducting state. This effect is called quenching. In the quench state the stored power within the cable or coil is dissipated by heat due to the immediate occurrence of the cable resistance at high current densities [80].

HTS technology can be applied in two ways in an electric motor design: 1.) replacing the PMs by HTS coils increase significantly B and can offer specific powers of up to 10 kW/kg at motor speeds up to 35,000 rpm [81]. This motor configuration is described as partial HTS motor within this thesis. 2.) The second type is referred to as a full HTS motor, where besides the rotor also the stator armature is replaced by HTS coils. This configuration is increasing the electric current density within the air gap (see Section 3.2.2) and offers efficiencies of more than 99.5% and expected specific powers up to 40 kW/kg (excluding cooling mass) [82]. In this configuration the stator is normally designed slotless, because otherwise the magnetic field is limited by the saturation of the surrounding iron [78].

3.2.2 Geometry Definition

The geometric design of an electric motor is essential for the calculation of its efficiency and mass. It depends on the requirements of the necessary torque that has to be delivered at a certain speed. Based on these parameters and the type of electric motor, the geometry such as active rotor diameter and active rotor length can be estimated based on methods published by [83] and [25]. The basic geometric parameters of the electric motor design are sketched in Figure 3.9.

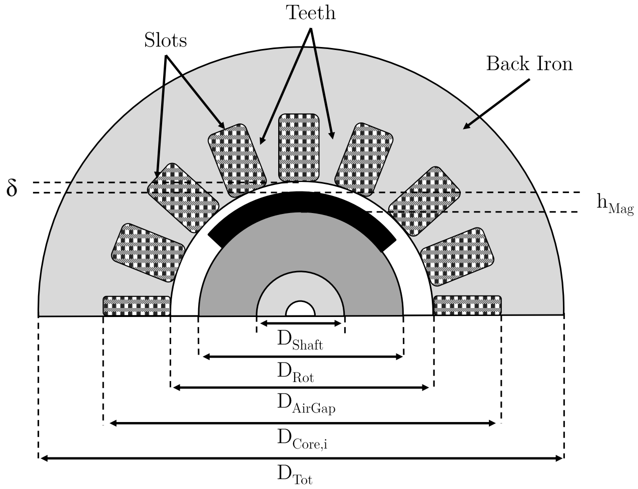

Figure 3.9: Geometry definition of the electric motor model based on [84]

The air gap diameter, D_{AirGap}, is calculated with Equation (3.14) using the rotor diameter, D_{Rot}, as free design parameter and is responsible for the required torque generation.

$$D_{AirGap} = D_{Rot} + 2 \cdot (h_{Mag} + \delta) \tag{3.14}$$

The parameter h_{Mag} represents the magnet height established according to methods published by [84]. In this study a sensitivity analysis was performed for h_{Mag} as function of rotational speed at constant shaft power demand of 20 MW. An optimal h_{Mag} has been identified at 2.5 cm for rotational speeds up to 7000 rpm. For simplification of this model, this height is used for all conducted electric motor designs, because the magnet mass has an impact of less than 4% of the entire electric motor mass [72]. Furthermore, D_{Rot} also includes the required shaft that is responsible for the transmission of the torque and speed to the mechanical load. The shaft diameter, D_{Shaft}, can be calculated with the shaft equation using the equivalent stress, $\tau_{max,Shaft}$, of van Miese.

$$D_{Shaft} = 2 \cdot \left(\frac{Q_{max}}{\left(1 - DR_{Shaft}^4\right) \cdot \pi \cdot \tau_{max,Shaft}} \right)^{\frac{1}{3}} \tag{3.15}$$

$$\text{with } Q_{max} = k_S \cdot \frac{P_{Design}}{2\pi \cdot n}$$

where Q_{max} corresponds to the maximum transmitted torque corrected by a safety factor, k_S, the ratio between the inner and outer radius of the hollow shaft, DR_{Shaft}, and the maximum shear stress of the used material, $\tau_{max,Shaft}$.

The mechanically imposed air gap, δ, the distance between rotor magnets and stator, can be estimated using a method according to [83]

$$\delta = \frac{C_1 + C_2 \cdot P^{0.4}}{1000} \tag{3.16}$$

This relation depends on the design parameters of the electric motor and the number of pole pairs used at the rotor. A magnet always appears with a north and a south pole, which corresponds to one pole pair [83]. The motor arrangement sketched in Figure 3.9 is representing a one pole pair motor. According to Equation (3.16) the parameters C_1 and C_2 are depending on the number of pole pairs and can be obtained by Table 3.5 taken from [83].

Table 3.5: Air gap parameters taken from [83]

	$\mathbf{C_1}$	$\mathbf{C_2}$
One pole pair	0.2	0.01
More than one pole pair	0.18	0.006

For the optimization of the motor design using D_{Rot} as free parameter, it has to be considered that it is limited by the maximum centrifugal force according to [83]

$$R_{p,0.2} \geq k_S \cdot \rho \cdot \pi^2 \cdot n_{max}^2 \cdot D_{Rot}^2 \tag{3.17}$$

$R_{p,0.2}$ represents the maximum yield strength of the rotor material and n_{max} the maximum rotational speed of the rotor. As mentioned, beside the centrifugal force, also the tip speed is a limiting factor when designing a PMSM. Finally, with D_{Rot} the required rotor (or active) length to transmit the necessary torque can be determined using the surface of the rotor cylinder and the available shear stress, σ, as defined in Equation (3.18)

$$l_{Rot} = \frac{P_{Design}}{2 \cdot D_{Rot}^2 \cdot \pi^2 \cdot n \cdot \sigma} \tag{3.18}$$

The available shear stress can be calculated based on [83] extended with a scaling relation for B according to [84] shown in Equation (3.19)

$$\sigma = J \cdot \frac{1}{\sqrt{2}} \cdot B \cdot \left(\frac{D_{Rot}}{D_{Ref}}\right)^{0.25} \tag{3.19}$$

It is a function of the air gap current density J, B and D_{Rot}. Furthermore, the available B is scaled based on a reference diameter, D_{Ref}, that is linked to the corresponding B. Finally, the total electric motor diameter, D_{Tot}, can be calculated with Equation (3.20)

$$D_{Tot} = D_{Core,i} + \frac{k_{Yoke}}{p} \cdot D_{AirGap} \tag{3.20}$$

and is dependent on the inner core diameter, $D_{Core,i}$, plus the core depth. The core depth is defined as ratio of the stator yoke ratio, k_{Yoke}, to the number of pole pairs, p, times D_{AirGap}. With the slot depth, d_{Slot}, $D_{Core,i}$ is calculated with Equation (3.21)

$$D_{Core,i} = D_{AirGap} + 2 \cdot d_{Slot} \tag{3.21}$$

In the end, the total machine length, l_{Tot}, can be determined with

$$l_{Tot} = l_{Rot} + 2 \cdot \frac{l_{Coil,End}}{2 \cdot \pi} \tag{3.22}$$

The length of an end coil, $l_{Coil,End}$, is directly calculated according to methods described in [25]. Besides the limitation of D_{Rot} constrained by the maximum centrifugal force and tip speed, the motor length is limited by the critical angular speed. This critical speed is defined at the first mechanical resonance bending mode. The maximum allowable rotor length, l_{Rot}, can be calculated according to [83] with Equation (3.23), which ensures a rotor length that is below the first critical resonance speed.

$$l_{Rot,max} = k_{Length} \cdot \sqrt{\frac{\pi^2}{k \cdot 2\pi \cdot n_{max}} \cdot \sqrt{\frac{E \cdot J}{\rho \cdot A}}} \tag{3.23}$$

The maximum rotor length is depending on n_{max}, the Young's modulus, E, and density, ρ, of the rotor material, the rotor area, A, and the mass moment of inertia, J [1]. This estimation is valid for a smooth-solid rotor. In reality, bearing mountings, slits, etc. are impacting the resonance behavior and reduces the theoretical maximum length. An additional safety factor, k_{Length}, is considered to take this effect into account. According to [83], the reduced length can be up to a third of the theoretical length. The design parameters of the electric motor based on [25] and [83] are summarized in Appendix A.

3.2.3 Mass Estimation

Based on the geometry, the mass for each component can be estimated using the method published by [25]. The total motor mass is the sum of all components

$$m_{Mot} = m_{Shaft} + m_{Rot} + m_{Mag} + m_{Stator} + m_{Arm} + m_{Serv} \tag{3.24}$$

For each electric motor component the volume is calculated and multiplied with the corresponding material density. The shaft mass, m_{Shaft}, is determined with Equation (3.25)

$$m_{Shaft} = (D^2_{Shaft} \cdot \left(1 - DR^2_{Shaft}\right) \cdot \pi \cdot l_{Shaft}\Big) \cdot \rho_{Shaft} \tag{3.25}$$

The shaft length, l_{Shaft}, is estimated to be 120% of l_{Tot} to consider bearing and mounting space. ρ_{Shaft} is the material density of the shaft itself.

The rotor mass, m_{Rot}, is calculated with the rotor material density, ρ_{Rot},

$$m_{Rot} = \left(\frac{D^2_{Rot} - D^2_{Shaft}}{4} \cdot \pi \cdot l_{Rot}\right) \cdot \rho_{Rot} \tag{3.26}$$

---

[1] full shaft design considered

The magnet mass, m_{Mag}, is estimated with the angle between the magnets, α_{Mag}, and the magnet density, ρ_{Mag}, according to [25]

$$m_{Mag} = \frac{1}{2} \cdot p \cdot \alpha_{Mag} \cdot \left(\left(\frac{D_{Rot}}{2} + h_{Mag} \right)^2 - \frac{D_{Rot}^2}{4} \right) \cdot l_{Rot} \cdot \rho_{Mag} \tag{3.27}$$

The stator mass, m_{Stator}, includes the mass of the back iron, m_{Iron}, and the teeth mass, m_{Teeth},

$$m_{Stator} = m_{Iron} + m_{Teeth} \tag{3.28}$$

The iron mass, m_{Iron}, can be obtained with Equation (3.29) and the stator density, ρ_{Stator}, according to [25]

$$m_{Iron} = \frac{1}{4} \cdot l_{Rot} \cdot \pi \cdot (D_{Tot}^2 - D_{Core,i}^2) \cdot \rho_{Stator} \tag{3.29}$$

and m_{Teeth} is estimated similarly according to [25]

$$m_{Teeth} = l_{Rot} \cdot N_{Slots} \cdot \left(h_{Slot} \cdot w_{Teeth} + \pi \cdot \frac{D_{Rot}}{N_{Slots}} \cdot \delta_{Slot} - w_{Slot} \cdot \delta_{Slot} \right) \cdot \rho_{Stator} \tag{3.30}$$

where N_{Slots} is the number of slots of the motor, h_{Slot} the height of the slot, δ_{Slot} the slot depression depth, w_{Teeth} the width of one tooth and w_{Slot} the slot depression width.

The armature mass, m_{Arm}, is calculated with

$$m_{Arm} = N_{Phases} \cdot l_{Conductor} \cdot A_{Conductor} \cdot \rho_{Conductor} \tag{3.31}$$

where N_{Phases} are the number of phases, $l_{Conductor}$ the conductor length of one phase calculated according to [25], $A_{Conductor}$ the conductor cross section based on the design current and the current density of the used conductor material and, finally, the conductor density, $\rho_{Conductor}$.

Beside the main components, also masses for the frame and mountings have to be taken into account that are defined as service masses, m_{Serv}. These m_{Serv} of an electric motor are considered with a mass fraction factor, k_{Serv}, of about 13% of the total component masses as recommended by [85]

$$m_{Serv} = k_{Serv} \cdot (m_{Shaft} + m_{Rot} + m_{Mag} + m_{Stator} + m_{Arm}) \tag{3.32}$$

3.2.4 Efficiency Simulation

Beside the mass, also the efficiency is an essential parameter to estimate the overall electric system performance. It is important to determine the design and off-design performance to conduct an overall system optimization. In a PMSM normally five main loss types occur, namely:

- Core losses of the stator
- Armature losses
- Friction and windage losses
- Stray load losses
- Miscellaneous losses

The core losses of the stator occur due to remagnetization (hysteresis) effects within the core material. The armature losses are generated by the electric current normally due to the ohmic resistance of the stator armature material. On the rotor side, the main losses are represented by the friction (and windage) losses caused by the air friction and losses of the bearings. Beside these primary losses, also secondary losses can occur. These secondary losses are for example evoked by geometry impacts such as additional stray load losses in bearings or between end coils and proximate metallic parts and are combined in the miscellaneous losses. Covering all these different loss types requires a huge computational effort with regard to finite-element methods to solve the Maxwell equations [86] for an accurate efficiency calculation. For aircraft conceptual design, these time-consuming methods are not favorable. For that reason a simplified method is used. This simplified method covers the mentioned loss types based on an existing reference motor and scaled accordingly with the design parameters such as P_{Design}, n and U_{Design}. The proposed approach is applicable to conventional, as well as, to HTS motor designs and is used to generate generic performance maps of a PM based motor architecture.

The motor efficiency, η_{Mot}, is defined in Equation (3.33) by summing up all individual power losses P_L of the electric motor for each operational point. Additionally, the required cooling losses, P_{Cool}, are considered that are depending on the motor type and can be estimated with methods described in Section 3.6.

$$\eta_{Mot} = \frac{P_{Out}}{P_{In}} = \frac{P_{Shaft}}{P_{Shaft} + \sum\limits_{n} P_{L,n} + P_{Cool}} \tag{3.33}$$

As mentioned before, the efficiency calculation is based on a scaling approach of a baseline electric motor. Therefore, each loss category is scaled with the power ratio, k_{Power}, of the new design power, P_{Design}, to the reference power, P_{Ref}. Because an existing motor is scaled to different design powers and speeds, the principle architecture of the motor, such as number of pole pairs, is not changed.

$$k_{Power} = \frac{P_{Design}}{P_{Ref}} \tag{3.34}$$

The core losses, $P_{L,Core}$, are mainly depending on the electric current and the frequency. As described in Section 3.2.1, the square of the electric current is equal to the torque and the frequency is direct proportional to the rotational speed. With these relations the core losses can be scaled according to Equation (3.35) with the mechanical parameters Q and n as shown by [87].

$$P_{L,Core} = k_{Power} \cdot P_{L,Ref,Core} \cdot \left(\frac{Q}{Q_{Design}}\right)^{\frac{1.353}{2}} \cdot \frac{n}{n_{Design}} \tag{3.35}$$

The armature losses, $P_{L,Arm}$, are depending only on the electric current and corresponds to the square root of the torque. Therefore, the armature losses can be estimated with Equation (3.36) including a technology factor, k_{Tech}, to consider also technologies such as HTS armature that reduce these losses to zero.

$$P_{L,Arm} = k_{Tech} \cdot k_{Power} \cdot P_{L,Ref,Arm} \cdot \frac{Q}{Q_{Design}} \tag{3.36}$$

According to [87], the stray load losses, $P_{L,Stray}$, are a function of the square of the magnetic flux ratio and the square of the rotational speed ratio. The magnetic flux has been identified in Section 3.2.1 to be proportional to the torque. Therefore, $P_{L,Stray}$ can be estimated with

$$P_{L,Stray} = k_{Power} \cdot P_{L,Ref,Stray} \cdot \frac{Q}{Q_{Design}} \cdot \left(\frac{n}{n_{Design}}\right)^2 \tag{3.37}$$

The air gap causes air friction losses, $P_{L,Air}$. These air friction losses can be calculated according to [25] with Equation (3.38). In contrast to the other loss types, $P_{L,Air}$ is directly calculated with the determined motor parameters and is not scaled.

$$P_{L,Air} = k_{Tech} \cdot 1.7 \cdot \rho_{Air} \cdot D_{Rot}^4 \cdot l_{Rot} \cdot n^3 \cdot \left(\frac{\pi^2 \cdot D_{Rot} \cdot \delta}{\nu_{Air}}\right)^{-0.15} \tag{3.38}$$

It depends on the air parameters such as the dynamic viscosity, ν_{Air}, and the air density, ρ_{Air}. To consider possible future trends such as evacuating the air gap section to reduce the air friction losses, the technology factor, k_{Tech}, is included.

For the estimation of the secondary losses, $P_{L,Sec}$, Equation (3.39) is used according to [87] and are mainly dependent on the square of the electric current and the rotational speed

$$P_{L,Sec} = k_{Power} \cdot P_{L,Ref,Bearing} \cdot \frac{Q}{Q_{Design}} \cdot \left(\frac{n}{n_{Design}}\right)^{1.25} \tag{3.39}$$

3.2.5 Benchmark of Electric Motor Model

Based on the previously described methods, a reference partial HTS is modeled according to the reference electric motor as listed in Table A.4 in Appendix A. For this purpose two cooling scenarios are considered: one with a constant cooling power demand according to the reference and one with the developed cryocooler model described in Section 3.6.2. The results of the efficiency comparison are shown in Figure 3.10.

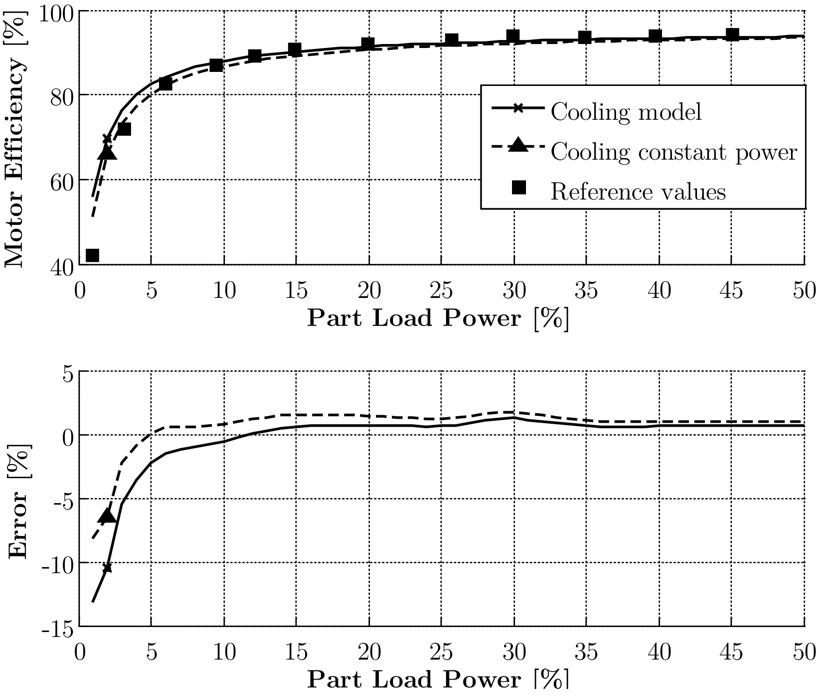

Figure 3.10: Efficiency validation of electric HTS motor performance [72]

The relative error between the developed efficiency model and the reference data is less than 1% in the relevant part load area (above 20%). Only at low torque operation the deviation is increasing up to 10%. For the further considerations this low part load area is not relevant and can be neglected. The developed cryocooling model shows a slightly better match in the relevant part load area with the reference data of up to relative 0.4% compared to an assumed constant cooling power demand.

Figure 3.11 gives an overview of the specific power trends for the motor types conventional conducting, partial HTS and full HTS motors at different rotational speeds generated with the described electric motor model. The specific powers are currently at 5 kW/kg for conventional motors as demonstrated by [34]. Future trends expect for normal conducting machines values of up to 20 kW/kg for a targeted EIS year of 2030 [88] covered by the used electric motor model. As claimed by [82], full HTS motors can reach specific powers of up to 40 kW/kg at high rotational speeds.

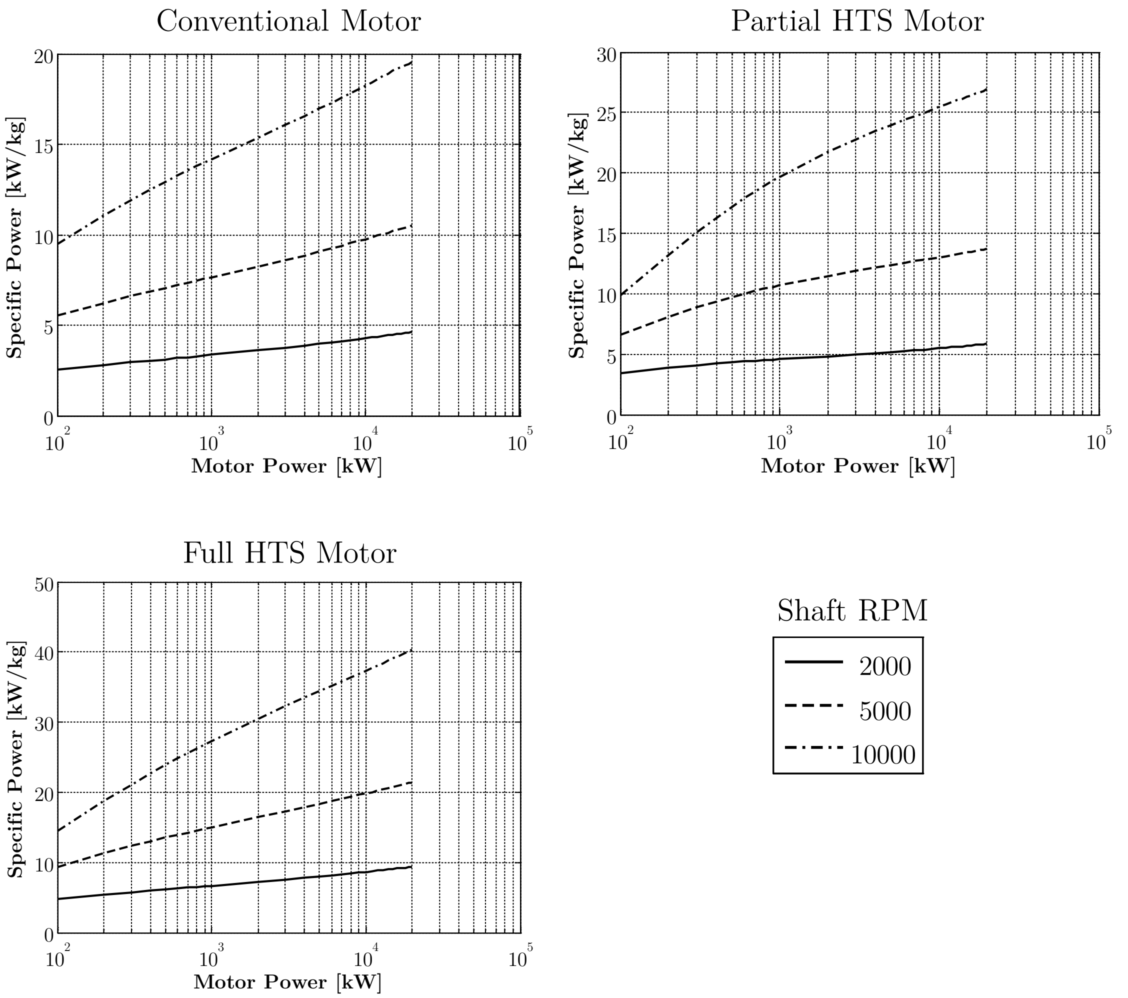

Figure 3.11: Results of the specific power trends generated with the developed electric motor model for different shaft powers, speeds and different motor architectures

3.3 Power Electronics

Power electronics are required to control the voltage and/or the electric current level (type) between the input and the output of the component. Voltage and current level changes are performed via converters that change the voltage level between the input and the output, and via inverters that change the voltage type e.g. from DC to Alternating Current (AC). This manipulation of the voltage is performed with a Power Switch (PS) and a diode, which are chopping the electric current in a way that the targeted voltage level is reached. The following section describes the principles of PS using semi-conductor materials and gives an overview of the modeling approach for converters and inverters with regard to efficiency and mass. Furthermore, it describes the approach to simulate the design and off-design efficiencies for high power applications in the megawatt range.

3.3.1 Principles of Semi-Conductors as Power Switches

There are different ways to convert the voltage type and/or level in a DC network. The simplest way can be realized using PS to chop the electric current in a way that the required output voltage is reached. For that purpose different types of PS are available: mechanical switches or switches based on semi-conductors. Semi-conductor switches seem to be the most efficient type, because they are more easily to control compared to the mechanical switches, but showing a more complex loss characteristic.

There are different types of semi-conductor based PS available such as thyristors, Metal-Oxide Semi-conductor Field Effect Transistors (sMOSFETs) or Insulated Gate Bipolar Transistors (sIGBTs). Based on [72], the IGBTs seem to be the most suitable PS type offering the best efficiency at the required power and frequency level necessary for an aviation application. In reality, the switching process of a PS is not lossless. The losses are directly transferred into heat, in the first instance, and can damage and even destroy the component, if a critical temperature is reached. The loss characteristic of a semi-conductor can be grouped into two main loss types, static and non-static losses. These loss types are further divided into sublosses as shown in Figure 3.12.

The common ohmic or also conduction losses are represented by the on-state losses that are a direct function of the electric current and the ohmic resistance of the semi-conductor. The second type of static losses is represented by the blocking losses, which occur if the semi-conductor is in blocking (non-conducting) mode. These losses can normally be neglected, because compared to the other losses they are relatively small [89].

For the static losses the main sizing parameter is the design output electric current, I_{Out}, and can be calculated according to Ohm's law with Equation (3.40)

$$I_{Out} = \frac{P_{Design}}{U_{Design} \cdot n_{Parallel}} \tag{3.40}$$

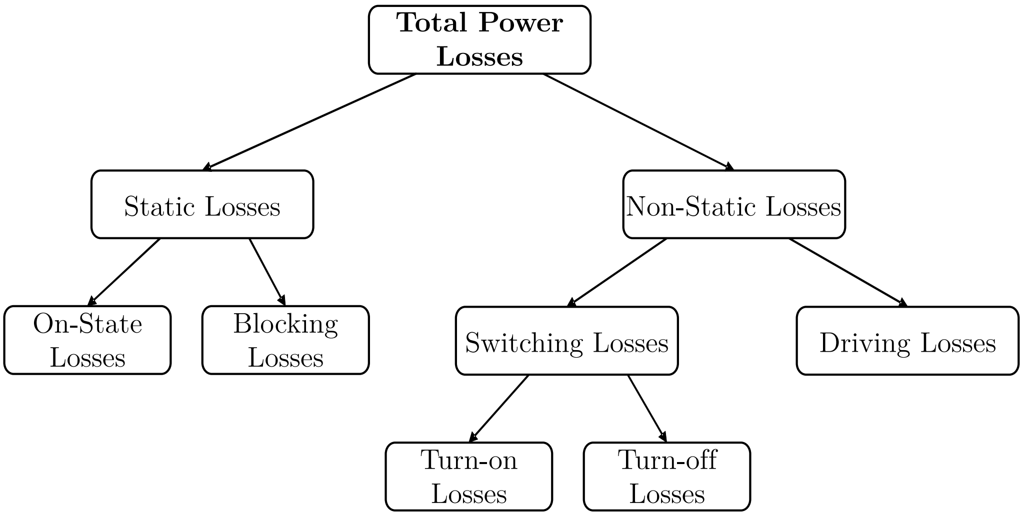

Figure 3.12: Overview and categorization of the different loss types of semi-conductor switches according to [89]

where P_{Design} is the design power, U_{Design} the design voltage of the PS and $n_{Parallel}$ the number of connected PS in parallel. An IGBT has a non-constant behavior of the conduction loss characteristic. Based on [89] this (forward) characteristic can be approximated via a linear regression of the component covering the constant DC and the AC term as shown in Equation (3.41)

$$P_{Cond} = I_{Out} \cdot U_0 + I^2_{Out,RMS} \cdot R(I_{Out}) \tag{3.41}$$

U_0 is the threshold voltage of the PS, $I_{Out,RMS}$ the root mean square of the electric current and, R, the ohmic resistance of the PS. The ohmic resistance is a function of I_{Out} and is characterized by the gradient of the forward characteristic of the used IGBT. Furthermore, it is a function of the junction temperature [89]. For the scope of this thesis the temperature of the components is kept at a constant level. This is realized by assuming that the associated thermal management system is capable to provide the necessary corresponding cooling flow.

The second main loss type is represented by the non-static losses. They can be further subdivided into switching and driving losses. The driving losses are normally in the same order of magnitude like the blocking losses and can be also neglected in the first instance [89]. The switching losses of a PS occur when the conduction state of the PS changes and can account for a significant amount of the total losses. This loss type is mainly depending on the on and off state energy of the used PS and the switching frequency, f_{SW}. The switching energy depends on I_{Out}, but also on the output voltage, U_{Out}. The switching loss characteristic of a semi-conductor PS can be represented via a non-linear regression according to [89] as shown in Equation (3.42)

$$P_{SW} = f_{SW} \cdot E_{On+Off,Ref} \cdot \left(\frac{I_{Out}}{I_{Ref}}\right)^{K_I} \cdot \left(\frac{U_{Out}}{U_{Ref}}\right)^{K_V} \tag{3.42}$$

This regression uses a switching energy, $E_{On+Off,Ref}$, including the required energy for on and off state based on a reference electric current, I_{Ref} and voltage, U_{Ref}. The switching energy can be scaled to any other operating points within the component limits by changing I and U. The scaling power factors for the electric current, K_I, and voltage, K_V, have to be determined using an existing PS. Beside PSs, also diodes are required to operate power electronics, mainly to control the electric current flow direction. Diodes are also based on semi-conductors. Therefore, for the performance calculation the same regressions can be applied as for the PS.

A common control strategy of semi-conductors is performed via Pulse Width Modulation (PWM). Hereby, the electric current is chopped with the help of the PS and a microcontroller. In this case, the microcontroller controls via the timely length of a pulse the base voltage of the IGBT and, in turn, the voltage and current at the collector and emitter. This pulse length depends on the purpose of the control strategy, for example changing the voltage level or the voltage type (sinusoidal waveform) as explained in more detail in the following sections.

For the set-up of the different power electronics, the parameters listed in Table 3.6 are used for IGBT PS and diode for all converter and inverter designs.

Table 3.6: Baseline component parameters for the design of the power electronics based on existing IGBT by Semikron [90]

IGBT	**Value**	**Diode**	**Value**
Voltage Collector Emitter U_{CE}	0.8 V	Forward Voltage U_{F0}	1.1 V
Maximum Voltage $U_{CE,max}$	1200 V	Maximum Voltage $U_{max,D}$	600 V
Maximum Current $I_{C,max}$	1800 A	Maximum Current $I_{max,D}$	900 A
Reference Voltage U_{Ref}*	600 V	Reference Voltage $U_{Ref,D}$*	600 V
Reference Current I_{Ref}*	550 A	Reference Current $I_{Ref,D}$*	550 A
Switching Energy E_{tr} @$600V$	195 mJ	Switching Energy E_D	65 mJ
Collector Resistance R_{CE} @150°C	1.8 $m\Omega$	Forward Resistance R_F	1.71 $m\Omega$
Mass	150 g	Mass	20 g
* calibrated			

There are several materials for semi-conductors available. The most common are Silicon (Si) based semi-conductors. Another promising development is Silicon-Carbide (SiC) semi-conductors. The SiC semi-conductors offer lower switching losses of more than 85% compared to Si, but higher conduction losses of around 40% (compare Table 3.7). Nevertheless, for active power electronics such as converters or inverters the SiC semi-conductors seem to be the better option, because the switching losses are usually the dominating losses in these systems. In this study, the performance of IGBTs is corrected by the listed average values if SiC instead of Si are used as semi-conductor material.

Table 3.7: Comparison of the properties of Silicon and Silicon-Carbide as semi-conductor materials

Source	Si based Conduction Loss	Si based Switching Loss	SiC based Conduction Loss	SiC based Switching Loss	*Δ*Loss Conduction	*Δ*Loss Switching
[91]	0.127 Ω	5.5 mJ	0.166 Ω	0.282 mJ	+30.7%	-94.9%
[92]	550.8 W	0.105 Ws	750.0 W	0.023 Ws	+36.2%	-78.4%
[93]	244.1 W	333.5 W	377.9 W	56.8 W	+54.8%	-83.0%
Averaged loss change between Si and SiC					*+40.6%*	*-85.4%*

3.3.2 DC-DC Converter Design

In an electrical network converters are required to change a (varying) input voltage to a nearly constant output voltage and different voltage levels compared to the input. For the conversion process two different converter types are available: isolated and non-isolated converters. Isolated converter means that the input and the output are galvanically isolated from each other and the energy is transferred with the help of magnetic components (e.g. inductances). Non-isolated systems are sharing a common ground [94]. Isolated converters have the drawback that efficiencies over 90% are hard to reach due to the transformer architecture [94]. Therefore, the focus in this section is set to the performance simulation and mass estimation of non-isolated converters, although these systems require additional protection devices. The main components of non-isolated converters are PS, diodes and inductors. To filter and smooth possible voltage ripples, capacitors are used at the input and the output. The simplest way to control the PS is performed via PWM [94]. For that purpose a micro-controller is used, which controls the switching elements in a way that the electric current is chopped appropriately. This chopping mechanism is controlled via the timely length of a pulse of the voltage and current. Depending on the configuration of these components, different converter architectures can be realized. The most common ones according to [94] are:

- Buck converters, which convert the input voltage to a lower output voltage level
- Boost converters, which convert the input voltage to a higher output voltage level
- Buck-boost converters, which are a combination of the buck and boost converters

Figure 3.13 shows the principle layouts for different DC-DC converter types. In case of a buck converter shown in (a), the PS is controlled in a way that the average output voltage is lower than the input voltage. During on time of the switch the passive components such as inductor and capacitor are charged. If the switch is turned off, the stored energy within the inductor maintains the current flow at the output. In this case the diode is acting as a valve allowing the electric current to flow in one direction. The capacitors are used as filter elements to smooth the input and the output voltages. The second converter type, the

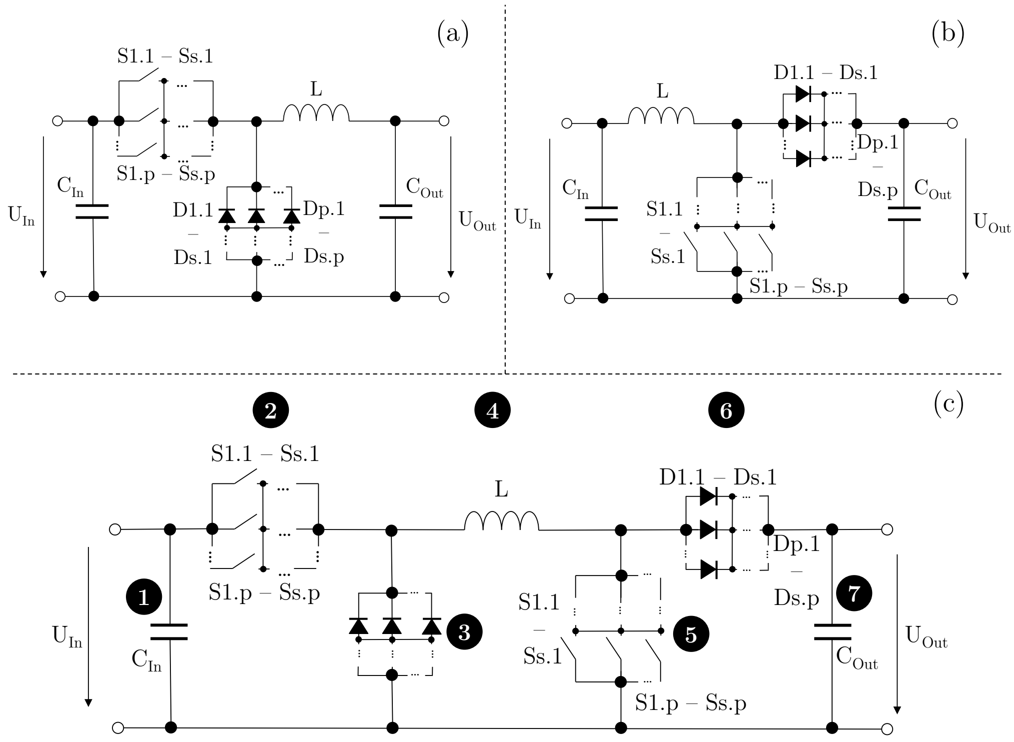

Figure 3.13: Simplified multi-level DC-DC converter for high power applications based on [89, 95]. (a) buck converter (b) boost converter (c) buck-boost converter

step-up or boost converter, shown in Figure 3.13 (b) increases the output voltage compared to the input. During on time of the PS S.1.1-Ss.p the inductor is charged. If the PS is turned off the inductor will maintain the current flow due to the stored energy. In this way it acts as a voltage source which is connected in series with the main input voltage source and is therefore increasing the output voltage. Figure 3.13 (c) shows a combination of the buck and the boost converter by combining both circuits to the buck-boost converter. This circuit is able to convert a lower and a higher input voltage to a target output voltage.

An important descriptor to define the duration of operation of the different semi-conductors and passive electric component types is the duty cycle, DCy. It is defined as the following [89]

$$\begin{aligned} \text{Buck converter: } DCy &= \frac{t_{On}}{T} = \frac{U_{Out}}{U_{In}} \\ \text{Boost converter: } DCy &= \frac{t_{On}}{T} = 1 - \frac{U_{In}}{U_{Out}} \end{aligned} \tag{3.43}$$

where t_{On} represents the on-time slope of the PS until the switch has reached its target voltage, T the period of a total on and off switch period. This expression can be also transferred in case of a buck converter to the ratio of the target output voltage, U_{Out}, to the input voltage, U_{In}, for boost mode vice versa. The design *DCy* depends on the input voltage range, U_{In}, to be covered. For a battery powered electric architecture the converter should be able to handle all battery output voltages depending on the different *SOCs* and *C-rates* (from maximum to U_{Cutoff}). Based on the input and output voltages the corresponding electric currents, I_{In} and I_{Out}, can be determined with Equation (3.44)

$$\begin{aligned} I_{In} &= \frac{P_{In}}{U_{In} \cdot n_{Parallel}} \\ I_{Out} &= \frac{P_{In} \cdot \eta_{Conv}}{U_{Out} \cdot n_{Parallel}} \end{aligned} \tag{3.44}$$

The number of PS and diodes are connected in parallel and in series to handle the high power and high voltage requirements. The number of components connected in parallel, $n_{Parallel}$, are defined by the electric current and the components connected in series, n_{Series}, have to handle the voltage. This architecture is referred to a simplified multi-level converter. The number of required switches is determined with Equation (3.45)

$$\begin{aligned} n_{Parallel} &= \left\lceil \frac{I_{Design}}{I_{max,Ref}} \right\rceil \cdot n_R \\ n_{Series} &= \left\lceil \frac{U_{Design}}{U_{max,Ref}} \right\rceil \end{aligned} \tag{3.45}$$

The maximum values for the current, $I_{max,Ref}$, and the voltage, $U_{max,Ref}$, are depending on the used components according to their data sheet definitions. The brackets represent a round up to the next integer value. To ensure a higher reliability of the converter in case of a failing switch, the minimum number of required parallel switches is multiplied via a redundancy factor, n_R. This approach allows single switches to fail without influencing the operation of the converter. In normal operation the electric current is distributed to all installed switches, reducing the load current for each single switch. In the first instance, the losses of one PS and one diode are used for the efficiency calculation and multiplied by the total number of installed components assuming that the other components connected in series and in parallel show the same behavior.

The PS controls the electric current through the converter. This control process is not lossless. For the estimation of the conduction power losses of the PS, $PL_{Cond,PS}$, Equation (3.41) is used including the voltage characteristics of the PS and *DCy* indicating the operating time of the switch according to [89]

$$PL_{Cond,PS} = \left(I_{PS} \cdot U_{CE0,PS} + I_{PS}^2 \cdot r_{CE,PS} \right) \cdot DCy \tag{3.46}$$

This simplified equation is valid for a constant operating temperature of the components and neglects the ripple current at the output. Besides the conduction losses, the corresponding switching power losses, $PL_{SW,PS}$, are calculated according to Equation (3.42) using the corresponding design currents and voltages of the switch. These values are corrected by the number of switches in series according to [89] as indicated in Equation (3.47)

$$PL_{SW,PS} = f_{SW} \cdot E_{On+Off,PS,Ref} \cdot \left(\frac{I_{PS}}{I_{PS,Ref}}\right)^{K_{I,PS}} \cdot \left(\frac{U_{PS}}{U_{PS,Ref} \cdot n_{Series}}\right)^{K_{V,PS}} \tag{3.47}$$

For the conduction and switching power losses of the diode the same approach is used, taking the corresponding diode parameters. The diode conduction power losses, $PL_{Cond,D}$, are calculated according to [89] with

$$PL_{Cond,D} = \left(I_D \cdot U_{F0,D} + I_D^2 \cdot r_{F,D}\right) \cdot (1 - DCy) \tag{3.48}$$

The PS and the diode are successively operating. This means that if the PS is switched off the diode is carrying the electric current considered by the term *1-DCy*. The diode switching power losses, $PL_{SW,D}$, are also derived according to [89]

$$PL_{SW,D} = f_{SW} \cdot E_{rr,D,Ref} \cdot \left(\frac{I_D}{I_{D,Ref}}\right)^{K_{I,D}} \cdot \left(\frac{U_D}{U_{D,Ref} \cdot n_{Series}}\right)^{K_{V,D}} \tag{3.49}$$

Depending on the converter type the used design currents, voltages and power coefficients are listed in Table 3.8. These parameters have been calibrated with the online available simulation tool SemiSel from the manufacturer Semikron [90]

The total losses of the semi-conductor components are finally derived with Equation (3.50)

$$PL_{SC,Total} = (PL_{Cond,PS} + PL_{SW,PS} + PL_{Cond,D} + PL_{SW,D}) \cdot n_{Parallel} \cdot n_{Series} \tag{3.50}$$

Beside the PS and the diodes, other passive components are required for a converter design to smooth for example U_{Out} and to reduce possible fluctuations of U_{In}. The inductor shown in Figure 3.13 is a central part of the conversion process. The main sizing parameter for the inductor is the maximum electric current that depends on the used converter type. The inductor for all converters is sized for continuous-current mode. This operation mode means that the stored energy of the inductor is sufficient to keep the current flow stable during discharge [96]. For the buck converter the low voltage side is at the output, and for the boost converter at the input. With the sizing current, $I_{Ind,max}$, the required inductance current

Table 3.8: Sizing currents and voltages as well as calibrated power factors used for buck and boost converters

Parameter	**Buck (Mode)**	**Boost (Mode)**
I_{PS}	I_{Out}	I_{In}
I_D	I_{Out}^a	I_{In}
U_{PS}	U_{In}	U_{Out}
U_D	U_{In}	U_{Out}
${K_{I,PS}}^b$	1.4	
${K_{V,PS}}^c$	1.6	
${K_{I,D}}^d$	1.0	
${K_{V,D}}^d$	1.4	

[a] Semikron online tool [90] is using I_{In} instead of I_{Out} according to [89]. For calculations I_{Out} is used.
[b] According to [89] value should be around 1
[c] According to [89] value should be between 1.3 and 1.4
[d] According to [89] value should be around 0.6

can be calculated with Equation (3.51) using the Inductor Current Ratio (LIR) according to [96]

$$dI_{Ind,max} = I_{Ind,max} \cdot LIR \tag{3.51}$$

With $I_{Ind,max}$ the required inductance for the buck converter, L_{Buck}, is calculated with Equation (3.52) according to [97]

$$L_{Buck} = \frac{U_{Out} \cdot (1 - DCy_{Design})}{f_{SW} \cdot dI_{Ind,max}} \cdot k_S \tag{3.52}$$

The design duty cycle, DCy_{Design}, is defined as the lowest value for the specified input voltage range and target output voltage. Accordingly, the required inductance for the boost converter, L_{Boost}, is calculated according to methods described by [98]

$$L_{Boost} = U_{In} \cdot \frac{(U_{Out} - U_{In})}{U_{Out}} \cdot \frac{1}{f_{SW} \cdot I_{Ind,max}} \cdot k_S \tag{3.53}$$

The design mode defines the size of the inductance. In off-design the electric current induced by the inductor is determined with Equation (3.54) for the buck mode according to [97] and for the boost mode according to [98]

$$\begin{aligned} dI_{Buck} &= U_{Out} \cdot (1 - DCy) \cdot \frac{1}{f_{SW}} \cdot \frac{1}{L_{Buck}} \\ dI_{Boost} &= \frac{U_{In} \cdot DCy}{f_{SW} \cdot L_{Buck}} \end{aligned} \tag{3.54}$$

Finally, the total current through the inductor of a buck converter, $I_{Ind,Buck}$, is calculated with Equation (3.55) according to [96]

$$I_{Ind,Buck} = I_{In} + \frac{dI_{Buck}}{2} \tag{3.55}$$

For the current through the inductor of the boost converter, $I_{Ind,Boost}$, Equation (3.56) is used according to [98]

$$I_{Ind,Boost} = \left(I_{Out} - \frac{dI_{Boost}}{2}\right) \cdot (1 - DCy) \tag{3.56}$$

The power loss generated by the inductor, PL_{Ind}, during operation is calculated based on the equivalent *Direct Current Resistance (DCR)* of the inductor given in Equation (3.57)

$$PL_{Ind} = I_{Ind}^2 \cdot DCR \tag{3.57}$$

Due to the chopping process, the output voltage shows a ripple waveform caused by the inductor [97]. For that reason, capacitors are used to stabilize the output voltage. The second task of a capacitor is to provide the load with power before the PS reacts. According to [96], this case is not the sizing case for the capacitor and is therefore neglected, in the first instance. For the estimation of the required capacitance, C_{Out}, a certain allowable overshoot tolerance, γ, of the output voltage is defined. This maximum ripple voltage, dU_{ripple}, is estimated with Equation (3.58)

$$dU_{Out,ripple} = U_{Out} \cdot \gamma \tag{3.58}$$

With $dU_{Out,ripple}$ the required C_{Out} for the buck converter can be calculated with Equation (3.59) according to [96]

$$C_{Out,Buck} = \frac{1 - DCy}{\frac{dU_{Out,ripple}}{U_{Out}} \cdot 8 \cdot L \cdot f_{SW}^2} \cdot k_S \tag{3.59}$$

For the boost converter the necessary C_{Out} is estimated according to [98] with Equation (3.60)

$$C_{Out,Boost} = \frac{I_{Out,max} \cdot DCy}{f_{SW} \cdot dU_{Out,ripple}} \cdot k_S \tag{3.60}$$

Furthermore, a safety factor, k_S, is additionally considered as recommended by [96]. The voltage, $U_{C,Out}$, induced by the output capacitor of the buck converter is calculated with Equation (3.61) according to [96]

$$U_{C,Out,Buck} = \frac{1}{2 \cdot C_{Out,Buck}} \cdot \frac{U_{In} - U_{Out}}{L} \cdot \left(\frac{DCy}{f_{SW}}\right)^2 \tag{3.61}$$

The capacitor output voltage is calculated for the boost converter according to [99]

$$U_{C,Out,Boost} = 0.3 \cdot I_{Out} \frac{U_{Out} - U_{In}}{U_{Out} \cdot C_{Out,Boost}} \cdot \frac{1}{f_{SW}} \tag{3.62}$$

With the ripple voltage the *Equivalent Series Resistance (ESR)* of the output capacitor can be derived. The ESR is required for the power loss estimation. The *ESR* is estimated based on [96] and the assumption of an allowable voltage ripple of the output capacitor.

$$ESR_{C,Out} = \frac{dU_{Out,ripple}}{dI_{Ind,max}} \tag{3.63}$$

Finally, the power loss of the output capacitor, $PL_{C,Out}$, is calculated according to [96]

$$PL_{C,Out} = ESR_{C,Out} \cdot dI_{Ind}^2 \tag{3.64}$$

Due to the chopping process of the PS, ripple effects can occur at the input side. To smooth U_{In} a similar approach as for U_{Out} is applied taking the same overshoot voltage tolerance.

$$dU_{In,ripple} = U_{In} \cdot \gamma \tag{3.65}$$

The input capacity, C_{In}, can be finally calculated with Equation (3.66) according to [97]

$$C_{In} = \frac{I_{Out}}{f_{SW} \cdot dU_{In,ripple}} \cdot (DCy - DCy^2) \tag{3.66}$$

Depending on the conversion mode the loss consideration of some components are set to static mode or to zero. For example during buck mode the second PS assembly (component 5) in Figure 3.13 (c) is set to zero and the second diode assembly (component 6) to static mode. In boost mode PS 1 (component 2) is set to static mode and the losses of diode 1 (component assembly 3) to zero. All converter designs are using the same design parameters as listed in Table 3.9.

Table 3.9: Design parameters used for all converter types

Component Parameter	**Value**
Inductor Current Ratio LIR [%]	30 [97]
Inductor Direct Current Resistance DCR [mΩ]	2 [96]
Capacitor Voltage Overshoot Tolerance [%]	+2 [96]
Safety Margin k_S [%]*	+20 [96]
Mass Density of Inductor $1/\bar{\rho}$ [kg/J]	3 [25]
Mass Density of Capacitor $1/\bar{\rho}$ [kg/J]	0.1 [25]
Power Switch Mass [g]	150 [90]
Diode Mass [g]	20 [90]
Mass Service Fraction** [%]	70

* used for inductance and input/output capacitances
** derived from data published by [100]

The mass of the converter is determined by summing up all individual components. The estimation of the mass of the semi-conductors, m_{SC}, including PS and diodes are based on existing components and can be performed with Equation (3.67)

$$m_{SC} = m_{PS} \cdot n_{PS} + k_{Conv,Type} \cdot m_D \cdot n_D \tag{3.67}$$

The single semi-conductor masses are listed in Table 3.9, where the number of PS, n_{PS}, and number of diodes, n_D, are determined with the required number of components needed in series and parallel depending on the individual maximum values. The parameter, $k_{Conv,Type}$, represents the converter type, 1 for buck and boost converters, 2 for buck-boost converters, assuming the same number of diodes for both voltage sides. The mass of the inductances is calculated with the stored energy. This energy is calculated with Equation (3.68)

$$E_{Ind} = \frac{1}{2} \cdot L \cdot I_{Ind,max}^2 \tag{3.68}$$

The mass of the inductor, m_{Ind}, can then be calculated with the corresponding mass density, $1/\bar{\rho}_{Ind}$, given in Equation (3.69)

$$m_{Ind} = E_{Ind} \cdot \frac{1}{\bar{\rho}_{Ind}} \tag{3.69}$$

The same approach is also used for the capacitors. The energy one capacitor can store, is calculated with the common energy Equation (3.70)

$$E_C = \frac{1}{2} \cdot C \cdot U_C^2 \tag{3.70}$$

The masses of the capacitors, m_C, are determined with the corresponding mass density, $1/\bar{\rho}_C$, given in Equation (3.71)

$$m_C = (E_{C,In} + E_{C,Out}) \cdot \frac{1}{\bar{\rho}_C} \tag{3.71}$$

Finally, the total converter mass, m_{Conv}, is corrected with the fractions for services, k_{Serv}, and cables, k_{Cables}, see Equation (3.72). The service fraction, k_{Serv}, covers all secondary components such as frames, mountings, platines, controllers, heat sinks etc. and is set to 2.5. This factor has been derived by published data according to [101].

$$m_{Conv} = (m_{SC} + m_{Ind} + m_C) \cdot (1 + k_{Serv}) \cdot k_{Cables} \tag{3.72}$$

With the described methods, the model was validated against the software SemiSel of Semikron [90]. The results of this validation are shown in Figure 3.14.

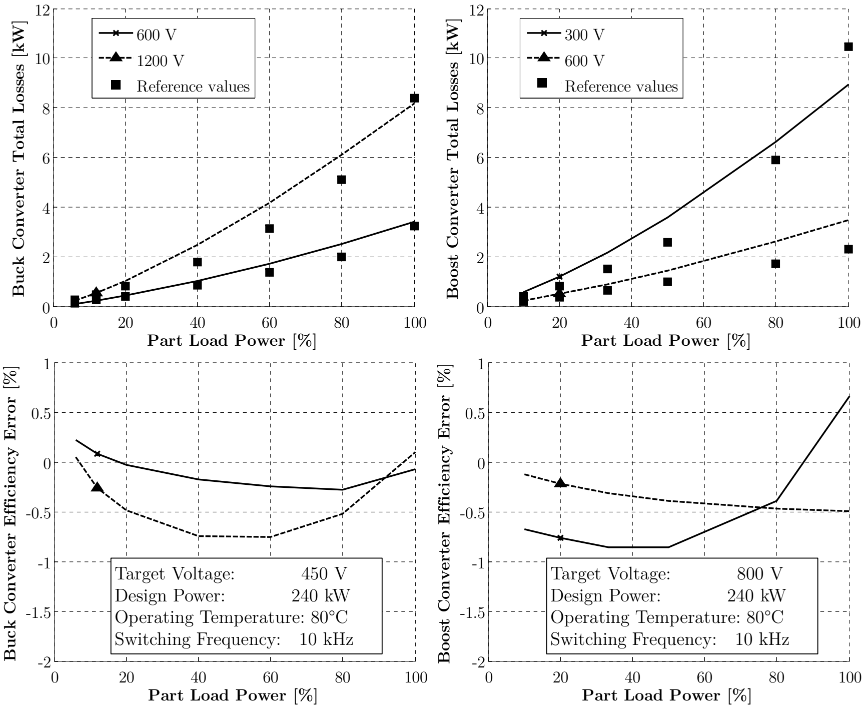

Figure 3.14: Total loss and efficiency validation of buck and boost converter against performance calculation of [90]

The validation includes a comparison of the total losses of each converter type at the specified design power for different converter types, part load conditions and input voltage ranges. It can be recognized that the calculated total losses of the buck converter meets the reference values at design power with a deviation of -2.7%. In part load conditions the calculated losses are higher than the reference values. This is mainly caused by the simplification that the converter is running at constant operating temperature while the Semikron tool uses the actual temperature levels. The boost converter is showing higher deviations than the buck converter. In the worst case there are deviations of the total losses of up to 50%. Nevertheless, the trends concerning input voltage and part power demands are in the same order of magnitude as the reference tool. However, comparing the maximum deviation with regard to the overall efficiency between the used model and the commercial software shows a deviation of less than 1%, which is accurate enough for the present study.

Figure 3.15 shows the impact of the switching frequency of the PS on the overall converter mass and efficiency for the three different converter types. These charts have been produced with the described models and are showing the design space for different output powers.

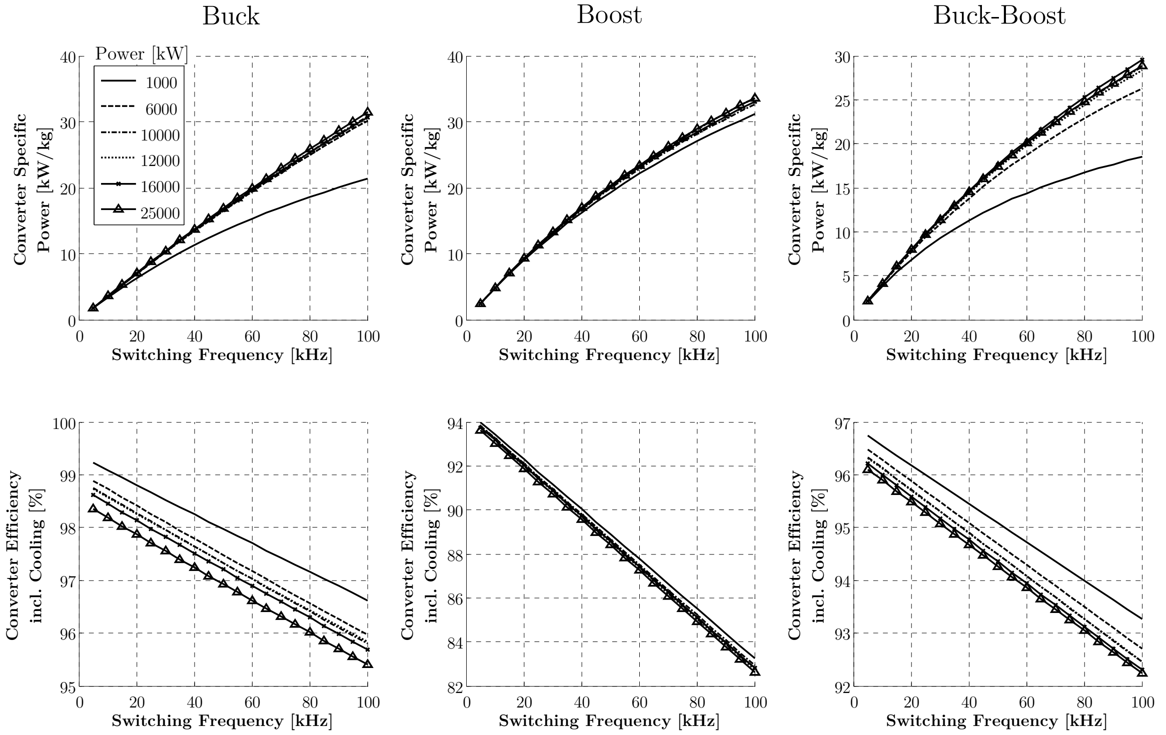

Simulation Settings
Target voltage 2000V, operating temperature 100°C, semi-conductor material: Silicon carbide

Figure 3.15: Mass and efficiency trends of the converter types for different power and switching frequency ranges

The common behavior of all types is that with increasing switching frequency at constant output power the mass and efficiency decreases. The mass reduction is in this case represented by an increase of the specific power at constant output power. The decreasing mass is caused by the smaller sized inductances and capacitors, because the higher the switching frequency the less energy these components have to store. However, the higher switching frequency also causes higher switching losses and impacts the cooling system. The buck converter offers the highest efficiency in this scenario with specific powers of up to 30 kW/kg. The boost converter delivers a lower efficiency at higher mass than the buck converter. The buck-boost converter is the heaviest solution of these types. It delivers in the design case a better efficiency than the boost converter, but still lower than the buck converter. The values achieved with the current approach seem to be in feasible regions. Efficiency values of up to 98.9% at specific powers of 62 kW/kg could already be demonstrated in the automotive sector with bidirectional DC-DC converters using SiC at 200 kW output power [102].

3.3.3 Motor Inverter-Controller

An externally excited electric motor needs a control unit to deliver a specific speed and torque demand within the specified operational envelope. This unit supplies the motor with the required sinusoidal current wave form at a certain frequency and amplitude. For this purpose an inverter-controller unit is required that changes, for example, the electric current type from an input DC to an output AC. The most common inverter is the pulse control or Voltage Source Inverter (VSI) to generate a three phase AC voltage using a DC current source such as batteries. The typical architecture of the VSI, also called B6 bridge inverter, is sketched in Figure 3.16.

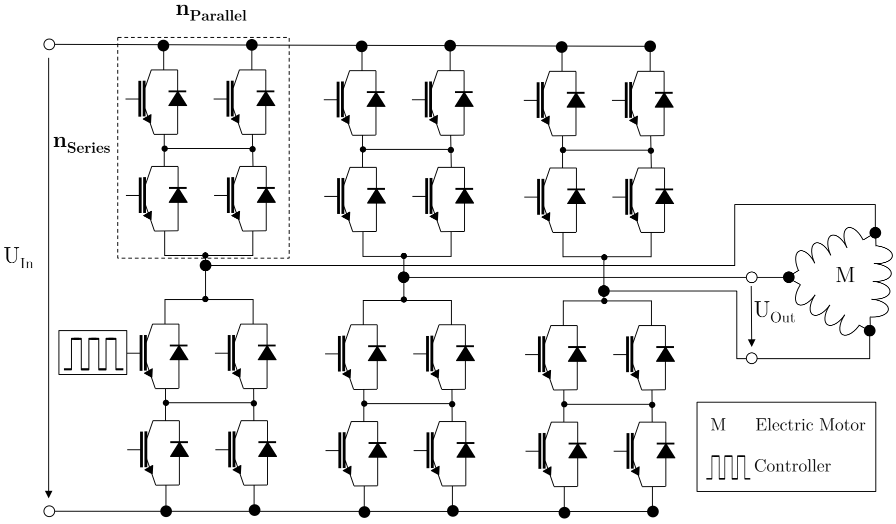

Figure 3.16: Simplified multi-level DC-AC inverter-controller unit for 3-phase high power electric motors

A typical VSI consists of PS and diode rectifiers. These components can be connected in parallel, $n_{Parallel}$, and/or in series, n_{Series}, for high power applications according to the operating power and input voltage, U_{In}, and redundancy aspects, and, furthermore, can be grouped in modules. The configuration in this thesis is defined as simplified multi-level inverter-controller. With these modules the electric current is controlled in a way that the coils of the electric motor are either energized in a positive or a negative electric current flow direction depending on the modules conduction state (blocking or conduction mode). This switching process generates an electric current flow that induces an electric field in the motor coils and interacts with the rotor field of the electric motor. The control of these PS is also performed via the PWM to approximate the aforementioned sinusoidal waveform of the electric current.

Chopping the electric current with PS via PWM is normally not lossless. Conduction and switching losses occur at the PSs and diodes during this control process. The model for these losses is based on an existing PS and uses scaling dependencies for the efficiency estimation according to [89]. This proposed model requires the following assumptions for the PS and diodes:

- switching times are neglected
- temperature is set constant to 463 K (150°C)
- switching frequency ripple of the AC current is neglected
- switching frequency has to be orders of magnitudes higher than the output frequency
- usage of linear modulation

Based on this method, a PS is limited by its peak current, $\hat{I}$, and peak input voltage, $\hat{U}_{In}$, specified in the corresponding data sheet (I_{Ref} and U_{Ref}) of the used PS. Designing the VSI only for motor control, $\hat{I}$ can be calculated with Equation (3.73) using the motor design power, P_{Design}, and motor design voltage, U_{Mot}, and the power factor, $cos\phi$, of the inverter.

$$\hat{I} = \frac{P_{Design}}{\eta_{Mot} \cdot U_{Mot} \cdot \sqrt{3} \cdot cos\phi} \cdot \sqrt{2} \tag{3.73}$$

The PSs and diodes can be grouped in modules. Within these modules the PSs and diodes can be further connected in series and/or parallel, if one or all design parameters are exceeding a limit of a specified component. This is demonstrated in Equation (3.74) using additionally the parameter n_R as redundancy factor, similar to the converter design.

$$\begin{aligned} n_{Parallel} &= \left\lceil \frac{\hat{I}}{I_{Ref}} \right\rceil \cdot n_R \\ n_{Series} &= \left\lceil \frac{\hat{U}_{In}}{U_{Ref}} \right\rceil \end{aligned} \tag{3.74}$$

In general, two main losses occur in a VSI, conduction and switching losses of the PSs and diodes. The conducting losses of one PS, $P_{Cond,PS}$, of a VSI can be calculated with Equation (3.75) according to [89]

$$P_{Cond,PS} = \left(\frac{1}{2\pi} + \frac{\Theta \cdot cos\phi}{8}\right) \cdot \frac{I}{n_{Parallel}} \cdot U_{CE0} + \left(\frac{1}{8} + \frac{\Theta \cdot cos\phi}{3\pi}\right) \cdot \left(\frac{I}{n_{Parallel}}\right)^2 \cdot R_{CE} \tag{3.75}$$

$P_{Cond,PS}$ depends on the threshold voltage, U_{CE0}, and the forward slope resistance, R_{CE}, of the used PS. The equation also represents the off-design characteristic and, therefore, the actual electric current through the collector is used instead of $\hat{I}$. The modulation index, Θ, represents according to [89] the virtual neutral point from the phase-neutral voltage of the load. It is calculated according to [103] and is dependent on the actual motor voltage U_{Mot} (output voltage) and the input voltage, U_{In}, as shown in Equation (3.76).

$$\Theta = 2 \cdot \frac{\sqrt{3}}{3} \cdot \frac{U_{Mot}}{U_{In}} \tag{3.76}$$

The second main loss contributors are the switching losses, $P_{SW,PS}$, of one PS. These losses are caused by the chopping mechanism, and can be determined with Equation (3.77) according to [89]

$$P_{SW,PS} = E_{Tr} \cdot \frac{I}{n_{Parallel} \cdot I_{Ref}} \cdot \left(\frac{U_{In}}{n_{Series} \cdot U_{CE,Ref}}\right)^{K_{V,PS}} \cdot f_{SW,Cont} \tag{3.77}$$

This method uses a scaling approach of the operating line of a PS based on the average switching energy (on and off), E_{Tr}. Normally, the E_{Tr} is also affected by surroundings such as stray inductances of motor cables or filter capacitors. In the first instance, these effects are neglected. E_{Tr} is scaled with the actual electric current, the reference current and U_{In} for one switch and module to the reference voltage, $U_{CE,Ref}$. The power factor, $K_{V,PS}$, for the voltage can be used to calibrate the operating line based on an existing PS. Finally, the scaled E_{Tr} is multiplied by the number of switches per second, $f_{SW,Cont}$, induced by the controller. The required $f_{SW,Cont}$ is estimated according to Equation (3.78) and is depending on n_{Mot}, p and, furthermore, on the discretization factor, k_P. This factor represents the number of pulses generated by the controller per period.

$$f_{SW,Cont} = n_{Mot} \cdot p \cdot k_P \tag{3.78}$$

The scaling method of the switching behavior is only valid for $f_{SW,Cont} >> n_{Mot}$ [89]. For that reason the parameter k_P is assumed to be 100 for all inverter designs. Beside the PS, the diodes are also generating heat caused by conduction and switching losses. The conduction losses of the diodes can be estimated in a similar way as for the PS using Equation (3.79) according to [104]

$$P_{Cond,D} = \left(\frac{1}{2\pi} - \frac{\Theta \cdot cos\phi}{8}\right) \cdot \frac{I}{n_{Parallel}} \cdot U_{F0} + \left(\frac{1}{8} - \frac{\Theta \cdot cos\phi}{3\pi}\right) \cdot \left(\frac{I}{n_{Parallel}}\right)^2 \cdot R_F \tag{3.79}$$

U_{F0} is the on-state voltage across the diode and R_F is the forward resistance of the diode [105]. The switching losses are estimated using the same scaling approach as for the PS with the switching energy of the diode, E_D, shown in Equation (3.80) according to [89]

$$P_{SW,D} = \frac{E_D}{\pi} \cdot \left(\frac{I}{n_{Parallel} \cdot I_{F,Ref}}\right)^{K_{I,D}} \cdot \left(\frac{U_{In}}{n_{Series} \cdot U_{F,Ref}}\right)^{K_{V,D}} \cdot f_{SW,Cont} \tag{3.80}$$

The power factor for the electric current scaling, $K_{I,D}$, and for the voltage scaling impact, $K_{V,D}$, are used to calibrate the switching behavior of the diode based on an existing operating curve. Finally, the total inverter efficiency, η_{Inv}, is determined with Equation (3.81) by summing up all single losses of the PS and diodes of one module multiplied by the total number of installed modules. Because only three phase electric motors are considered, the VSI represents a six H-bridge. This means that in total six modules are installed and is therefore dependent on the architecture of the electric motor.

$$\eta_{Inv} = \frac{P_{Out}}{P_{In}} = \frac{P_{Out}}{P_{Out} + (P_L \cdot n_{Series} \cdot n_{Parallel}) \cdot 6} \tag{3.81}$$

$$\text{with } P_L = P_{Cond,PS} + P_{SW,PS} + P_{Cond,D} + P_{SW,D}$$

Based on the number of required modules and in turn PS and diodes, the mass of the required switches, $m_{Switches}$, can be calculated by using, in the first instance, the mass of one existing PS, m_{PS}, multiplied by the number of switches in parallel and in series. To take also account for additional equipment such as heat sinks, mountings and housing the calculated mass is multiplied with k_{Serv}. This parameter is set to the same value as used for the converter design. The described approach is shown in Equation (3.82)

$$m_{SC} = (6 \cdot n_{Parallel} \cdot n_{Series} \cdot m_{PS}) \cdot k_{Serv} \tag{3.82}$$

For the calculation of the total mass of the VSI, m_{Inv}, the m_{SC} is further extended by a cable mass factor, k_{Cables}, of 1.2 of the total equipped PS mass derived from data published by [101]

$$m_{Inv} = m_{SC} \cdot k_{Cables} \tag{3.83}$$

The inverter model using the reference data of the IGBT was validated against the tool SemiSel from [90] for a given design output power of 300 kW at 400 V with 50 Hz and for two different input voltages (shown in Figure 3.17). The total loss error including conduction and switching losses deviates from the tool up to 15% for part loads below 40% of the design power. The deviation increases for higher input voltages. Above 40% part load power the deviation stays in a range of ±5%. The deviation is mainly driven by the assumption that the temperature is constant, which the SemiSel tool takes into account as mentioned in Section 3.3.2. However, focusing on the overall efficiency of the inverter the high deviation of the losses can be neglected, because the resulting efficiency error is outside of the overall model accuracy (see Figure 3.17, right).

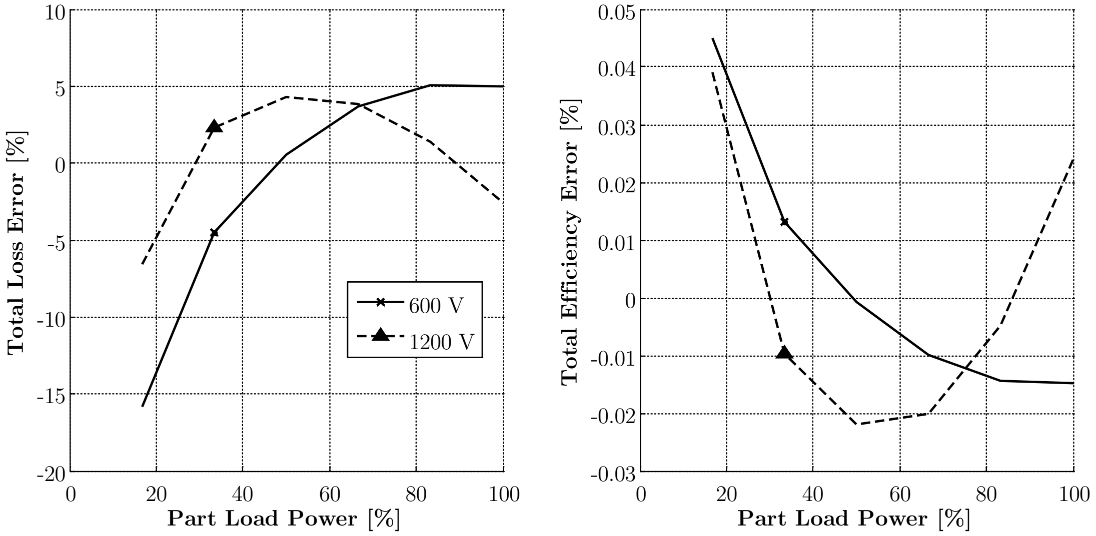

Simulation settings
- Target voltage 400V @ 50Hz
- Output power 300kW
- Operating temperature 150°C (constant)
- Switching frequency 10kHz

Figure 3.17: Comparison of the inverter model with the performance data provided by the tool SemiSel [90] for different input voltages. Left: total loss error; Right: total efficiency error

Based on the described modeling approach, a design space exploration has been performed for various output powers and different input voltages at a constant target output voltage as shown in Figure 3.18. The target output voltage represents the voltage level used for the architectural design space exploration described in Section 5.2. The resulting design efficiency ranges between 98% and 99.5% and the specific power between 12 kW/kg up to 50 kW/kg. It can be recognized that the efficiency and specific power decreases with increasing input voltage at fixed output voltage. With increasing design power the specific power is increasing. The discontinuities are caused by the serial and parallel arrangement of the PS.

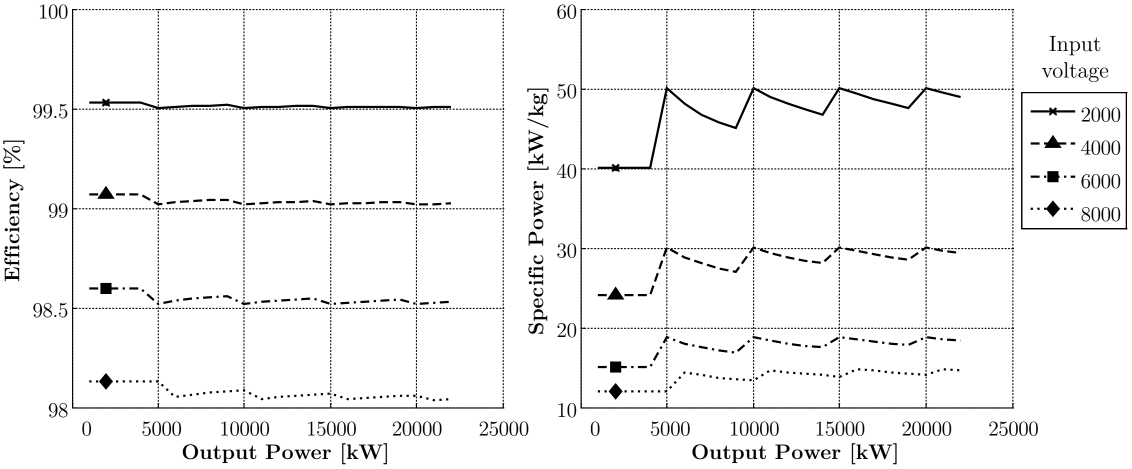

Simulation settings
- Target voltage 1000V @ 50Hz for 2 pole pair electric motor
- Operating temperature 150°C (constant)
- Switching frequency 10kHz
- Redundancy factor 2

Figure 3.18: Efficiency (left) and specific power (right) estimation for different sizing powers and input voltage ranges

3.4 Protection Devices

Protection devices play a central role in an electric system architecture, because they are required to protect the overall system in a failure case. Depending on the device type they are able to disconnect a disabled component from the network. Although these systems are essential, the biggest disadvantage is the high mass impact in the relevant power and voltage range required for aircraft. Current electric systems to supply subsystems on board of an aircraft are in a range of 270 VDC and power levels below 1000 kW (e.g. Boeing 787)[65]. Normally, Electromechanical Circuit Breakers (EMCB) are used as main protection device in conventional electric systems [65, 106]. For higher power and voltage systems Solid-State Circuit Breakers (SSCB) or Solid-State Power Controllers (SSPC) are integrated to protect the system as for example used in the B787 [37]. SSPC have a faster operating time [37] compared to EMCB. This means that in case of a failure a component or a disabled system can be disconnected faster from the network. A general rule states that the faster the protection device acts, the less fault energy has to be absorbed and, in turn, the lighter the component can be designed. In an electric network the following failure types can occur

- Fault current: An unresistant connection between two nodes with different potential.
- Over voltage: Deviation from the nominal voltage, which can be symmetrical or asymmetrical.

- Over power: A load pulls more power than the system is designed for.
- Parallel and serial arcs [107]: Lightning arcs are a serious challenge for the aviation industry. Due to the high altitude and, in turn, low air density, the occurrence of lightning arcs increases according to Paschen's law [15]. It can be distinguished between two types of lightning arcs: serial and parallel. Serial lightning arcs occur in series of, for example, a void of a cable and their detection is difficult. A parallel lightning arc occurs in general between a source and the ground or another cable. The fault power is limited only by the internal resistance of the power source and in turn high fault powers and temperatures can occur. For high power applications with electric currents above 500 A using AC the likelihood of parallel arcs are most probable, while series arcs can be neglected [107]. In DC networks series arcs are more difficult to detect, because the current has no zero crossing [108] and the detection cannot be described analytically, because its behavior is chaotic and random [109].
- Faulty operation: This failure type happens if a component operates outside of its specified conditions and is only detectable in combination with a health-monitoring system.

Figure 3.19 gives an overview of possible protection devices including their operating times. Beside EMCB and SSPC also Hybrid Circuit Breakers (sHCBs) are compared that are a combination of EMCB and SSPC.

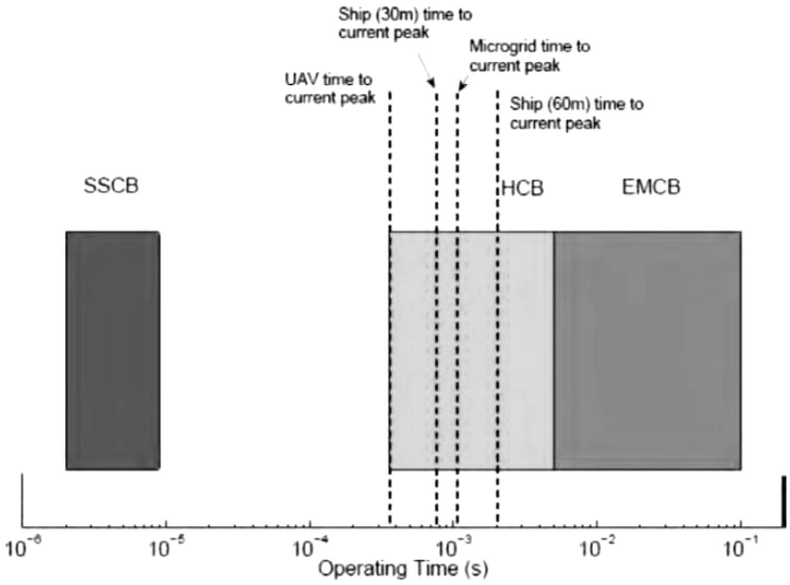

Figure 3.19: Comparison of the operating times of different circuit breaker types taken from [106]

Armstrong et al. [37] analyzed the mentioned protection devices for a 50 MW turbo-electric propulsion system including a potential cryogenic operation. A summary of the compared devices is given in Table 3.10.

Table 3.10: Comparison of DC protection devices for aircraft application, taken from [37]

Parameter | Device	EMCB	HCB	SSCB
Operating time	0	+1	+3
Mass	0	+3	+3
Conduction resistance	0	-1	-3
Cryogenic operation	0	+3	+3

-3 strongly negative; -1 negative ; 0 neutral; +1 positive; +3 strongly positive

Considering the trade-offs between mass and efficiency, the SSCB or SSPC seem to be the most promising solution. The relative high conduction losses are a challenging disadvantage of this protection device. This requires an active cooling system for the considered power ranges. For the scope of this study only SSPCs are considered. The mass and efficiency estimation of this protection device consider two different architectures of switches and protection devices as shown in Figure 3.20.

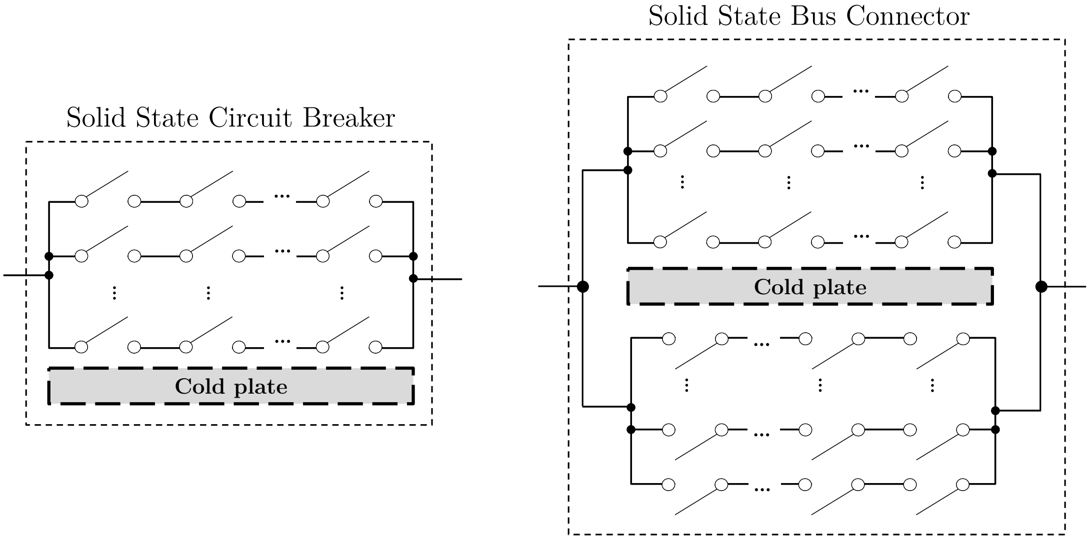

Figure 3.20: Design of a solid-state circuit breaker (left) and a solid-state bus connector (right) based on [18]

In the first instance, to estimate the mass and efficiency of the circuit breakers, the number of required switches is determined with the maximum electric current and voltage. The cold plate is used to connect the PSs to the liquid cooling system, which is further described in Section 3.6.1. The cold plate is normally the heaviest part of the entire protection switch assembly. In case of bi-directional switches, as shown with the crosslink connector or solid-state bus connector, the switches can be arranged in a way that they share the same cold plate to save overall system mass. The required number of parallel and serial connected single switches is calculated with Equation (3.84)

$$n_{Parallel} = \left\lceil \frac{\hat{I}_{Design} \cdot k_{FCM}}{I_{PS,max}} \right\rceil \cdot n_R \qquad (3.84)$$

$$n_{Series} = \left\lceil \frac{\hat{U}_{Design}}{U_{PS,max} \cdot K_S} \right\rceil$$

The number of parallel connected switches is depending on the maximum current, $\hat{I}_{Design}$, through the component, the component specific fault current multiplier, k_{FCM}, according to Table 3.11, the redundancy factor, n_R, and the maximum design current of one PS, $I_{PS,max}$. A fault current multiplier is used to take account for uncertainties and transient behavior during a fault. As minimum the value 2 is used for the k_{FCM}. For the estimation of the number of required switches in series the maximum voltage, $\hat{U}_{Design}$, over the component is used and the maximum allowable voltage, $U_{PS,max}$, of the PS corrected by a voltage safety factor, K_S, of 0.5.

Table 3.11: Used fault current multipliers based on maximum electric current of component

Component	**Fault Current Multiplier,** k_{FCM}
Battery	10 · module capacity [Ah] [110]
Converter	2 [37]
Controller	2 [37]

Based on the mentioned design approaches for the SSCB and the crosslink, the mass of the PS for each single system is estimated with Equation (3.85)

$$m_{SC} = m_{PS} \cdot n_{Parallel} \cdot n_{Series} \cdot k_{Type} \qquad (3.85)$$

m_{PS} represents the mass of one PS according to the table shown in Section 3.3.1 and k_{Type} represents the component type, 1 for the SSCB and 2 for the bidirectional crosslink. The final mass of the overall protection device or crosslink is calculated with Equation (3.86) considering a fraction for services, k_{Serv}, such as housing, cold plates and cables, k_{Cables}. The same numbers as used for the converter and inverter design are taken (see Section 3.3.3).

$$m_{Protection} = m_{SC} \cdot (1 + k_{Serv}) \cdot k_{Cables} \qquad (3.86)$$

The efficiency is calculated according to the methods described in Section 3.3.1 considering only the conduction losses of the circuit breaker in normal mode of operation. As shown in Figure 3.21, the efficiency can be assumed constant in the considered design space. The specific power is increasing with increasing system voltage level and reaches values up to

26 kW/kg. According to [37] values of up to 250 kW/kg can be reached, if cryogenic protection devices can be realized.

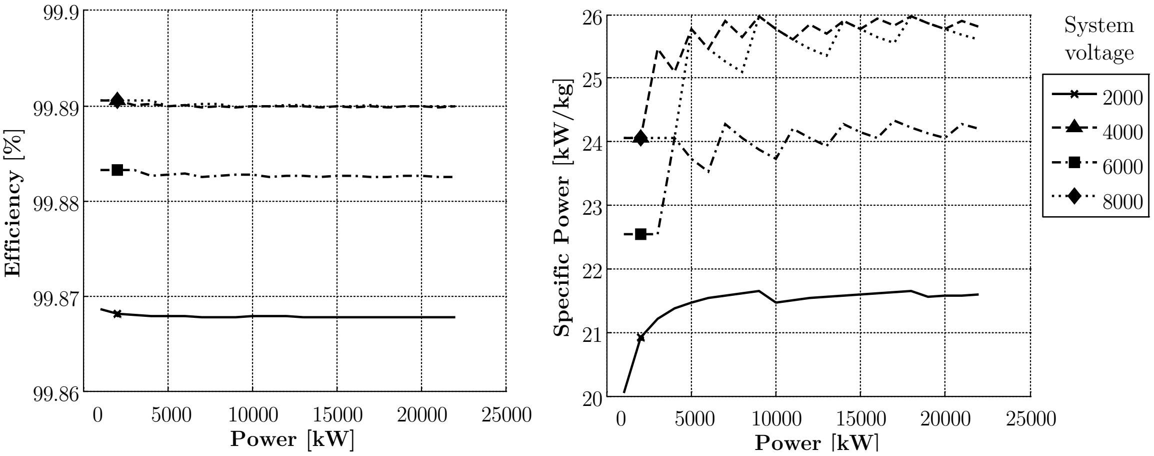

Figure 3.21: Efficiency (left) and mass (right) estimation for different sizing powers and input voltage ranges

3.5 Transmission Cable

Transmission cables are required for the transfer of the electric power from the EPS to the electric loads and to connect the components. There are different materials for the conductor available such as copper, aluminum or HTS. These types differ in cable design, mass and also cooling efforts. The following section describes the modeling approach of cable systems using conventional conducting materials such as copper or aluminum.

A typical layout of a conventional transmission cable can be divided into three main components as sketched in Figure 3.22. The main part is the conductor that is responsible for the electron transfer, followed by the insulation and, finally, the sheath. The sheath protects the cable from environmental effects.

The conductor cross section, A_C, is calculated with the design current and the current density, J, of the used conductor material. The allowable current density is depending on the operating temperature. Normally, a cable is separated in a bundle of small conductors. For simplification reasons only a single conductor is considered as shown in Equation (3.87)

$$A_C = \frac{I_{Design}}{J} \tag{3.87}$$

There are two different types of conductor materials available in aircraft design, the standard copper and aluminum [65]. Copper conductors have a smaller resistance, but a higher material

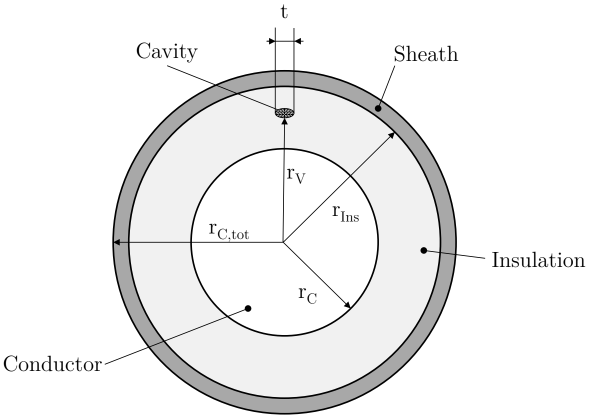

Figure 3.22: Typical design of a conventional transmission cable based on [111]

density. Aluminum conductors are more than three times lighter than copper, but cause higher losses. The most important parameters are summarized in Table 3.12.

Table 3.12: Typical properties of copper and aluminum conductors at room temperature [112]

Parameter	**Copper**	**Aluminum**
Density $[kg/m^3]$	8890	2700
Electrical Resistivity at 293K $[\Omega \cdot m]$	$1.68 \cdot 10^{-8}$	$2.71 \cdot 10^{-8}$

Based on the conductor area, the conductor radius, r_C, can be calculated with Equation (3.88)

$$r_C = \sqrt{k_C \cdot \frac{A_C}{\pi}} \tag{3.88}$$

The parameter k_C is used to correct the conductor cross section to take into account for a bundle of conductor cables, which normally increases the cable diameter due to imperfections of the bundle. Therefore, k_C should be greater than 1. Based on the r_C, the required insulation thickness included in the insulation radius, r_{Ins}, can be calculated with Equation (3.89) based on [111]

$$r_{Ins} = r_C \cdot \exp\left(\frac{U_{Design} \cdot K_S \cdot \kappa \cdot t}{\alpha \cdot r_V}\right) \cdot \left(1 + \frac{t}{r_V}\right)^{1-\kappa} \tag{3.89}$$

The insulation thickness is depending on U_{Design}, the breakdown voltage within the cavity, α, the thickness, t, and the position of the cavity within the insulation, r_V, an additional safety factor to take account for uncertainties, K_S, and, finally, the shape factor, κ, of the cavity. These voids can cause partial discharges that can destroy the insulation over time and are caused by manufacturing uncertainties [111]. Therefore, the insulation has to be designed in a way to be corona free. The shape factor depends on the shape of the cavity and in case of a spherical form, κ of the void can be calculated with Equation (3.90) according to [111].

$$\kappa = \frac{3\epsilon}{1+2\epsilon} \tag{3.90}$$

In this equation ϵ represents the relative dielectric permittivity and is depending on the used insulation material. Typical values for ϵ and densities for the insulation material are listed in Table 3.13 [113].

Table 3.13: Typical insulation materials and their properties [113]

Material	**Material Density** $\rho[kg/m^3]$	**Relative Dielectric Permittivity** ϵ **[-]**
Polyvinyl Chloride	1350	4
XLPE	923	2.3

The total cable radius, $r_{C,Tot}$, is finally determined with Equation (3.91). For the thickness of the sheath, t_{Sheath}, a constant value of 1 mm is assumed.

$$r_{C,Tot} = r_{Ins} + t_{Sheath} \tag{3.91}$$

Based on the cross section of the cable the mass is calculated according to the single volumes of each component and the total length of the cable, l_{Cable}. The conductor mass, $m_{Conductor}$, is determined without the safety factor for the area correction with Equation (3.92)

$$m_{Conductor} = A_{Conductor} \cdot l_{Cable} \cdot \rho_{Conductor} \tag{3.92}$$

The required insulation mass, m_{Ins}, for the specified design voltage can be calculated with Equation (3.95)

$$m_{Ins} = (r_{Ins}^2 - r_{Conductor}^2) \cdot \pi \cdot l_{Cable} \cdot \rho_{Ins} \tag{3.93}$$

The sheath mass, m_{Sheath}, is determined with Equation (3.94) and the corresponding sheath density, ρ_{Sheath},

$$m_{Sheath} = (r_{C,tot}^2 - r_{Ins}^2) \cdot \pi \cdot l_{Cable} \cdot \rho_{Sheath} \tag{3.94}$$

Finally, the total cable mass, m_{Cable}, is the sum of the single components

$$m_{Cable} = m_{Conductor} + m_{Ins} + m_{Sheath} \tag{3.95}$$

The efficiency of the transmission cables, η_{Cable}, and implicitly the power loss, $P_{L,Cable}$, is only depending on the electrical resistance, R, and the length of a DC cable. The power loss also corresponds to the voltage loss, $U_{L,Cable}$, over the cable and is equal to the efficiency, η_{Cable}. It is calculated with Equation (3.96) using the correction factor, k_{Phase}, equals 2 for a single phase, and 1 for a three phase cable (like for electric motor supply) according to [114]

$$\begin{aligned} U_{L,Cable} &= k_{Phase} \cdot \frac{R \cdot l_{Cable}}{A_{Conductor}} \cdot I \\ P_{L,Cable} &= I \cdot U_{L,Cable} \\ \eta_{Cable} &= \frac{P_{In} - P_{L,Cable}}{P_{In}} \end{aligned} \tag{3.96}$$

For high power cables a promising conductor material is HTS as shown by [35] and [46]. A typical design of a DC HTS cable is sketched in Figure 3.23. The main issue of these cables is the required insulation, shielding and cooling effort, in this case performed with liquid nitrogen. The conductor cross section and mass of such a system only accounts for a small portion of the overall cable mass. For that reason, in the first instance, the cable mass is set to 5 kg/m for all power and voltage demands according to [18]. This value is based on a target setting by Brown [46]. This value represents today's specific weight of transmission cables of 270 VDC systems. However, these cable types require a certain cooling effort. Therefore, a cryocooling system is considered to keep the temperature at 70 K with a heat dissipation of 60 W/m [115].

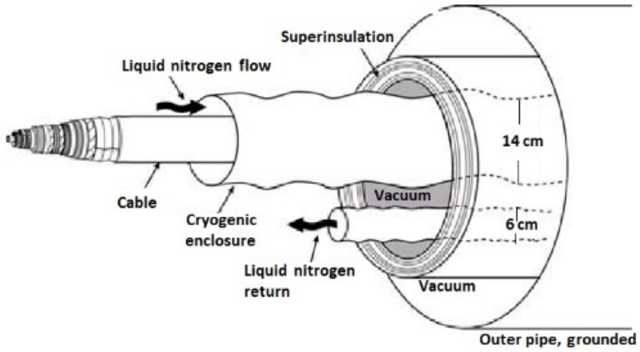

Figure 3.23: Layout of a HTS cable [116]

Based on the presented method, Figure 3.24 represents the specific mass of the different cable types as a function of the transmitted current. The voltage has only a minor impact on the insulation mass and can therefore be set constant for voltage ranges up to 10000 V.

The breakeven point where HTS cables are lighter than copper cables is identified at 1050 A and at 1600 A for aluminum cables. For the presented study this would be at 2.1 MW and at 3.2 MW, respectively. However, the cable masses of the HTS type do not include the additional cooling demand.

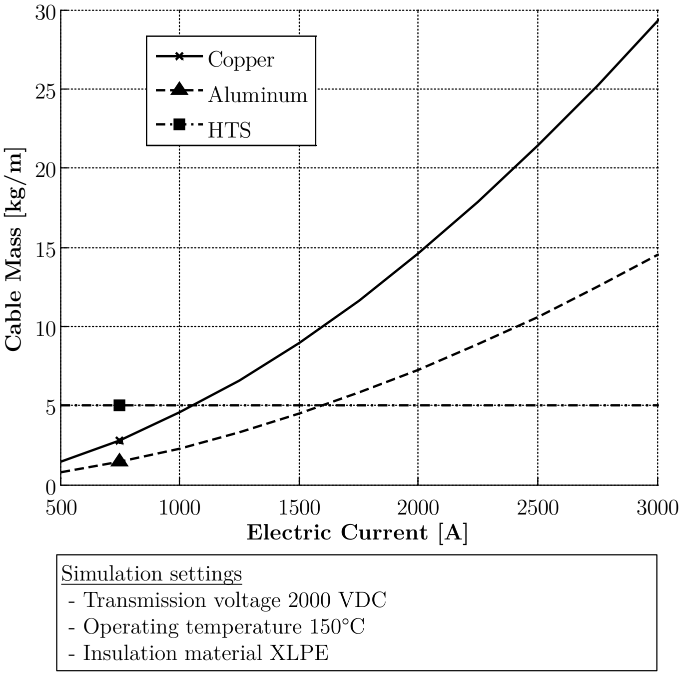

Simulation settings
- Transmission voltage 2000 VDC
- Operating temperature 150°C
- Insulation material XLPE

Figure 3.24: Specific mass of cable types using different conductor materials with XLPE insulation (except HTS cable)

3.6 Thermal Management System

The thermal management system is a central system within an electric power train. All electric components on board of an aircraft are generating heat due to their internal resistance or could be heated up by the environment, which has to be compensated. The thermal management system itself would represent a parasitic loss in the total electric power train, because it is not actively contributing to the propulsive power. Nevertheless, it is responsible that all electric components are kept in their thermal limits during operation. Depending on the required operating temperature there are two different cooling systems considered

- Liquid Cooling Systems, for all power electronics and batteries
- Cryocooling Systems, for operating temperatures below 80 K

The following section describes the estimation of the required cooling power for different cooling types. This includes the mass of these different systems without considering, in the first instance, the transfer of the heat to the surrounding environment.

3.6.1 Liquid Cooling System

For non-cryogenic operating temperatures two different cooling approaches are common: air cooled systems and liquid cooled systems. Liquid cooled systems are normally more complex and heavier than air cooled cooling systems, but allow for higher performances of the cooled components due to the higher cooling efficiency. Therefore, the focus is set on liquid cooling systems for high power non-cryogenic electric components.

Based on [58], a liquid thermal management system can be designed in three basic arrangements: parallel, serial and decentralized. Decentralized systems, where each component or group of components has their dedicated cooling system, seems to be the most promising solution [58]. This approach allows for a smaller sizing of the individual heat exchangers compared to other arrangements such as serial or parallel. Furthermore, the reliability of the overall system can be improved, because an inoperative heat exchanger does not shut down the entire system. For that reason, a simplified cooling model is developed that covers the aspects of required cooling power and mass. The liquid cooling system is modeled as a hydraulic circuit powered by an electrical hydraulic pump. With this design, the necessary electric motor power is determined with the volumetric coolant flow, $\dot{V}$, to transport the ejected heat from the components. The required coolant flow characteristics mainly depend on the three parameters viscosity, μ, density, ρ, and the specific heat, c_P, of a specific coolant type. Table 3.14 gives an overview of several coolant types typically used for electronics.

Table 3.14: Overview of typical coolant characteristics for electronic components taken from [117]

Coolant type	**Viscosity** μ $[kg/m/s]$	**Specific heat** c_P $[J/kg/K]$	**Density** ρ $[kg/m^3]$	**Freezing temperature** T [K]
Aromatic	0.0010	1700	860	193
Aliphatic	0.0090	2150	770	223
Propylene glycol/water (50:50 vol.)	0.0064	3400	1062	236
Methanol/water (40:60 wt.)	0.0020	3560	935	233
Potassium formate/water (40:60 wt.)	0.0022	3200	1250	238

A potential candidate is the single phase fluid potassium formate-water mixture. It provides a high specific heat of 3200 J/kg/K and a medium dynamic viscosity of 0.0022 kg/m/s, but a relative high density of 1250 kg/m^3. Furthermore, the fluid is non-toxic and non-flammable [117]. With these parameters the required cooling pump power can be estimated with $\dot{V}$ using Equation (3.97) including properties of the used coolant type under static operating conditions.

$$\dot{V} = \frac{P_{th} \cdot k_S}{c_P \cdot \rho \cdot \Delta T} \tag{3.97}$$

The heat power, P_{th}, of the electric components is directly determined with the associated efficiency of the component. For the estimation of the required coolant flow a safety factor, k_S, is considered to take account for uncertainties. The temperature difference, $\varDelta T$, is the difference between the mean coolant and the component temperature and implicitly represents the heat exchanger performance. In the first instance, $\varDelta T$ is set constant and independent of Mach number and altitude.

Finally, the required electric pump motor power is estimated using a simplified form of Gibbs fundamental equation, which is adjusted for energy flow as shown with Equation (3.98) according to [58]

$$P_{Elec} = \dot{G} = \dot{V} \cdot dp \tag{3.98}$$

Substituting $\dot{V}$ with Equation (3.97) and taking account for the losses of the hydraulic pump, η_{Hydr}, and the electric motor system, η_{Elec}, leads to the required input power of the liquid cooling system

$$P_{Cool} = \frac{dp}{\eta_{Hydr} \cdot \eta_{Elec}} \cdot \frac{P_{th}}{c_P \cdot \rho \cdot \varDelta T} \cdot k_S \tag{3.99}$$

The assumptions to calculate the required liquid cooling input power are summarized in Table 3.15.

Table 3.15: Assumptions for the liquid cooling system

Design Parameter	**Value**
Hydraulic pump efficiency η_{Hydr}	85% [118]
Electric Motor-Controller efficiency η_{Elec}	95% [118]
Pressure loss dp	2 bar
Temperature difference $\varDelta T$	5°C
Safety factor k_{SF}	1.2
Specific power $\bar{\rho}$	1.2 kW/kg*

* projected to EIS year 2035 based on current specific power of 0.8 kW/kg [119] and maximum found projected specific power of 1.5 kW/kg assumed by [120]

In the first instance, the mass for the single liquid cooling system for each component is calculated with Equation (3.100)

$$m_{Cool} = \frac{P_{Cool}}{\bar{\rho}} \tag{3.100}$$

3.6.2 Cryocooling System

Beside the liquid cooling system, HTS components require a cooling system that keeps the components at cryogenic temperature level. There are two cryocooling systems available: passive and active systems. A passive cryocooling system uses a cooling fluid, for example liquid nitrogen, that is stored in a reservoir, to keep the components on a specific temperature level. The cooling fluid is hereby ejected to the environment after the cooling process. The advantage of this system is the simple design that requires a specific storage container for the cooling fluid and no additional equipment for pumps. The disadvantage is that the cooling fluid has to be refilled at the airport and causes an additional effort for ground operations. The second cryocooling system is represented by an active system. An electric motor-driven reverse Brayton cycle refrigerator, short *cryocooler*, is using liquid hydrogen as cooling fluid. Compared to the passive cryocooling system the active system represents a more complex architecture. This complexity of the system is also disadvantageous with regard to the overall system mass. Optimistic projections foresee a specific power of 0.33 kW/kg based on the maximum occurred cooling power [46]. The advantage is that this system does not influence the ground operations during turn-around.

In this study an active cryocooler system is considered that keeps mainly the electric motor system at a constant operating temperature of 40 K. This temperature level shows a good trade-off between the critical temperature and critical electric current density. For the estimation of the required ejected heat, P_{th}, Equation (3.101) based on [72] is used

$$P_{th} = P_{Comp} \cdot (1 - \eta_{Comp}) \cdot k_C \tag{3.101}$$

Depending on the component to be cooled, P_{Comp} represents the actual component power and η_{Comp} the efficiency of the component. The parameter k_C is used as a correction factor of how much of the ejected heat is actively cooled. A factor of 1 would mean that the entire generated heat is cooled by the cryocooling system. Heat flows beyond the system boundaries are not taken into account (e.g. conduction through mountings or the frame). The cryocooler power, P_{Cryo}, is finally calculated with Equation (3.102) according to [46].

$$P_{Cryo} = P_{th} \cdot \frac{T_{sink} - T_{load}}{T_{load} \cdot \eta_{Cryo}} \tag{3.102}$$

T_{sink} is the surrounding temperature (assumption at ISA +10°C conditions, no altitude dependency), T_{load} represents the operating temperature of the component and η_{Cryo}, is the cryocooler efficiency. The cryocooler efficiency is based on the Carnot efficiency and assumed to be 30% according to [46]. For the mass estimation of the system the maximum required cooling power during the mission is considered including the specific power of the cryocooler system (see Equation (3.100)).

4 Sizing Methods for Hybrid-Electric Power Architectures

The following section describes the definition of the parallel hybrid-electric topology and its system boundaries. Furthermore, the sizing approach of the entire parallel hybrid-electric architecture is described including the individual components assembled to subsystems such as the electric ducted fans with a gear box system and a conventional fuel supplied gas turbine. In the next step of the simulation framework the design of the electric architecture and the integration to the overall assessment platform including the aircraft level assessment are described. Finally, the assessment parameters are defined to identify an optimal architecture on system and aircraft level.

4.1 Parallel Hybrid-Electric Architecture

As outlined in Section 2.1 there are different variants of parallel hybrid-electric topologies. This variety of design options is given by the design space offered by the wide range of H_P and H_E. Furthermore, a big advantage of the parallel hybrid-electric topology is that the electric system does not have to be sized for the entire propulsive power like in cases of serial hybrid-electric or turbo-electric topologies. Table 4.1 compares different topologies and their suitability for aircraft application based on a qualitative assessment covering the knowledge gained out of Section 2 with the serial hybrid-electric (including the turbo-electric derivative) as a baseline. The comparison further includes the potential of enabling annexed technologies[1].

With respect to mass the serial hybrid-electric topology can be more advantageous than other hybrid-electric topologies even though the power train has to be sized for the entire propulsive power. The main reason for this advantage is that the electric system can be operated with a turbo-generator that has no battery assistance. In case of parallel hybrid-electric systems, the electric system always requires a power supply from the battery to be operable. This in turn has a negative impact on battery mass. Nevertheless, considering the power train efficiency improvement the parallel hybrid-electric variants could be more advantageous. This is mainly caused by the fact that the gas turbine efficiency is not negatively influenced by the

---

[1] Annexed technology refers to a supporting technology on overall aircraft level such as distributed propulsion or boundary layer ingestion, which the hybrid-electric topology efficiently affords

Table 4.1: Qualitative assessment of different hybrid-electric topologies for aircraft

Criterion	**Serial Hybrid Reference**	**MIPH**	**CIPH**	**DPH**
Mass	0	-	-	-
Efficiency	0	+	+	+
Reliability	0	0	0	+
Operational Behavior	0	-	-	0
Support Annexed Technologies	yes	no	no	yes
Electric Cruise Capability	yes	yes	no	yes

+...positive/better 0...neutral -...negative/worse

electric architecture efficiency chain. Although the gas turbine can be operated with higher efficiency in a serial hybrid system, the overall system has to over-compensate the electric architecture efficiency penalty on overall aircraft level. The reliability of the single system is assessed for the DPH more positive than for the other topologies, based on the core engine integration. Despite the DPH, the electric system of other topologies is integrated in series between the thrust producing device and the core engine. This series integration implies that the single components have to show a higher reliability (including the core engine) to reach the necessary failure rates again per flight hour of the overall power train. From an operational point of view, the serial hybrid-electric can be assessed slightly better than the DPH because of the decoupling of the electric propulsor and the gas turbine. The MIPH and the CIPH show more constraints due the strongly coupled integration of the electric system within the gas turbine. In this case, the operating margins of the turbo components have to be carefully monitored when choosing a certain electric power assist [43, 53]. The CIPH configuration is the only concept, where the electric system is not directly coupled to the propulsor shaft. This implies that with this kind of configuration no electric cruise is possible efficiently [43]. The turbo-electric topology and the DPH seem to be potential solutions to enable the support of annexed technologies such as boundary layer ingestion. Only the MIPH and the CIPH are pure engine hybridization concepts which not directly support annexed technologies on the overall aircraft level. Summing up all possible considerations the DPH seems to be a suitable solution for short to medium range aircraft and will serve as a baseline topology for the further studies.

Two main subsystems are required for the modeling of the DPH power train. The first is the battery supplied EDF. Figure 4.1 sketches the required components to supply and operate an electric powered ducted fan for a hybrid-electric propulsion system. It includes the ducted fan and a potential required gear box system to change the rotational speed levels and the electric system architecture including the battery as power supply. The second main subsystem is the GTF. The GTF consists of the well-known turbo-components and is supplied by kerosene. The detailed modeling approach and assessment of the entire DPH power train is described in the following for both the system and aircraft level analysis.

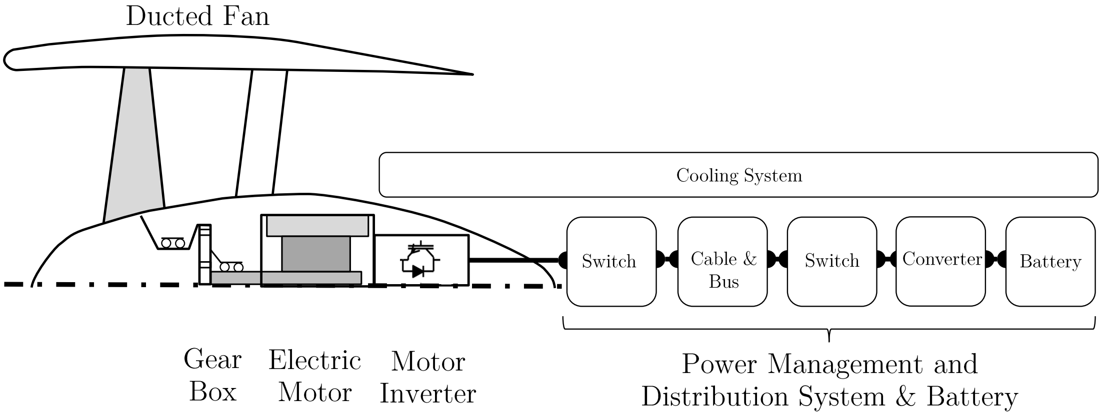

Figure 4.1: Required subsystems to power and operate an electric ducted fan. Based on [121]

4.1.1 Gas Turbine Design

The conventional power train is based on a GTF. For the modeling of the GTF the methods described in [19] are used for the performance and mass estimation. The sizing point is defined at Top of Climb (TOC) conditions for a design flight level of FL350, Mach number 0.78 and International Standard Atmosphere (ISA) +10°C conditions. The performance charts for different design thrusts have been generated with the commercial software GasTurb 11 [122]. The engine performance has been produced for a specific design thrust range between 15 kN and 35 kN. The GTF is designed for a bypass ratio of 16.2 and an overall pressure ratio of 62. As mentioned in Section 1.1, a gear box allows for the decoupling of the fan rotational speed and the low pressure shaft speed. In the current GTF design a gear ratio of 3 has been identified as optimal design parameter [21]. The performance data, such as the fuel flow, has been normalized to the corresponding design thrust to allow for specific scaling of the individual engine platforms in Figure 4.2 (d). The Thrust Specific Fuel Consumption (TSFC) varies between 13.24 g/kN/s and 13.30 g/kN/s depending on the GTF size in the design point. This approach is based on the method implemented in the aircraft preliminary design tool PaceLab APD [123]. The part load characteristics of the GTF model cover the relevant design envelope of altitude ranges between 0 ft and 35,000 ft and Mach number ranges between 0.2 Mach and 0.78 Mach. Further, the tables include the optimal thrust lever position for each relevant flight phase with minimum TSFC. For the relevant cruise segment, the optimum thrust lever position ranges between 0.7 and 0.9. The overall propulsive efficiency[2] of all gas turbine designs is 83.1% in the design point. Beside the performance of the gas turbine, the mass and geometry have also been defined. The results of the GTF design with regard to mass, geometry and performance characteristics for different design thrusts are summarized in Figure 4.2. The fan diameter varies between 1.6 m and 2.5 m depending on the design thrust.

---

[2] The overall propulsive efficiency in this thesis includes the propulsive efficiency, the fan polytropic efficiency, the intake, ducting and nozzle losses

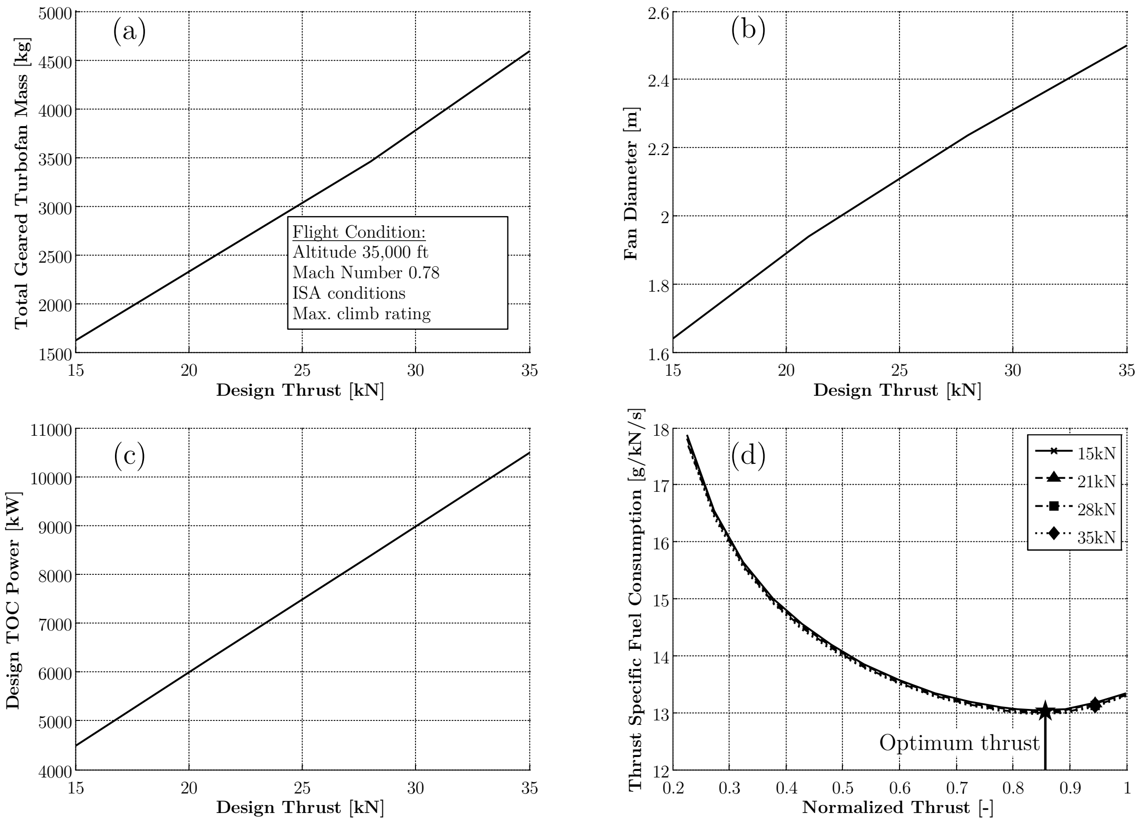

Figure 4.2: Design and off-design performance of the geared turbofan model. (a) Engine Mass (b) Fan Diameter (c) Fan Shaft Power (d) TSFC at part load conditions at FL350

4.1.2 Electric Ducted Fan Model

For an EDF powered by electrical means it is necessary to estimate the performance over the entire flight envelope to identify the maximum available thrust for each flight condition. Normally, a fan is powered by an air-breathing gas turbine whose performance depends on the flight altitude and speed. For the calculation of the maximum available thrust and the required fuel demand of such a configuration, there are several commercially available software tools, such as GasTurb [55]. In case of the EDF, the air breathing gas turbine is replaced by a flight state independent electric motor system. GasTurb does not offer the ability to directly simulate a ducted fan without a core engine. Therefore, for the generation of the performance of an EDF, a 0-dimensional thermodynamic performance model is used based on methods described in [124]. The definitions of the thermodynamic stations required for the 0-dimensional model are sketched in Figure 4.3.

This model covers basic gas-dynamic relationships and standard compressor theory of the important components inlet, fan, duct and nozzle calculated at single stations. These stations are characterized by the standard gas and flow properties such as total and static temperatures, densities, pressures, mass flow, Mach number and cross-sectional area. In the first

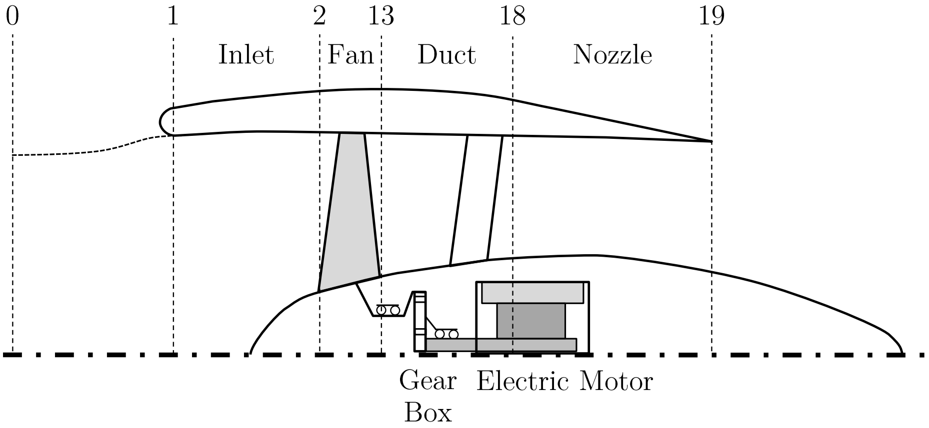

Figure 4.3: Schematic sketch of the electric ducted fan with gear box and electric motor integration based on [13]

instance, the fan is specified by the pressure ratio, Π, for a specific design thrust in a specified flight condition, usually TOC. In this design case, the flow path with the single required areas and Mach numbers are defined. Based on these parameters, the fan tip speed, v_{Tip}, can be calculated with Equation (4.1)

$$v_{Tip} = a \cdot \sqrt{Ma_{Rel,Blade}^2 - Ma_{Fan,Face}^2} \tag{4.1}$$

v_{Tip} is defined by the speed of sound, a, at the actual flight state, the relative blade Mach number, $Ma_{Rel,Blade}$, assumed to be 1.1 Mach and the design fan face Mach number, $Ma_{Fan,Face}$, assumed to be 0.6 Mach, according to [125] for such fan designs. With v_{Tip} and the required cross-sectional area of the fan (assuming a hub to tip ratio of 0.3) the design spool speed, $n_{Fan,Design}$, is calculated with Equation (4.2)

$$n_{Fan,Design} = \frac{v_{Tip}}{D_{Fan} \cdot \pi} \tag{4.2}$$

Based on these parameters, the fan power, P_{Fan}, can be calculated in the design and off-design conditions with Equation (4.3) with the specific heat, c_P, and the total temperature difference between the fan inlet, $T_{Tot,2}$, and exit station, $T_{Tot,13}$.

$$P_{Fan} = \dot{m}_2 \cdot c_P \cdot (T_{Tot,13} - T_{Tot,2}) \tag{4.3}$$

The off-design behavior of the fan is predicted using a generic fan map based on GasTurb [55], which is scaled to the actual fan design. The scaling approach of the fan maps as well as the off-design calculation is performed similarly according to GasTurb. The form of the map contains the non-dimensional parameters Π, the corrected mass flow, $\dot{m}_{corr}$, and the isentropic efficiency, which are normally represented by a function of relative corrected speed, N_{corr}, and the auxiliary coordinate, β. This non-physical parameter β is used to ensure that all points in the fan map are unambiguous. The performance simulation of the EDF was also validated against GasTurb. The parameter N_{corr} represents the thrust lever and is used to meet the thrust demand in off-design. The corresponding spool speed in off-design conditions is shown in Equation (4.4)

$$n_{Fan} = N_{Corr} \cdot \sqrt{\frac{T_{Tot}}{T_{Tot,Design}}} \cdot n_{Fan,Design} \tag{4.4}$$

The masses of the fan and the nacelle are calculated with the same methods as described in Section 4.1.1. Based on these described methods, the design of the EDF is performed at TOC conditions. For the identification of an optimal design the impact of the design thrust and the design Π has been investigated for different TOC sizing thrusts. The results of this approach are visualized in Figure 4.4.

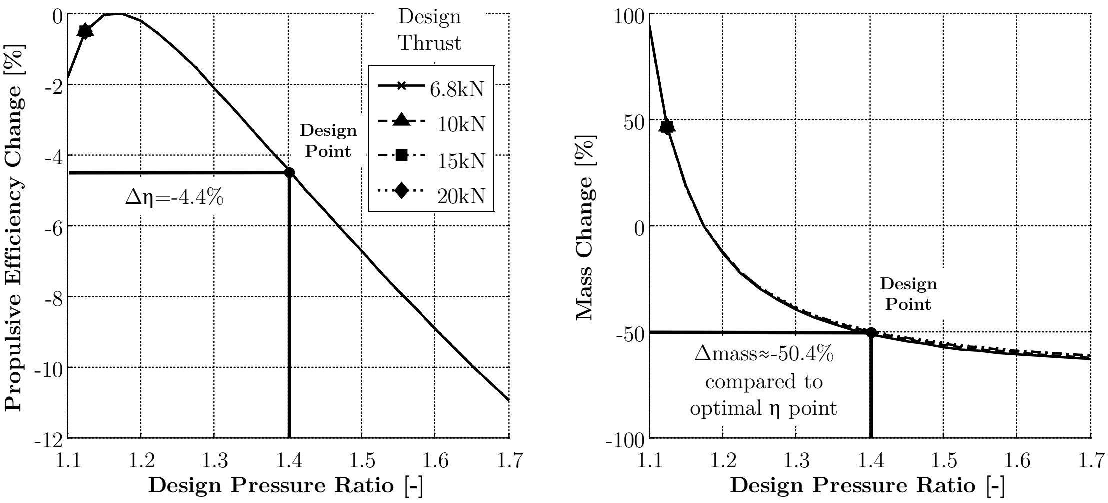

Design Settings:
- 35,000 ft, Mach 0.78, ISA +10°C
- Fan face Mach number 0.6
- Hub to tip ratio 0.3

Figure 4.4: Impact of different design fan pressure ratios on the propulsive efficiency and the EDF mass (fan and nacelle)

It should be recognized that with increasing Π the overall EDF mass decreases, while the propulsive efficiency has an optimum around 1.18 for the entire considered thrust range. Furthermore, the relative impact of the efficiency, as well as the mass, is nearly independent of the design thrust. For that reason, the design pressure ratio of all fan configurations has been fixed to 1.4, which represents a trade-off between mass and propulsive efficiency. The efficiency decreases 4.4% however the mass can still be reduced by 50.4% compared to the optimum propulsive efficiency design. A further increase of Π above 1.4 would only result in a minor saving of the EDF mass, while the efficiency strongly decreases.

4.1.3 Gear Box System

A gear box is required to change the rotational speed between the input and output. One design characteristic of the electric motor as shown in Section 3.2, implies that for a specific power demand a higher speed is more advantageous with regard to the motor mass. The rotational speed of the fan is defined by Π and fan diameter and is fixed for a required design thrust (Section 4.1.2). To allow for a decoupling of the fan speed and the motor speed a planetary gear box system was considered to optimize the electric motor with regard to the system mass. This gear box type offers a transformation of the rotational speed without changing the rotational axes of the system. The mass of the planetary gear box was estimated by an approach proposed by NASA [126], which is a function of the *Gear Ratio (GR)*, the maximum transmitted output torque, Q_{Fan}, and a technology factor, k, as shown in Equation (4.5)

$$m_{GB} = m_{Ref} \cdot k \cdot \left(\frac{GR}{GR_{Ref}}\right)^{0.15} \cdot \frac{Q}{Q_{Ref}} \tag{4.5}$$

The GR is defined in Equation (4.6) and is the ratio of the motor speed, n_{Mot}, and the fan speed, n_{Fan}

$$GR = \frac{n_{Mot}}{n_{Fan}} \tag{4.6}$$

The stage efficiency, η_{Stage}, can be assumed to be 99.5% [127]. For the off-design performance simulation the map published by [74] is used. This covers the dependency of the input torque and rotational speed. Stückl [18] published a regression equation with a normalized input power for a constant speed planetary gear box system that is commonly used for turboprop aircraft. This approach is only valid if the output rotational speed is fixed as it is the case for a propeller aircraft. However, a ducted fan has a variable rotational speed over the flight envelope. Therefore, the approach of Stückl cannot be used directly for a ducted fan because it only covers one operating line of a planetary gear box system. For that reason, to cover different rotational speed lines, the published efficiency map by [74] has been normalized to its design rotational speed and torque[3] (see Figure 4.5) and represents a double stage planetary gear box system. In the first instance, the off-design efficiency of the planetary gear box system was estimated with Equation (4.7)

$$\eta_{GB} = \eta_{Stage}^{n_{Stages}} \cdot f\left(\frac{n_{Mot}}{n_{Design,Mot}}, \frac{Q_{Mot}}{Q_{Design,Mot}}\right) \tag{4.7}$$

---

[3] Design torque is 120 Nm, design rotational speed is 3000 rpm and the gear ratio is fixed at 9.87 according to [74]

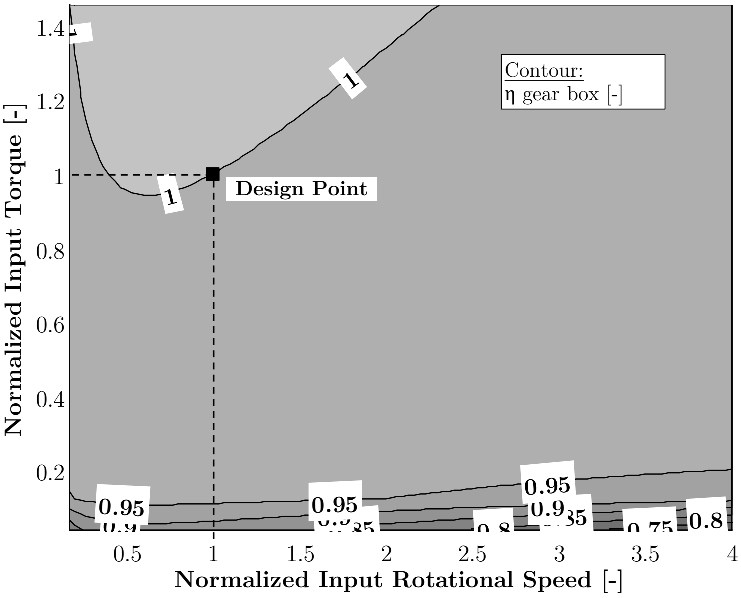

Figure 4.5: Normalized off-design map of a planetary gear box (scaled from two stages to one stage) based on [74]

$f(\frac{n}{n_{Design}}, \frac{Q}{Q_{Design}})$ represents the normalized efficiency at normalized rotational speed and torque based on the design point. Nevertheless, to compare the efficiency of the presented method in Equation (4.7) with the approach published by Stückl, the part load conditions were generated by reducing the output torque at constant speed starting from the design point. This comparison is visualized in Figure 4.6.

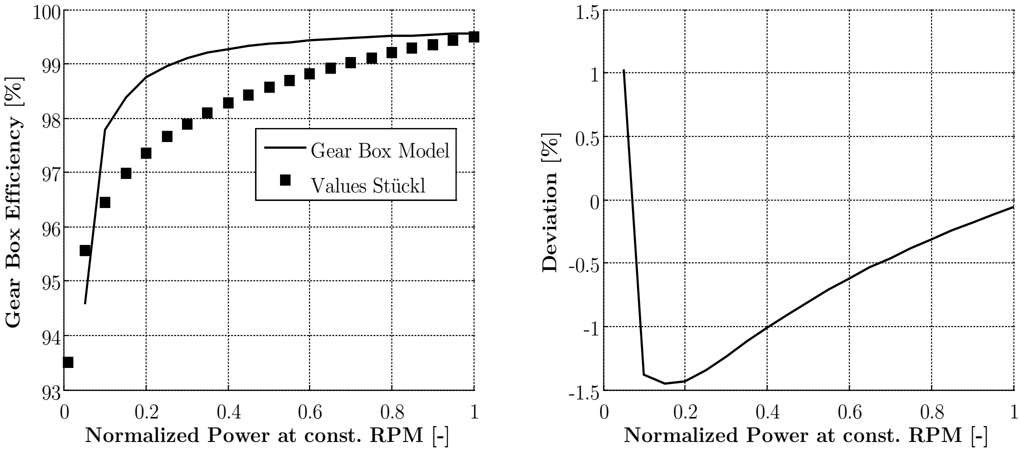

Figure 4.6: Comparison of the planetary gear box model (single stage) against the model of Stückl [18] at design rotational speed. Left: absolute efficiency at part load; Right: relative error between the models

The presented approach using the normalized performance map shows at lower part loads deviations of up to (relative) 1.5%. The deviation decreases to below 0.5% in part load areas higher than 40% of the design power. However, according to [127] the normalized approach delivers accurate results in the relevant operating area. Only at low part loads, the model used may be too conservative (see [127]). The normalized operating area for different speed and torque ratios based on the design values is shown in Figure 4.7.

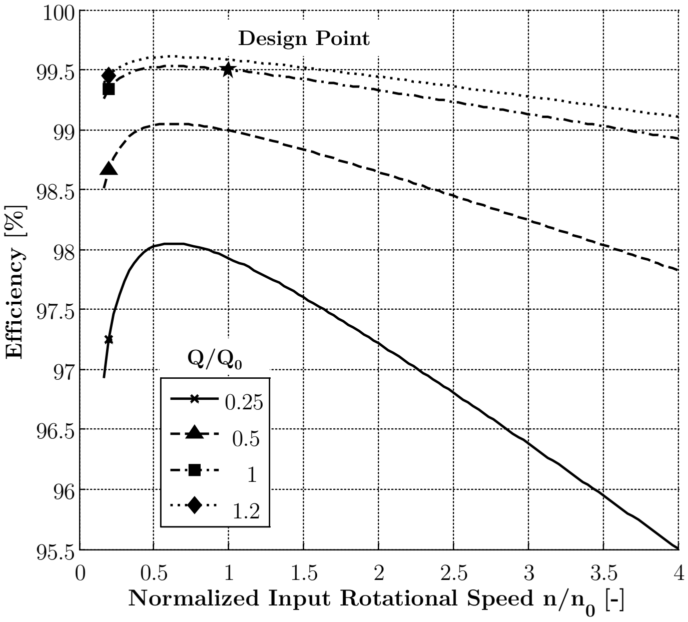

Figure 4.7: Gear box efficiency for different torque and speed ratios. Based on [121]

4.1.4 Electric Architecture Design

An electric architecture is responsible for the transmission of the electric power from the EPS to the power consumers in a redundant and reliable way. Therefore, an electric architecture is normally not designed for the normal operation case but for the abnormal operation scenarios. This also had an impact on the transmission performance and overall electric system mass. For the electric power supply only batteries were considered as they offer higher efficiencies than fuel cell systems (see Section 3.1). Batteries already provide DC and so the entire system is designed for a DC voltage transmission. This change in the transmission voltage type is also a trend, which can be recognized in electric architecture design for aircraft (Section 2). For that purpose the components described in Section 3 are assembled to fulfill the overall system architecture requirements. An example of a generic setup of n_{Mot} installed in electric motors supplied by n_{Bat} batteries per single power train is shown in Figure 4.8.

The system consists of several batteries where each battery is controlled via a BCU and protected by a SSPC. As several energy sources are involved in the EPS, the generated power is collected at a central distribution power bus. From this distribution bus, all loads are supplied such as electric motors, the thermal management system and possible electric subsystems. In normal operation each electric motor system is supplied by its dedicated distribution bus to be in compliance with CS 25.953 (see Section 2.3). The crosslink between

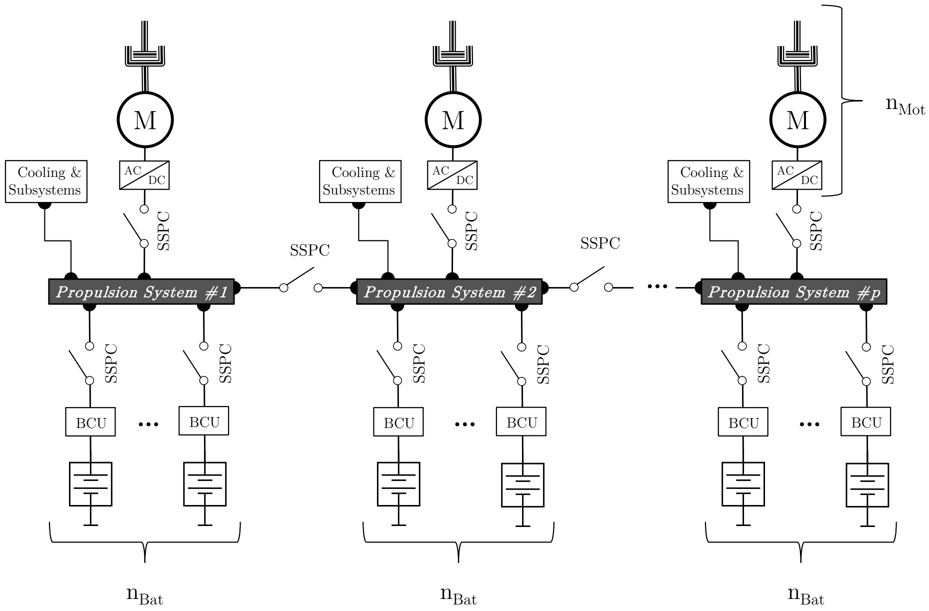

Figure 4.8: Generic design of an electric power architecture consisting of n_{Mot} electric motors and n_{Bat} batteries per single power train

the single busses, which is represented by another SSPC, allows for the connection of other systems in abnormal operation cases. Potential strategies of how the power sources and the power loads can be connected as a single power train are shown in Figure 4.9. As described in Section 3, all electric components have the similar input and output parameters voltage, frequency and power. Additionally, the output parameter heat is defined, which is required for the thermal management system sizing. The electric motor has as output only the power port representing the shaft power and a frequency port representing the rotational speed. Because only DC components are considered, the frequency port of each component is set to zero except for the output port of the inverter and the input port of the electric motor.

As described in Section 3.1, a battery shows a strongly non-linear discharge behavior, which responds in a fluctuating output voltage of the battery for different power demands. This voltage variation is stabilized in the first kind of architecture to ensure that the motor inverter-controller unit is always receiving a nearly constant input voltage and can operate at optimum efficiency. The stabilization of the battery voltage can be performed via buck, boost or buck-boost converters. In the second case (bottom) the battery voltage is not stabilized and the motor inverter-controller unit sees the entire voltage range of the battery. In both systems, a part of the battery power supplies the thermal management system, which is dependent on the efficiency chain of the connected components. The efficiency also depends on the requirements of power and voltage defined by the speed and torque at the electric motor shaft. The speed of the motor defines the output voltage and frequency of the motor inverter-controller unit. The entire sizing approach for the design and off-design performance is sketched in Figure 4.12.

The transmission or system voltage, U_{Elec}, is an important design parameter because it has an impact on the cabling mass, the transmission efficiency and the motor inverter-controller

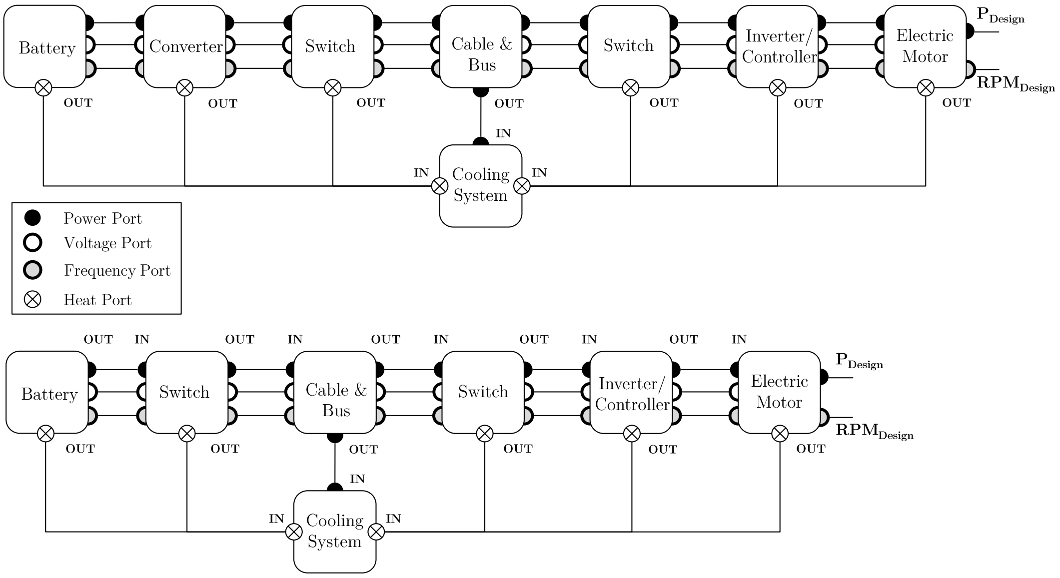

Figure 4.9: Different architecture options for constant (top) and variable transmission voltage (bottom). Adapted from [58]

unit. Depending on a variable or constant system voltage and of the converter type to be used, the definition of U_{Elec} is defined in Table 4.2. In design mode, U_{Elec} is defined at the battery output of the variable voltage architectures and at the converter output of the constant voltage architectures.

Table 4.2: Definition of the system voltages for different architecture types

Architecture Type	**Converter Type**	**System Voltage U_{Elec} Definition**
Variable Voltage	N/A	at $U_{Elec} = U_{Bat}$ at SOC 0%
Constant Voltage	Buck	at converter output ($U_{Elec} = U_{Bat}$ at SOC 0%)
	Boost	at converter output ($U_{Elec} = U_{Bat}$ at SOC 100%)
	Buck-Boost	at converter output ($U_{Elec} = U_{Bat}$ at SOC 50%)

As mentioned before an electric architecture is not sized for the normal mode of operation. For example the protection devices have to resist and switch fault currents, which occur in abnormal mode of operation. Figure 4.10 indicates for a dual motor architecture the normal mode of operation and two potential abnormal modes of operation with the OMI and the OBI case. The critical case for the crosslink switch occurs when the batteries on one side are inoperative. For that purpose one crosslink is sized for the entire electric motor power plus the losses and the required cooling power for this type of supply.

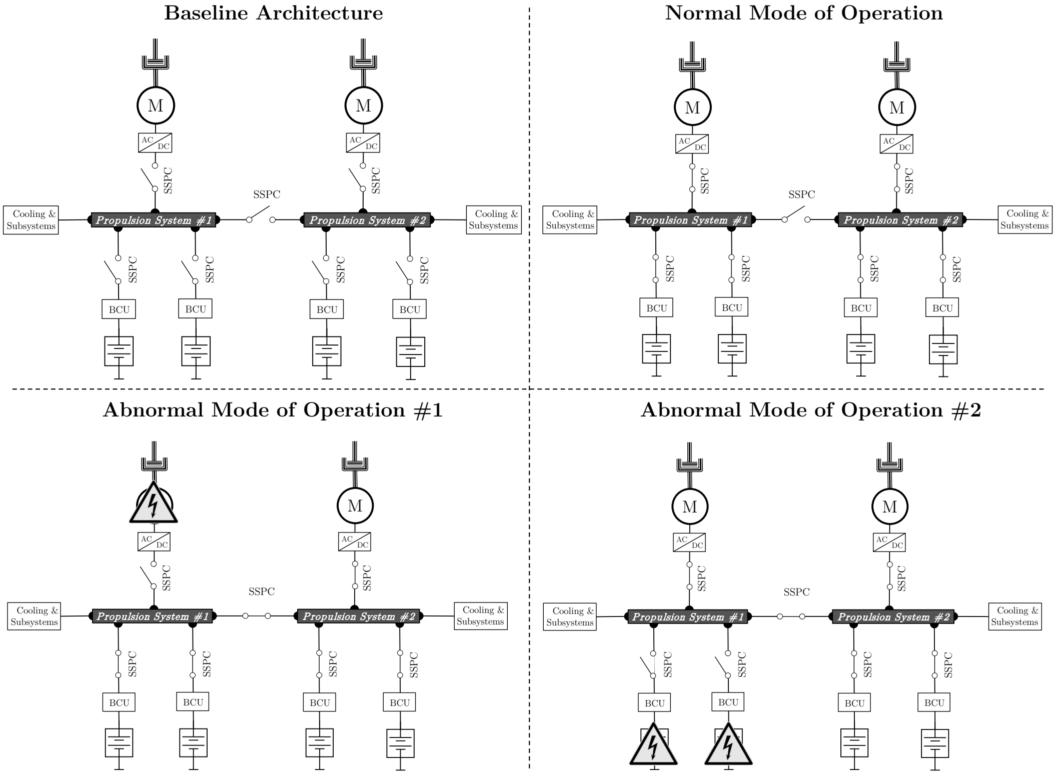

Figure 4.10: Electric architecture operation modes based on a dual motor architecture

4.2 Integration of Electric Power Train in Aircraft Sizing

The overall system sizing approach for the DPH power train concept is visualized in Figure 4.11. The starting point of the simulation is the definition of a design H_P, which is equal to a specific *Thrust Split (TSP)* between the conventional GTF and the EDF in a DPH topology in a specified flight state such as TOC or Take-Off (TO). The dependency between H_P and TSP is shown in Equation (4.8).

$$H_P = \frac{\frac{F_{EDF} \cdot v_0}{\eta_{prop,EDF}}}{\frac{F_{EDF} \cdot v_0}{\eta_{prop,EDF}} + \frac{F_{GTF} \cdot v_0}{\eta_{prop,GTF}}} = \frac{\frac{F_{Tot} \cdot TSP}{\eta_{prop,EDF}}}{\frac{F_{Tot} \cdot TSP}{\eta_{prop,EDF}} + \frac{F_{Tot} \cdot (1 - TSP)}{\eta_{prop,GTF}}} \tag{4.8}$$

$$\text{with } TSP = \frac{F_{EDF}}{F_{EDF} + F_{GTF}}$$

F_{EDF} represents the actual EDF thrust, F_{GTF} the actual GTF thrust, v_0 the flight speed, $\eta_{prop,EDF}$ the propulsive efficiency of the EDF and $\eta_{prop,GTF}$ the propulsive efficiency of the GTF. The TSP is defined as the ratio of the total thrust delivered by the EDFs to the total required thrust. If the propulsive efficiencies of the GTF and EDF are identical, the TSP is

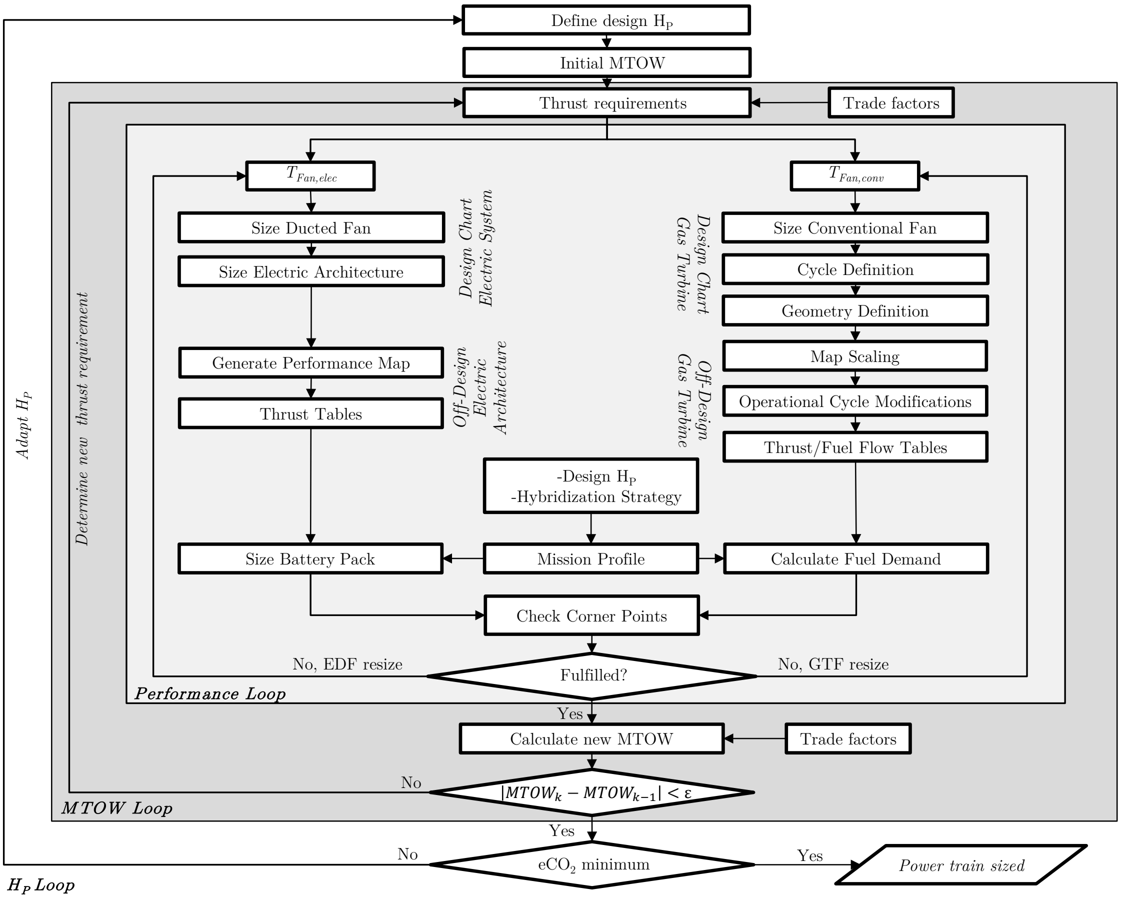

Figure 4.11: Sizing and integration approach of combined gas turbine and electric ducted fan on mission level

equal to the H_P. Otherwise to meet a specific value of H_P the parameter *TSP* has to be iterated until the target H_P has been reached. With the definition of the design H_P and an initial Maximum Take-Off Weight (MTOW) the thrust requirement based on trade factors is determined and split up according to the *TSP*. The fan geometry is defined by this thrust requirement of the EDF according to the methods described in Section 4.1.2. This results in the power and speed requirements of the electric system, which is sized for an optimum trade-off between overall system mass and efficiency according to the methods shown in the next section Section 4.2.1. In the off-design case of the electric architecture, the battery is dimensioned to meet the mission, as well as, sizing corner points such as OEI or OMI. In parallel, the conventional GTF is sized according to the methods described in Section 4.1.1. The aim of this approach is to get the optimum overall mass of the EDF system including the battery mass and the GTF, with the required fuel demand. The battery and fuel mass are estimated using a mission thrust profile for the specified aircraft and mission. This profile is discretized with specific time steps and in each point the required fuel and battery energy demand are calculated. The thrust profile and the trade factors for MTOW and thrust requirements are generated using the integrated aircraft sizing platform PaceLab APD [123], further explained in Section 4.2.2. The classical known trade factors consider a higher burned fuel during the mission for a non-hybrid aircraft and do not take into account for alternative power sources. For that reason, the mission performance has been determined separately. Due to the variation of the H_P, the ratio of the burned fuel mass to constant mass stored in batteries during the mission is not covered by these trade factors for conventional aircraft. The required fuel and battery mass are calculated with the mission profile and the actual hybridization strategy based on the design H_P. In total four different mission hybridization strategies are considered as described in detail in Section 5.2. Depending on the mission hybridization strategy the thrust requirement for the individual component is determined in each individual flight point. If a component is reaching its thrust limit, the TSP is adapted in a way that the remaining component is taking over the residual thrust. In this case it is checked if the total required thrust is delivered, otherwise the entire propulsion system has to be resized. Out of this performance process the resulting fuel and battery mass can be directly translated into an overall aircraft mass change. The delta mass of the DPH, Δm_{Prop}, is elaborated based on the reference propulsion system mass, m_{Ref}, represented at a $H_P = 0\%$ as shown in Equation (4.9).

$$\Delta m_{Prop} = m_{Ref} - (m_{GTF} + m_{Fuel} + m_{EDF} + m_{Elec} + m_{Bat}) \tag{4.9}$$

With this mass change a new MTOW can be determined with the help of the mentioned trade factors. In Section 4.2.2 the approach and definition of the trade factors are described in more detail. Afterwards the sizing loop is repeated with the newly determined MTOW and thrust requirements until the MTOW converges. The advantage of applying the trade factors in this way is that it allows for a fast analysis of the sensitivities of the electric system architecture design parameters with an implicit consideration of the snow ball effects at aircraft level.

4.2.1 Electric Architecture Design Framework

The models described in Section 3 have been integrated using Matlab [128]. Matlab was chosen for this kind of application, because it is a standard engineering platform and offers a broad spectrum of different optimization routines. The simulation set-up of the Matlab integration is sketched in Figure 4.12. This is used for the determination of the electric architecture mass and overall design and off-design performance.

The design requirements of the electric motor system like power demand and rotational speed is provided by the EDF model (see Section 4.1.2). In the **design case**, the single electric components are sized according to their maximum specified design parameter values. The sizing of the battery is mission-dependent and is not dimensioned during the architecture sizing. For the architecture sizing only the required battery output voltage range is considered. The iteration scheme is defined in a way that the required battery output power, $P_{Bat,Out}$, is determined via the electric motor shaft power demands, $P_{Mot,Req}$, corrected by the electric systems architecture efficiency including the cooling demand, $P_{Cool,Req}$, as visualized in

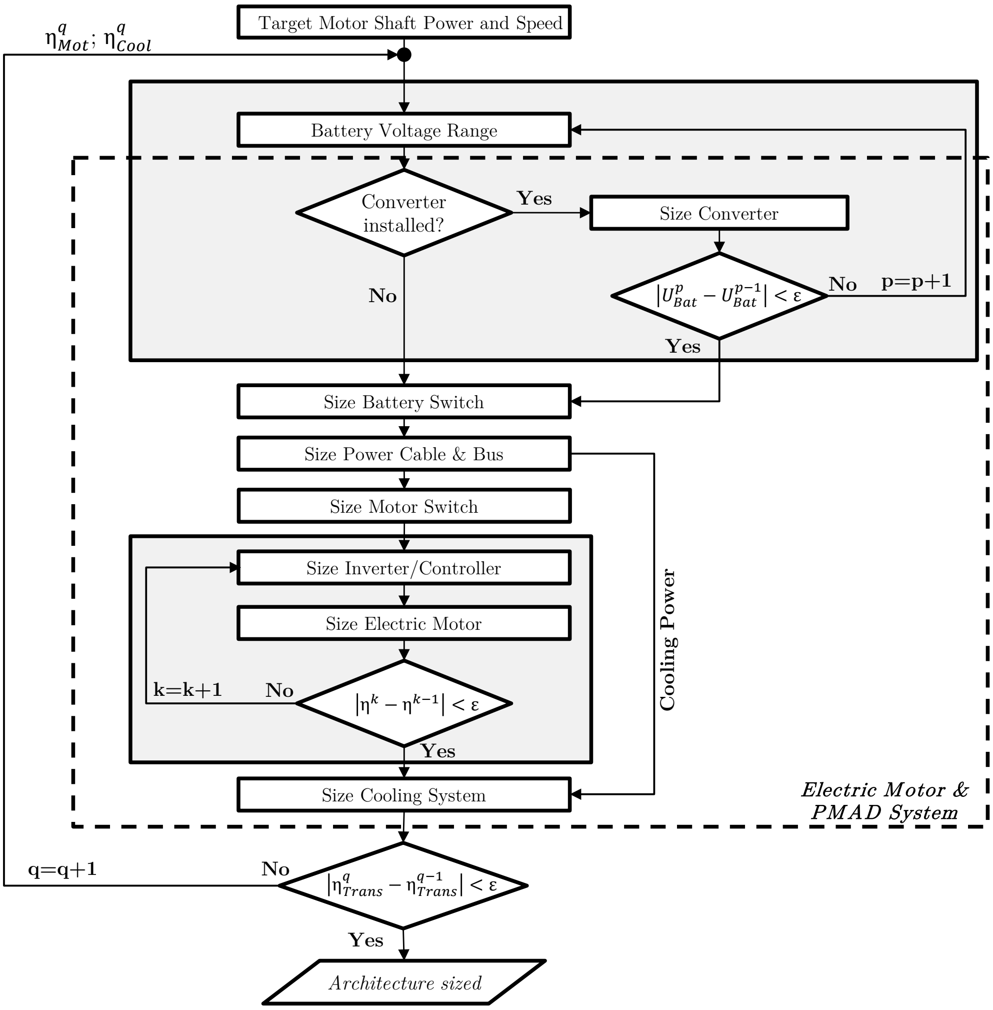

Figure 4.12: Simulation of the architecture performance depending on the sizing strategy for a specific power and speed demand of the electric motor

Figure 4.12. The electric system efficiency is split into a load and a supply side based on the distribution bus. The load side covers the efficiency from the bus to the electric motor, η_{Load}, the source side the efficiency chain from the battery to the distribution bus, η_{Supply}. The system converges if the deviation of the overall transmission efficiency, η_{Trans}, from the actual to the previous iteration step is below the set convergence criterion, ϵ, of 10^{-6}. This is necessary as the efficiencies of the single components are sensitive with regard to voltage and power. Furthermore, because the efficiencies of the single components are not known in the first iteration the required cooling power is also unknown. These losses have to be additionally compensated by the battery for a certain shaft power requirement. The iteration parameters listed in Equation (4.10) are used for this sizing approach of all considered architecture types. Beside the design mission profile, corner points are also considered as point performances for the overall architecture sizing. These corner points are defined at OMI and

OBI at low SOC at TO. If one of the power and speed requirements of these corner points are not fulfilled the architecture will be resized accordingly to meet the new requirements.

$$
\begin{aligned}
P_{Bat,Out} &= \frac{\frac{P_{Mot,Req}}{\eta_{Load}} + P_{Cool,Req}}{\eta_{Supply}} \\
\eta_{Load} &= \frac{P_{Mot,Req}}{P_{Bus,Out}} \text{ and } \eta_{Supply} = \frac{P_{Bus,In}}{P_{Bat,Out}} \\
\eta_{Trans} &= \frac{P_{Mot,Req}}{P_{Bat,Out}}
\end{aligned}
\tag{4.10}
$$

The **off-design performance** and also point performances use the same iteration loop as visualized in Figure 4.12 expect that the components are fixed with regard to mass and configuration (e.g. number of series and parallel connected switches). With this setup an off-design performance chart can be generated as a function of required motor power and speed, as well as, input voltage represented by the SOC of the battery. An example of a generic overall architecture off-design chart is shown in Figure 4.13. The configuration of the components are fixed and so the chart will show limitations such as electric current or torque limits for rotational speeds lower than the design speed or installed power limits for rotational speed higher than the design motor speed. However, other components can limit the overall electric performance beside the electric motor.

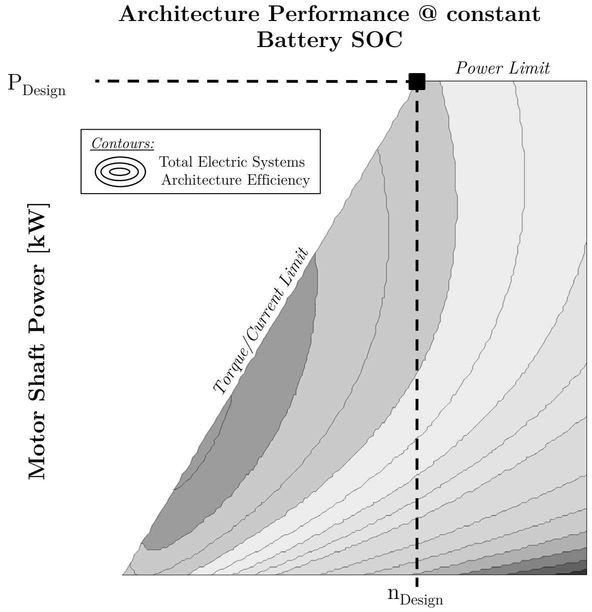

Figure 4.13: Generic example of an off-design chart of an electric architecture

4.2.2 Aircraft Sizing and Performance Environment

In aircraft design there are several performance simulation tools available. For investigations of the aircraft integrated performance and assessment, the commercial software environment PaceLab Suite [123] was used. The advantage of this software is that it combines a database with unit based aircraft parameters, with the corresponding methods such as mass, aerodynamics and geometry definition. These different disciplines can be implemented in different ways and level of detail with semi-empirical handbook methods or from external sources via look-up tables. It also includes a numerical flight performance simulation for a specified mission including field performance. Another advantage of this software is that there are not predefined input and output parameters. The mentioned methods are treated as black box systems by the framework which generates a linear system of equations to solve the aircraft performance and mission analysis. The number of inputs must be consistent with the number of outputs. With this design environment, trade factors are determined for a specified design range and payload via changing the operating empty weight increment mass, Δm, to identify the resulting impact on the MTOW and thrust (Figure 4.14). These masses include the entire propulsion characteristics and can be translated with the help of the trade factors in an initial estimation of the overall aircraft performance. The resulting mission thrust profile is also extracted out of this process. The thrust profile is required to determine the required fuel and battery mass for a hybrid-electric aircraft for a specific H_P.

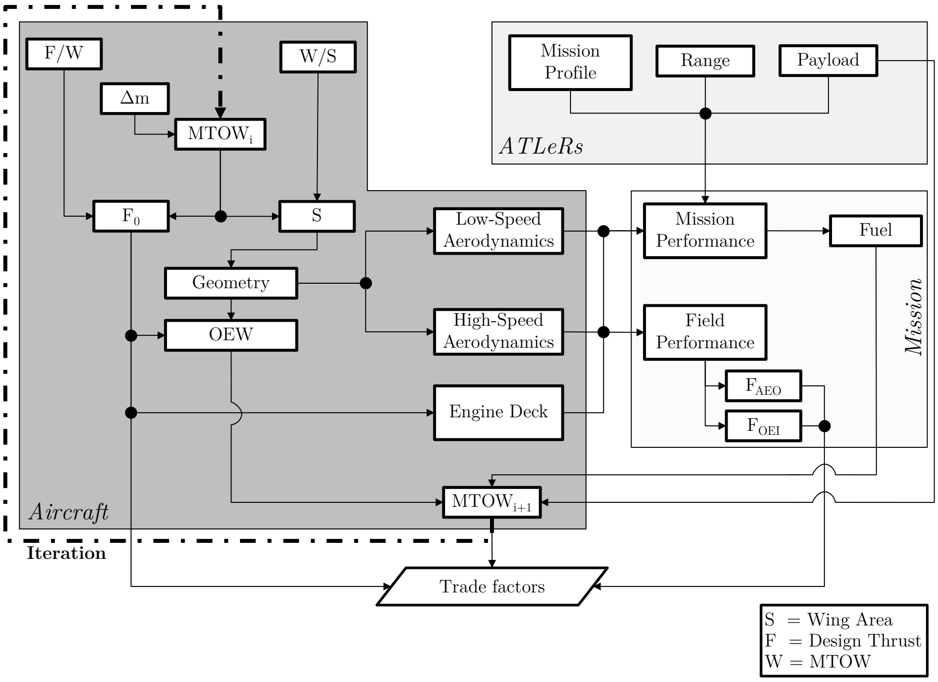

Figure 4.14: Sizing loop implemented in PaceLab APD to determine the trade factors for the given reference aircraft. Based on [129]

For the mass estimation of the single components such as airframe, wing, empennage, and landing gear the methods according to Torenbeek [14], Raymer [16] and *Luftfahrttechnisches Handbuch* [130] are used and calibrated to meet the performance requirements as summarized by [129]. For the aerodynamics (low and high speed performance) the methods according to Torenbeek are implemented [129]. The propulsion system is modeled to cover the masses, geometries and performances, like fuel flow and maximum available thrust in the single flight phases of the commercial software GasTurb [55]. These performance data are implemented via look-up tables in the framework and are used for the determination of the reference propulsion system mass and fuel demand.

4.3 Assessment Parameters for Hybrid-Electric Power Trains

One main environmental goal of this research was to reduce the overall CO_2 per passenger kilometer, which should be reached by an increase in the propulsion efficiency. There are already several assessment parameters for propulsion system and overall aircraft level evaluation available in current literature. Seitz et al. [13] introduced the *Thrust Specific Power Consumption (TSPC)* on a system level, which is an extension of the well-known TSFC. The *TSPC* is used to determine the overall system efficiency defined as supplied power, P_{Supply}, in form of battery power, P_{Bat}, and effective fuel enthalpy power, P_{Fuel}, to the net design thrust, F_N, as shown in Equation (4.11)

$$TSPC = \frac{P_{Supply}}{F_N} = \frac{P_{Bat} + P_{Fuel}}{F_N} \tag{4.11}$$

The second parameter used for the assessment is the CO_2 equivalent. This allows for an assessment on overall aircraft level to identify the best degree of power and energy hybridization. To identify the potential CO_2 equivalent of a hybrid-electric power train, assumptions for the electric energy mix have to be made and forecasted to the targeted EIS 2035+. Such a study was already performed by [131] for different scenarios of electric energy production mixes. These scenarios are summarized in Table 4.3 for the different electricity mixes and GHG emissions covering minimum, nominal and maximum scenarios. The maximum scenario represents the worst case scenario where the energy markets are developing based on today's policies (e.g. share of coal based generation around 40%) [131]. The nominal scenario includes the today's current policies plus the materialization of planned electricity mix enhancements such as a further increase in renewable energy. The minimum scenario represents a development of the energy generation in a way that the climate goal of the generated GHGs is reached. In this scenario in 2040 a global average temperature rise to a maximum of 2°C would be achieved using increased sources of renewable energy [131].

For the hybrid-electric power train the generated CO_2 equivalent can be estimated with Equation (4.12). This equation includes the generated CO_2 for the production of the fuel and the electric energy according to Table 4.3. These values of the electric energy mix do not included the additional CO_2 generated during the production of the battery packs. Kerosene production accounts for 87.3 gCO_2eq/MJ (equal to 3.73 kg_{CO_2}/kg_{Fuel}) including

Table 4.3: Projection of possible electricity mix GHG emissions for year 2035+ taken from [131]

	min. Scenario	**nom. Scenario**	**max. Scenario**
Equivalent CO_2 footprint $[gCO_2/kWh]$ $1/\bar{\rho}_{CO2,Elec}$	237	385	462

the combustion of the kerosene (well-to-wake). Finally, the overall emitted equivalent CO_2 for a hybrid-electric mission is calculated by Equation (4.12).

$$eCO_2 = E_{Fuel} \cdot \frac{1}{\bar{\rho}_{CO2,Fuel}} + E_{Bat} \cdot \frac{1}{\bar{\rho}_{CO2,Elec}} \tag{4.12}$$

5 Application to Hybrid-Electric Power Trains

The following section describes the application of the developed methods for the investigation of the parallel hybrid-electric power train on system (uninstalled) and aircraft (installed) level. The aircraft level assessment is performed using trade factors based on a reference aircraft and a corresponding thrust profile over the mission to determine the H_P dependent fuel and battery masses. The investigations on the system level cover the results of the electric power architecture sizing, the ducted fan design and the system level considerations of the DPH power train. The electric power architecture analysis is conducted for a broad range of shaft power and rotational speed demands of the electric motor to identify the optimal parameters and technologies for different performance demands. Based on those results, the most suitable options to link the electric system with the EDF are identified. A further uninstalled study investigates the impact on the system mass and efficiency for different values of H_P when combining the EDF system with the gas turbine. Finally, after the identification of constraining combinations a similar study was performed for the different values of H_P on aircraft level (installed). With the help of the trade factors, the performance of the hybrid-electric aircraft is investigated with the thrust profile of the reference aircraft, and mission. The performance analysis includes the determination of the power train efficiency, the required battery and fuel mass. The assessment was performed using the equivalent CO_2 generation per passenger nautical mile as main FoM.

5.1 Reference Aircraft and Mission

The datum aircraft was based on an advanced kerosene powered short-to-medium range narrow-body aircraft in the class of an A320 sketched in Figure 5.1 (left). The EIS year of the reference aircraft was defined for 2035 (technology freeze 2030) [21]. It accommodates a design payload of 18360 kg (180 PAX) and a design range of 1300 nm. The design range of this concept has been identified with 1300 nm and was selected as benchmark range because it covers nearly 90% of the cumulative stage lengths in the class of narrow-body aircraft [21]. Furthermore, this design range was also the result of a comprehensive analysis of different design ranges for the parallel hybrid-electric derivatives, referred to as BHL Quad-Fan shown in Figure 5.1 (right), which offers the best block fuel reduction potential and Energy Specific Air Range (ESAR) change for this concept. The BHL Quad-Fan represents a DPH aircraft with two inner mounted kerosene supplied GTFs, as described in Section 4.1.1, and two battery supplied EDFs mounted at the wing outboard sides. Both propulsion systems can be independently controlled from each other. In the reference study [21], the electric system uses HTS cables and full HTS motors. The batteries are housed in containers within the fuselage allowing for a quick exchange of these batteries at the airport [21]. Furthermore, the datum non-hybrid-electric aircraft (see Figure 5.1 left) covers an all-electric subsystem architecture (e.g. environmental control system, anti-ice, actuation, etc.) powered by a fuel cell system according to [19]. For sake of comparison, this fuel cell system for the subsystems is also considered for the hybrid-electric variants that are derived in this thesis with the help of the selected reference aircraft and is covered by the trade factors. This means that no additional customer power off-takes from the power train system are required.

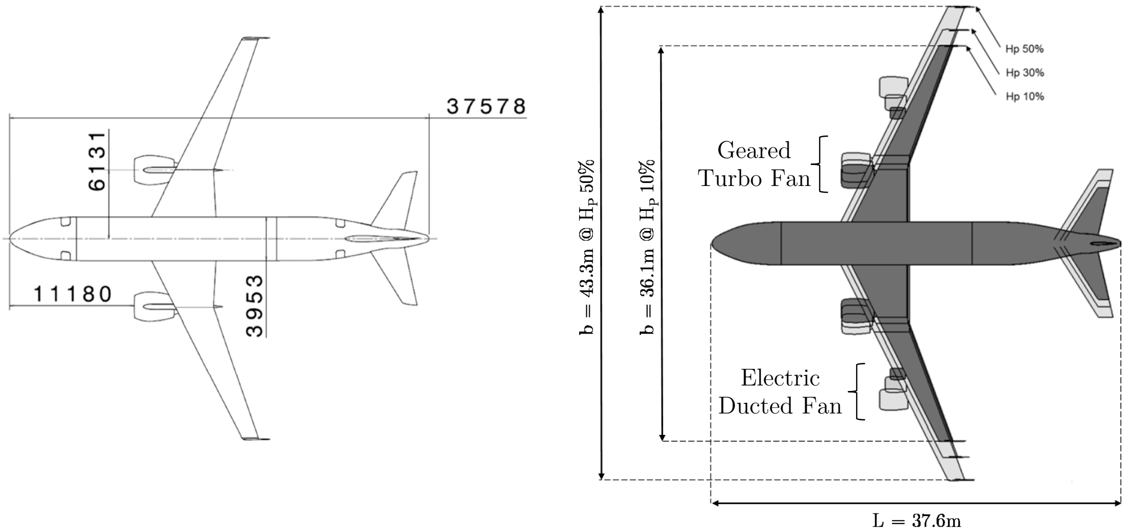

Figure 5.1: Top view of the advanced 2035+ reference aircraft (left) and the hybrid-electric BHL Quad-Fan (right) according to [21]

The reference mission was based on Pornet and Isikveren [21] defined for 1300 nm and 180 passengers. For the determination of the required fuel and battery demand, the mission performance calculation used a normalized thrust profile over the mission, that was normalized with the reference TOC thrust, $F_{TOC,Ref}$ (Figure 5.2). It includes the block mission (gate to gate) as well as the required reserves, such as a 30 min hold and a 100 nm diversion segment.

To determine the new design thrust requirements, F_{TOC}, for the hybrid-electric aircraft covering different design values of H_P, the aforementioned $F_{TOC,Ref}$ is implicitly scaled with the corresponding MTOW assuming a constant thrust to weight ratio as shown in Equation (5.1). For that purpose, the trade factors are used and are dependent on the mass change of the

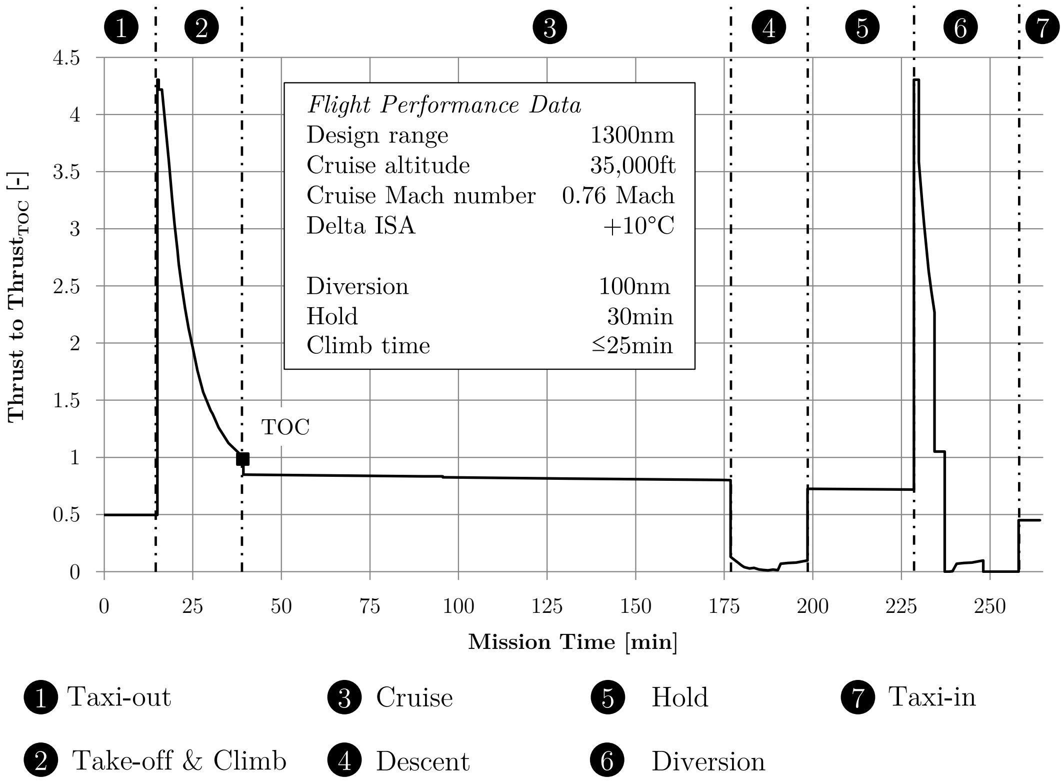

Figure 5.2: Normalized thrust profile of the DPH aircraft reverse engineered according to data published by [21]

propulsion system including the battery and fuel mass, Δm_{Prop}, defined in Section 4.2. This mass change influences the overall operating empty weight and in turn the MTOW and the absolute thrust requirements. Based on the methods developed by Pornet et al. [19, 21] these thrust requirements also cover aspects for TO during All Engines Operative (AEO) and OEI conditions.

$$\begin{aligned} F_{TOC} &= F_{TOC,Ref} \cdot \left(1.0 + 2.12 \cdot 10^{-5} \cdot \Delta m_{Prop}\right) \\ F_{AEO} &= 3.96 \cdot F_{TOC} \\ F_{OEI} &= 2.34 \cdot F_{TOC} \end{aligned} \tag{5.1}$$

The estimation of the new MTOW can be calculated with the trade factor using also Δm_{Prop} as defined in Equation (5.2).

$$MTOW = MTOW_{Ref} \cdot \left(1.0 + \Delta m_{Prop} \cdot 2.495 \cdot 10^{-5}\right) \tag{5.2}$$

With the MTOW and the scaled TOC thrust of Equation (5.1), the actual mission point thrust requirement, F_{actual}, can be calculated using Equation (5.3). This thrust demand includes a calibration factor, $Corr_{Aero}$, allowing for the consideration of potential aerodynamic improvements enabled by hybrid-electric propulsion systems such as boundary layer ingestion. This calibration factor was set to 1 for the main scope of the presented studies.

$$F_{actual} = F_{norm} \cdot \frac{F_{TOC}}{F_{TOC,Ref}} \cdot Corr_{Aero} \tag{5.3}$$

The aircraft reference data used for the aircraft sizing approach are summarized in Table 5.1. Pornet and Isikveren [21] have identified an upper limit of the H_P at 30% for the investigated DPH configuration due to a volumetric constraint caused by the battery housing. For the sake of comparison, this H_P was used as benchmark for the system level studies.

Table 5.1: Summary of the most important parameters for the reference aircraft and the BHL Quad-Fan at a H_P of 30% taken from [21]

Parameter	**Reference 2035**	**BHL Quad-Fan Hybrid-Electric H_P=30%**
Total Propulsion Mass	10449 kg	24011 kg
-Thrust Device Masses (equipped GTFs and EDFs)	4132 kg	5117 kg
-PMAD Mass (without motor and controller)	n/a	1348 kg
-Release Fuel Mass	6317 kg	5806 kg
-Total Battery Mass	n/a	11740 kg
$MTOW_{Ref}$	60840 kg	77730 kg
$Thrust_{TOC,Ref}$	35.9 kN	46.0 kN
$Thrust_{AEO,Ref}$	142.2 kN	182.0 kN
$Thrust_{OEI,Ref}$	84.0 kN	107.6 kN
Single Reference EDF Thrust (sizing at TOC)	n/a	6.8 kN

5.2 Description of Investigated Studies

In total four, mutually constructive studies were conducted within this thesis covering system level investigations, such as optimal electric architecture performances, and aircraft level assessments. These dependent studies are summarized in Figure 5.3.

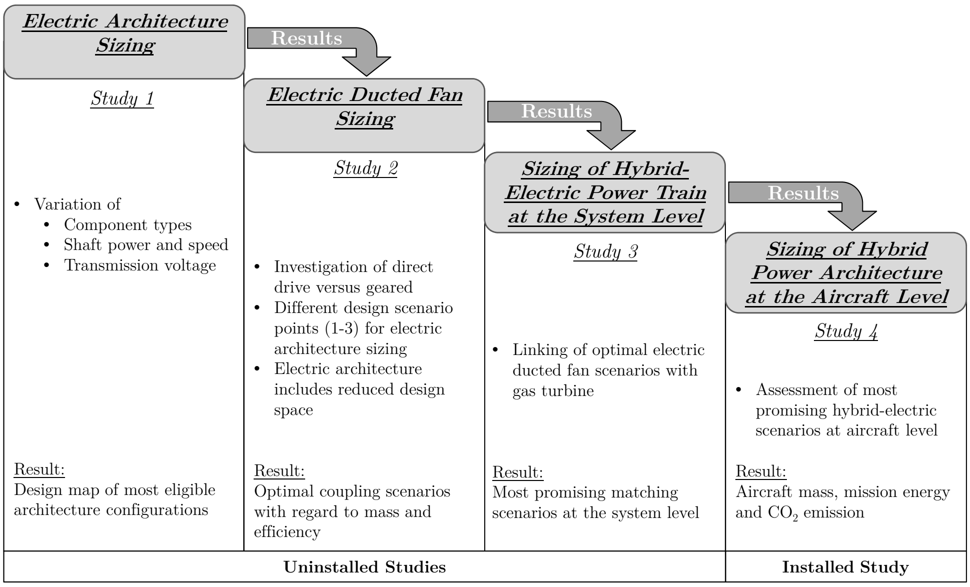

Figure 5.3: Approach of the conducted system and aircraft level sizing studies symbolizing the relative level of detail of each single study by the height of the bar

The **first study** covers the determination of the optimal architecture components and voltage levels for a specified design shaft power and the rotational speed requirements. As a baseline, a dual motor architecture was used. The performance assessment of the different architecture combinations was performed using the assessment parameter defined in Section 4.3 plus the specific power at the system level. The different options and possible component combinations for the battery supplied electric power architecture are shown in Table 5.2 in the form of a morphological box.

Table 5.2: Overview of electric power architecture system design options

Component	**Design Space**			
	Option 1	**Option 2**	**Option 3**	**Option 4**
Motor Type	Conventional	Partial HTS	Full HTS	
Converter Type	None	Buck	Boost	Buck-Boost
Cable Type	Copper	Aluminum	HTS	

In the defined design space 36 architecture options were investigated for the different technology options for electric motor, converter and cable type. These architectures are sized for a power range varying between 0.5 MW and 24 MW (representing the OEI case of the Ce-Liner concept [35]) for a rotational speed range between 2000 rpm and 10000 rpm and transmission voltages between 1500 V and 5000 V. Based on the top view of the reference aircraft shown in Figure 5.1, a cable length of 42 m was determined for all electric architecture studies which connect the battery with the motor-inverter unit. The aim of this study is to identify the best voltage level, with regard to the overall system efficiency and mass, using the considered components.

The **second study** covers the coupling of the EDF with the most eligible electric system architecture identified in the first study. This includes the comparison between a direct drive versus a geared variant as shown in Figure 5.4, which impacts the sizing point of the electric systems architecture. The main purpose of this consideration is to identify the most suitable gear ratio with regard to overall mass and efficiency on the EDF system level. As shown in Section 3.2 the mass of an electric motor can be reduced when increasing the rotational speed. However, higher rotational speeds can cause higher (switching) losses on the controller side since the controller has to be operated with a higher switching frequency to generate the necessary output frequency. Furthermore, different sizing powers and speeds of an electric motor within the Q-n envelope have to be considered. Figure 5.5 shows different motor sizing scenarios for the electric motor, when linking it to the ducted fan map for a fixed design thrust. This example shows a generic Q-n fan map for all possible flight states and thrust lever positions. In motor sizing scenario **(1)**, the motor power represents the power demand that is normally required for TO. Considering a sizing scenario for the quad-fan configuration the motor sizing option **(2)** covers the TOC conditions for speed and torque. This option implies that the EDF is not delivering its maximum available TO thrust. This means that in the case of the DPH quad-fan configuration the gas turbine has to be sized to deliver the required delta thrust during TO. Sizing scenario **(3)** is also sized for TOC power demand, but at TO conditions for torque and speed at the equivalent TOC power. For the considered sizing scenarios, the impact on the overall thrust performance was investigated within the flight envelope. This also includes the aspects of the maximum available thrust at different flight altitudes and Mach numbers and which is the constraining component parameter.

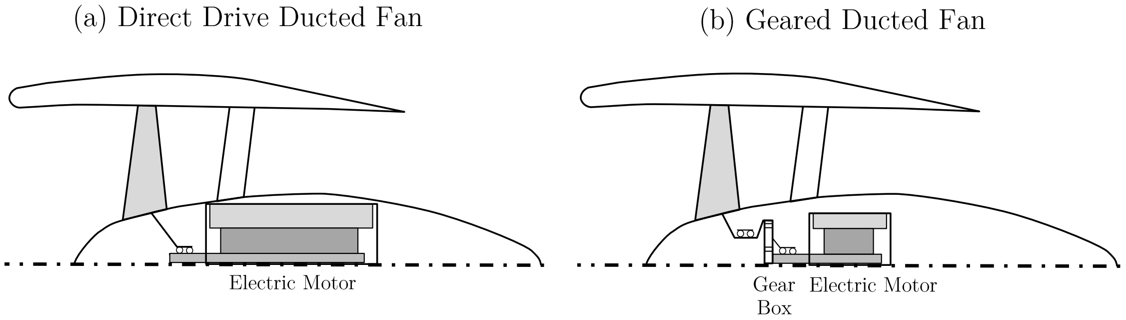

Figure 5.4: Design option of a (a) direct drive and a (b) geared electric ducted fan concept

In the **third study**, the results of the EDF and the electric system architecture are combined with the gas turbine characteristics to represent the DPH power train architecture. In the first instance, different impacts of the design H_P are investigated assuming constant thrust requirements for TOC and TO based on the reference hybrid-electric aircraft platform. The nominal operation mode AEO and the abnormal modes of operation, such as OEI and OMI, are considered for the determination of the required sizing thrust. A main focus is set on the sizing point of the gas turbine and the EDF and which thrust requirement is the driving parameter. The design strategy was performed in a way that the thrust requirement of the EDF is identified in TOC conditions for a defined H_P. If a thrust requirement is not fulfilled for TO, the gas turbine will be (over-)sized in TOC accordingly to meet those requirements. This oversizing impacts the resulting H_P in TOC. The sizing strategy to meet again the defined design H_P and TOC thrust was defined in a way that the GTFs are operated in part load conditions. Using this design strategy the used mission thrust profile is similar for the different design values of H_P. Another possibility to increase the TO thrust would be to change the turbine exit temperature, T_4. This cycle adaption was not considered as it would decrease the life of the gas turbine. The overall mass and TSPC were used for the assessment as main FoM at the system level.

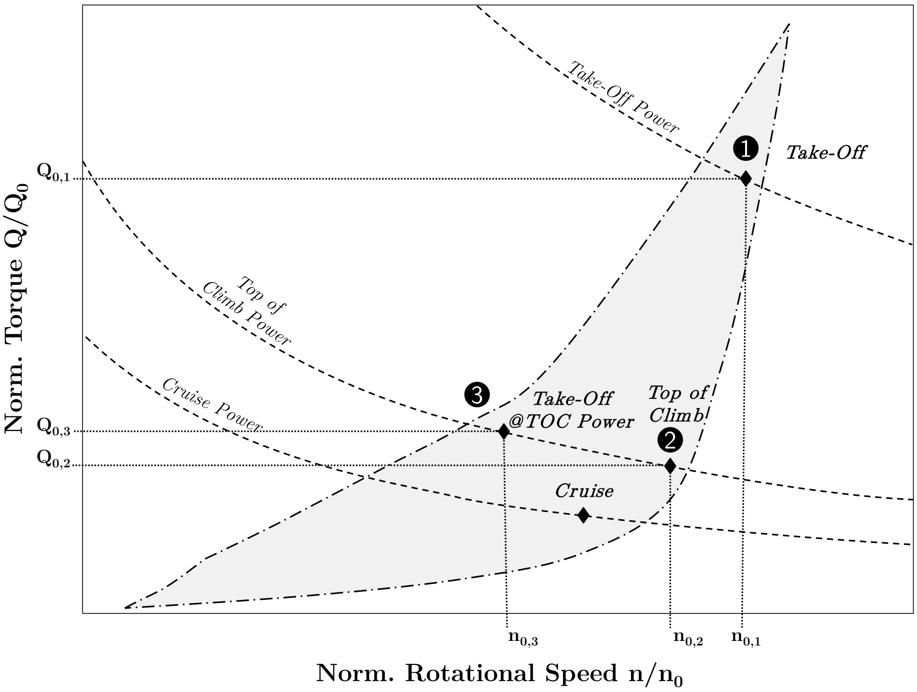

Figure 5.5: Different sizing scenarios of the electric motor matching with the electric ducted fan characteristic. (1) take-off power sizing (2) top-of-climb power sizing (3) take-off conditions sizing at equivalent top-of-climb power

Finally, the **fourth study** analyzed the different sizing points on the overall aircraft level using a generic mission thrust profile that was scaled with the actual MTOW. This thrust profile served as a baseline to determine the required battery mass, fuel demand, and the mass of the overall hybrid mission architecture. The assessment parameter of the equivalent CO_2 was used for the identification of the optimum design H_P (Section 4.3). Additionally for the best hybrid power train design point, different hybridization strategies were analyzed for the considered design mission. In total four different hybridization strategies (see also Figure 5.6) were analyzed:

1. The GTFs deliver the maximum possible thrust in all flight phases and the EDFs provide the residual thrust, strategy GTF_{max}
2. The EDFs deliver the maximum thrust in all flight phases and the GTFs provide the residual thrust, strategy EDF_{max}
3. A constant H_P is used for the entire mission, where it is possible (strategy *constant* H_P)
4. The GTFs are operating in the optimal SFC point and the EDFs are providing the residual thrust, strategy *optimum* SFC_{GTF}

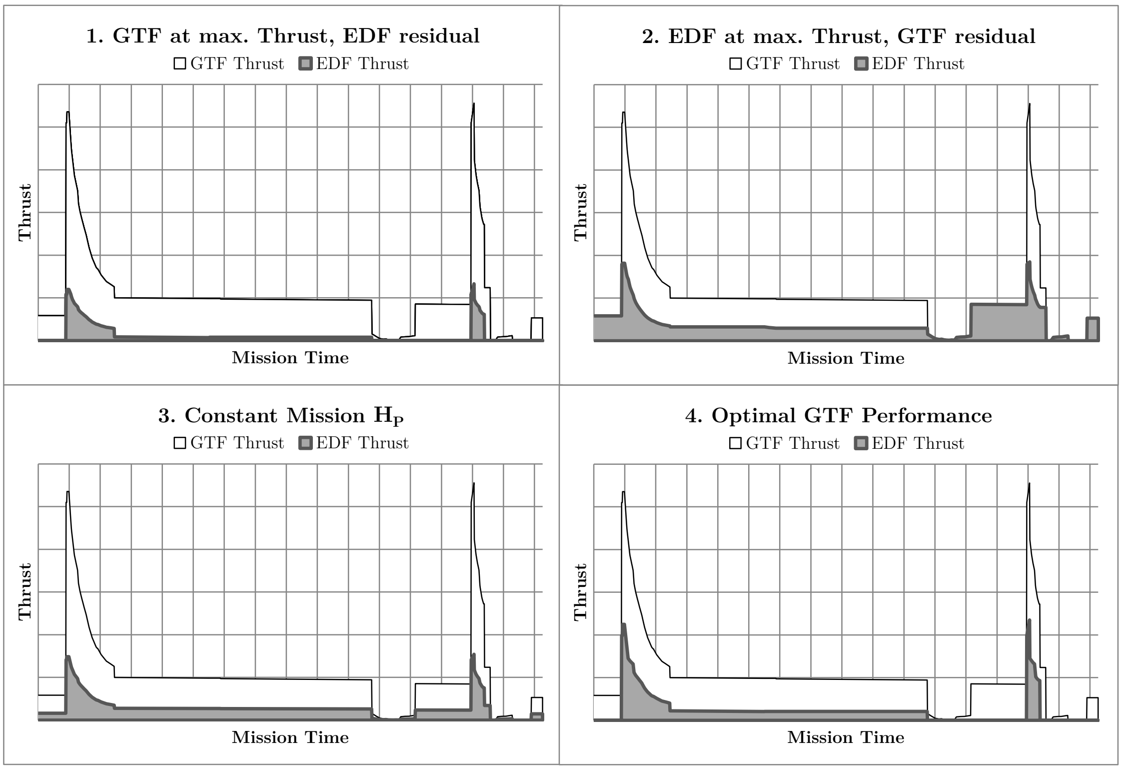

Figure 5.6: Possible hybridization strategies for a hybrid-electric propulsion system sized in TOC conditions

5.3 Results

The following section covers the results of the previously described studies. At first, the uninstalled outcomes are presented starting with the electric system architecture results. Finally, the impact of different values of design H_P and mission hybridization strategies are shown at system and aircraft level.

5.3.1 Electric Architecture Results

The assessment of the electric architecture sizing, as described in Section 5.2, is based on a dual motor configuration shown in Figure 4.8. For this baseline configuration, different architecture options were simulated for different component technologies, design motor shaft powers, speeds and design transmission voltages. The main results of this approach are shown in Figure 5.7 for the overall system efficiency and specific power excluding the battery.

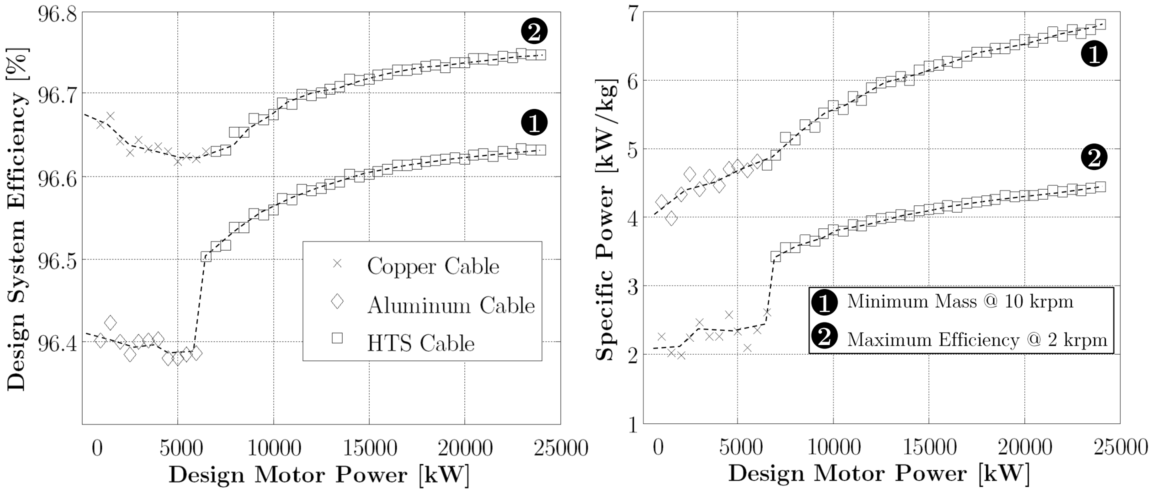

Simulation Settings:
Dual motor architecture with variable voltage transmission, full HTS motor and different conductor materials

Figure 5.7: Variable voltage system at a transmission design voltage level of 2000 V for all architectures utilizing a full HTS motor at different rotational shaft speeds and cable options for minimum system mass (1) or maximum transmission efficiency (2)

It covers the two extreme possible design options for an electric architecture, either an architecture designed for minimum mass (1) or maximum efficiency (2). One major aspect that could be identified was that the variable voltage system (no converter installed) dominates the architecture design with regard to minimum mass and maximum efficiency for all power and rotational speed ranges. The full HTS motor design (stator and rotor utilized with HTS material) provided the best performance for all considered design combinations including the required cooling demand. The transmission voltage is constant at 2000 V below 7000 kW and 1500 V above 7000 kW. Only the design choices of a specific system rotational speed and transmission cable type were impacting the targeted system goal. If the electric system should be designed for high efficiency the copper conductor is providing the best results below single electric motor powers of 7000 kW at rotational speeds of 2000 rpm. Above 7000 kW, the HTS transmission cable including the required additional cryogenic cooling demand seems to be a suitable solution. Maximum efficiencies of 96.75% can be achieved (without battery). Considering the system mass, the high efficiency system offers specific powers of 2.8 kW/kg below 7000 kW and up to 4.3 kW/kg using HTS transmission cables. In contrast to the high efficiency system, the second extrema represents the electric systems at minimum mass. This was identified at a higher rotational speed of 10000 rpm (upper limit of considered speed range). From an efficiency point of view, the minimum mass systems do show the same transition point as the efficiency optimized systems at 7000 kW. The aluminum conductors are the best choice for architectures below 7000 kW design shaft power. Above 7000 kW the HTS transmission cables achieved the optimum results. This transition point indicates together with the full HTS motor a potential change to full cryogenic electric system architectures. The efficiency of the mass optimized systems is in a range between 96.4% and 96.6%, and is 0.2% lower than the efficiency optimized systems in power ranges below 7000 kW. Above 7000 kW, the efficiency reaches values of 96.6% and is in a similar range as the efficiency optimized systems. Concerning specific powers, the values are between 4.0 kW/kg and 6.9 kW/kg and are 43% higher than those of the efficiency optimized systems. Based on the results of the mass optimized system (1), Figure 5.8 shows the specific power of a dual motor electric architecture for different single motor shaft powers and rotational speeds at minimum system mass.

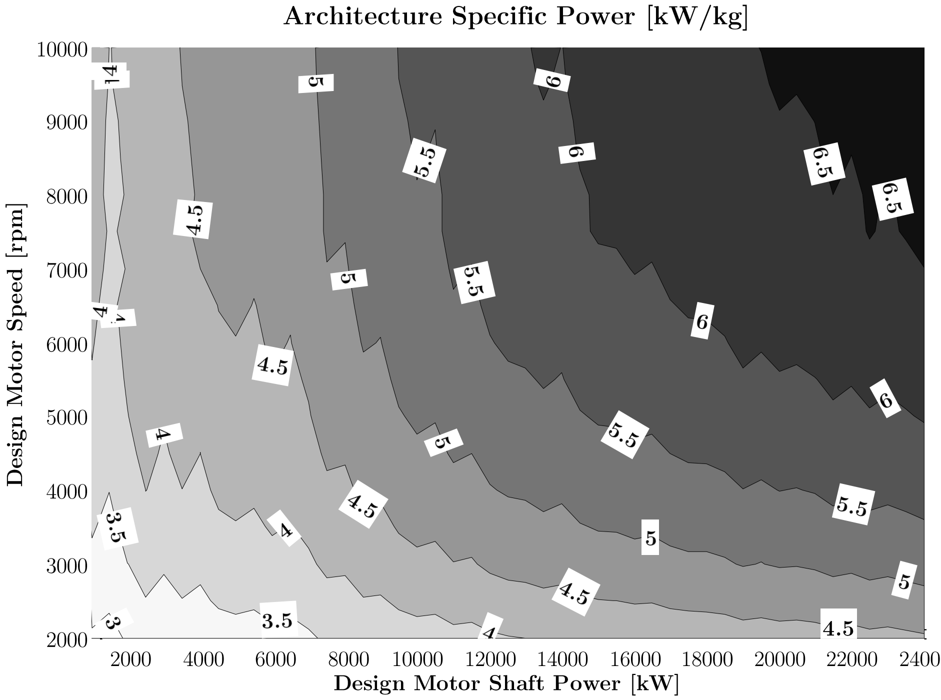

Simulation Settings: - Transmission voltage 2000V - Full HTS motor system - Variable voltage architecture

Figure 5.8: Design space of the specific power of a variable voltage architecture at 2000 V transmission voltage at different design rotational speeds and shaft powers of the electric motor for minimum system mass

The overall electric architecture specific power varies between 3.0 kW/kg up to 6.5 kW/kg depending on the shaft rotational speeds and powers. The discontinuities in the diagram are caused by the multi-level inverter and protection switches. The design efficiency of the variable voltage architecture, shown in Figure 5.9, is also varying for different design rotational speeds and shaft powers. The architecture design efficiency reached values between 96.4% and 96.7%. The sharp efficiency transition area between 6000 kW and 7500 kW indicates the change of the cable type from aluminum to HTS conductors.

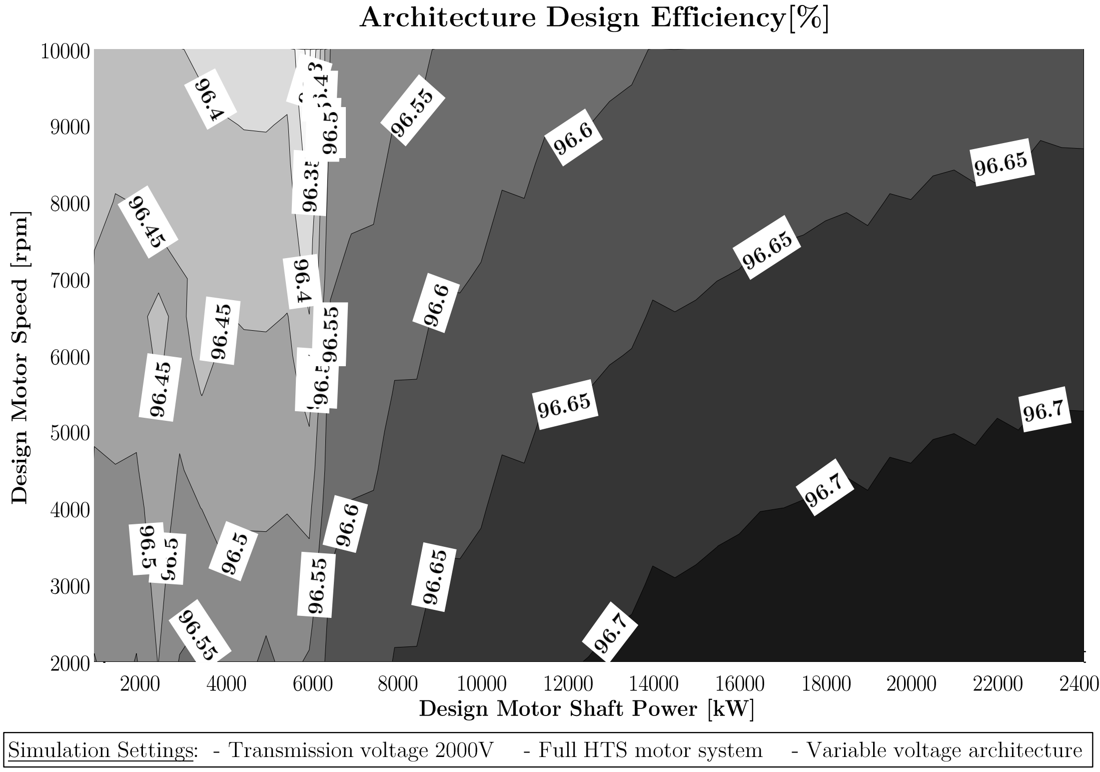

Figure 5.9: Design space of the design efficiency of a variable voltage architecture at 2000 V transmission voltage at different design rotational speeds and shaft powers of the electric motor at minimum system mass

It was identified that the variable voltage architecture is the dominating design option for all considered application cases. Figure 5.10 shows the comparison between the variable and the constant voltage architectures at different design transmission system voltages at a fixed motor voltage of 1000 V and rotational speed of 4000 rpm. These requirements are based on the electric power demand of the BHL Quad-Fan. Based on the results of the previous design space exploration, only full HTS motors and aluminum cables were considered for this comparison. The variable voltage system is shown in column (a) with no converter installed. In column (b) the results of the buck converter are shown, in (c) of the boost and in column (d) of the buck-boost converter. In the first row the loss distribution of the different involved electric components are itemized. It can be recognized that the general trend for all combinations is that with increasing system voltage the total losses also increase,

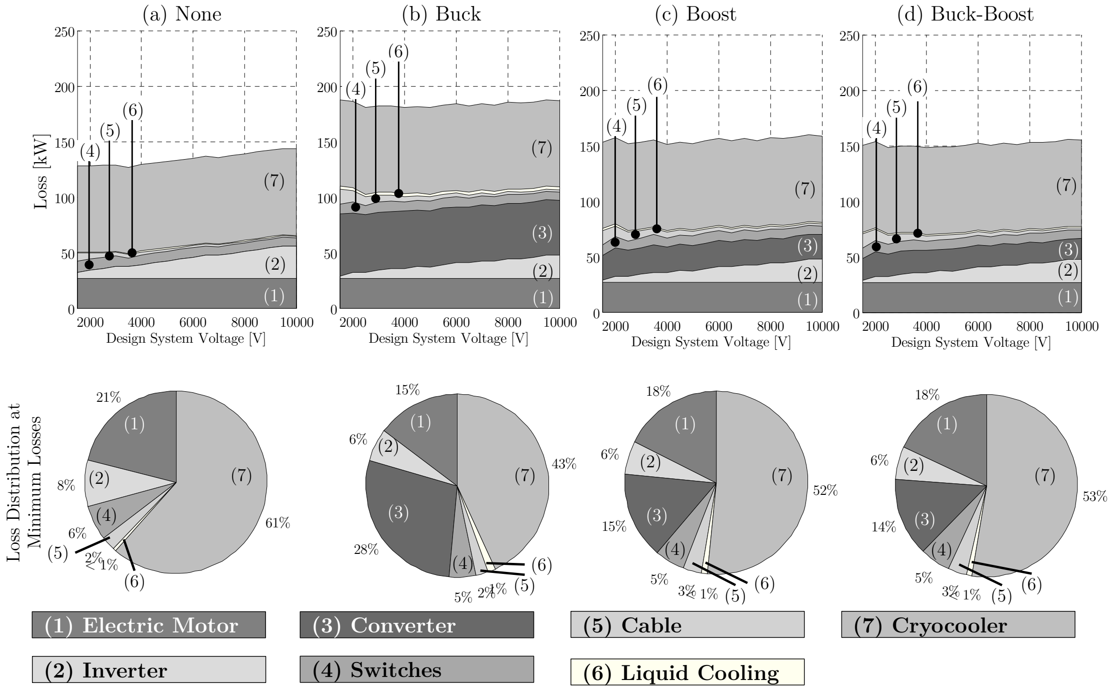

Figure 5.10: Loss distribution of a 2100 kW motor system (at 4000 rpm) utilizing a full HTS motor, aluminum transmission cables and four different architecture options: (a) no converter, (b) buck converter, (c) boost converter and (d) buck-boost converter installed

mainly driven by the inverter. The electric motor shows an independent loss characteristic because the motor voltage is fixed in this scenario. The cable losses are slightly decreasing with increasing system voltage, but are overcompensated by the increased controller losses. The converters are also showing an independent behavior of the choice of the system voltage, caused by the design point of the battery. The design voltage of the battery was also adapted accordingly, implying that the required working potential of the converter maintains. The discontinuities occurring in the charts are due to the parallel and series arrangements of the PSs installed in the inverter, converter and protection devices. The variable voltage architecture (a) shows the lowest total losses of 130 kW. This is 49% lower compared to the buck converter architecture (b). Depending on the voltage design point the efficiency (without battery) of the variable voltage architecture ranges between 96.0% and 97.4%. The boost and the buck-boost converter are nearly showing the same loss distribution, only that the buck-boost variant has 5% lower losses. In case of an installed converter, the inverters in architectures (b) to (d) are operating with a 5.9% higher efficiency than architecture (a). Nevertheless, due to the additionally installed component the overall system losses are higher. The pie charts show for each architecture the relative loss distribution at the individual minimum system total loss. In case of the variable voltage system the cooling system (cryocooler plus liquid cooling system) is responsible for about 42% of the total losses. The other components are in ranges between 12% and 17%. For the constant voltage architectures the loss distribution is slightly different, caused by the additional installed converter. The buck converter (b) causes about 46% of the total losses followed by the cooling system with 24%. The boost (c) and the buck-boost (d) converter are nearly showing the same loss distribution between 25% and 29%. The cooling system is between 31% and 32%. The other components are contributing to the same amount.

Compared to the loss distribution the same approach was also performed to analyze the mass distribution given in Figure 5.11.

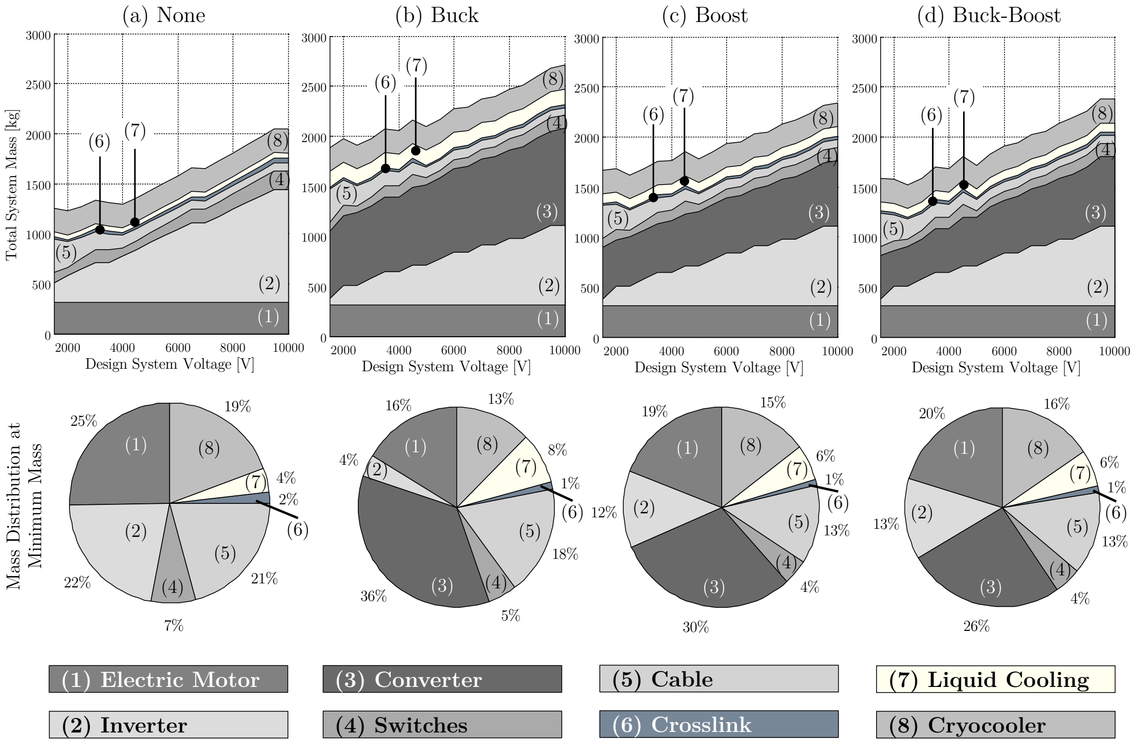

Figure 5.11: Mass distribution of a 2100 kW motor system (at 4000 rpm) utilizing a full HTS motor, aluminum transmission cables and four different architecture options: (a) no converter, (b) buck converter, (c) boost converter and (d) buck-boost converter installed

The charts include the mass of the crosslink that connects the individual electric power train systems and has no impact on the losses during normal operation because blocking losses were neglected. This component is only required in abnormal mode of operation, but influences the total system mass. The first row covers the detailed mass distribution for the four different architecture options at different system design voltages: no converter (a), buck (b), boost (c) and buck-boost (d) converter. The mass of the electric motor is independent like the loss characteristic. The inverter mass and protection switches increase with increasing design system voltage. The cable mass is slightly decreasing with increasing system voltage, while the mass of the crosslink and the cooling system is nearly constant. Due to the used aluminum cables, the mass optimum for the variable voltage system (a) is at 2000 V. The specific power is in ranges between 1.9 kW/kg and 3.8 kW/kg. The converter based architectures have their mass optimum at lower voltages of around 1500 V near the electric motor voltage. The inverter designs of the constant voltage architectures are 66.6% lighter than those of the variable voltage architectures. This mass saving is compensated by the converter mass. The mass of the converter and the protection switches are increasing with increasing system voltage. The cable masses decrease with increasing system voltages, while the cooling system and the crosslink switches are nearly constant.

5.3.2 Electric Ducted Fan Sizing

This section presents the results of the second study. It covers the identification of potential coupling options between the ducted fan, the electric motor system including the PMAD and a gear box at different sizing points of the electric motor. The impact of the variation of the GR and design thrusts of the EDF on the TSPC and the overall system mass can be taken from Figure 5.12. The electric system architecture was sized according to the results of the previous section using a variable voltage system at 2000 V and a full HTS motor system.

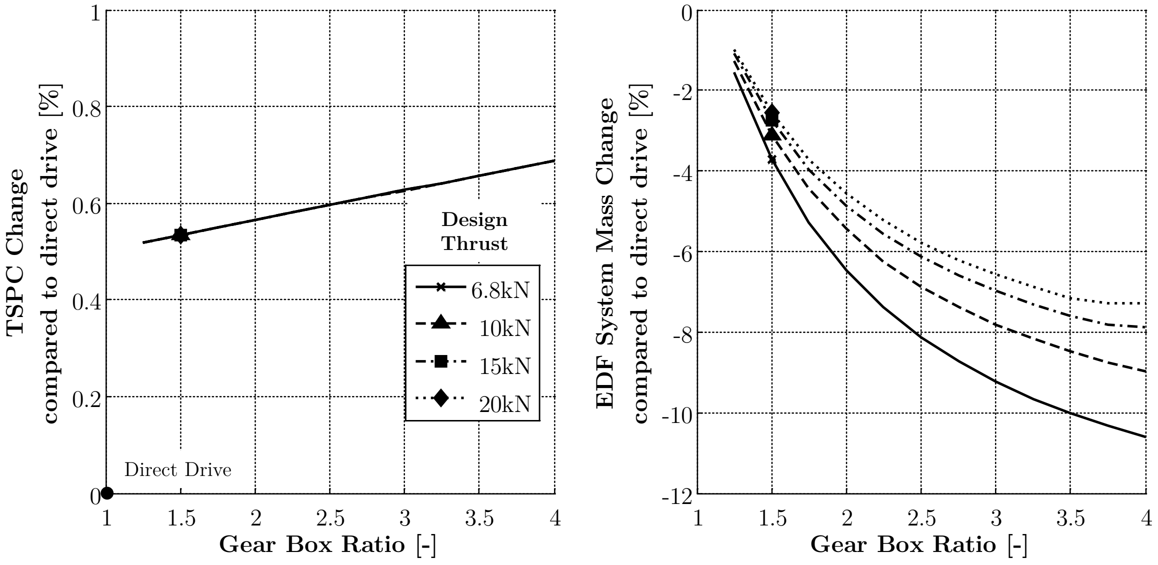

Figure 5.12: Results of the impact of the gear box ratio on the TSPC (left) and the overall EDF mass (right) based on [121] (legend is valid for both plots)

With these described methods, the variation of the GR leads to a decreasing overall efficiency, indicated by an increasing TSPC. However, the TSPC increase is below 1%. The overall system mass decreases with increasing GR up to 10.5% compared to a direct drive system. For that purpose, a trade-off between mass and efficiency has to be made for a suitable design at the system level. At the current design stage, the driving parameter of the design at the overall aircraft level is unknown. Therefore, a GR of 2 was assumed for the further system level studies. In the first instance, this design choice represented a suitable trade-off between mass and efficiency and will be reevaluated at the overall aircraft level. Furthermore, to identify potential sizing points of the electric motor the standard compressor maps of an EDF were transferred to a Q-n-diagram. This is accomplished by varying the off-design altitude, Mach number and thrust lever position of the EDF to evaluate the resulting fan shaft rotational speed and torque for different design thrusts. Figure 5.13 represents a normalized map for a thrust design range between 5 kN and 20 kN. It marks the three discussed potential sizing points of the electric motor relative to the sizing point TOC.

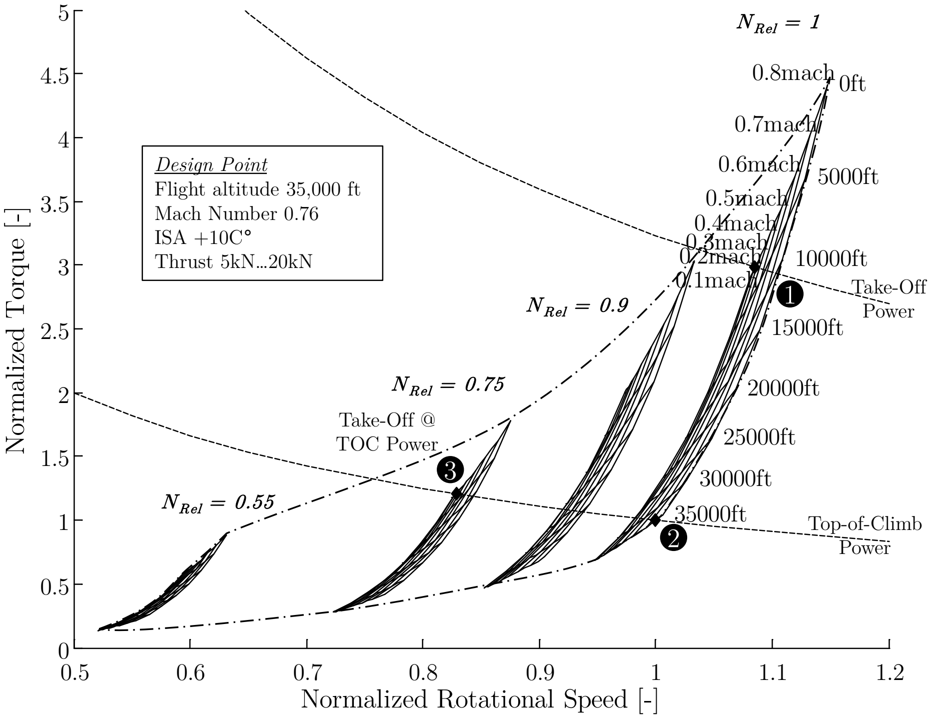

Figure 5.13: Results of the normalized torque-rotational speed map of the EDF for a thrust design range of 5 kN to 20 kN marking important flight state demands according to [121]

The TO point referred to Scenario No.1 requires a three times higher torque demand and an approximately 8% higher rotational speed than the sizing point in TOC, defined as Scenario No.2. The higher torque demand is directly driven by the difference in air density and corresponds to the required power demand. When operating the EDF at TO conditions with equivalent TOC power (Scenario No.3) the torque demand increases by 21% at a 17% reduced shaft speed compared to TOC conditions. This is equivalent to a relative corrected speed of approximately 75%. The different possibilities of the motor sizing points were assessed for the reference thrust requirement of 6.8 kN. The thrust is based on the hybrid-electric reference aircraft [21], which was sized for a design value of H_P of 30% in TOC. The results for these sizing considerations are listed in Table 5.3. It can be recognized that Scenario No.1 results in an overall system mass of 2151 kg and is equal to an overall specific power of 3.15 kW/kg. The efficiency is 70.6% during TOC conditions. The available TO thrust is reduced by 67.6% when changing the sizing point to Scenario No.2 compared to Scenario No.1. The system mass decreases by 54% and increases the TOC efficiency to 72.4%. The reduced available TO thrust can be partially compensated by changing the motor sizing point as performed with Scenario No.3. A thrust increase of 24.8% can be accomplished, but this is still 57.8%

less than for Scenario No.1. Due to the changed sizing point the electric motor gets 17.3% and the gear box 23.5% heavier compared to Sizing No.2.

Table 5.3: Impact on different motor sizing options of an EDF on the thrust performance for a 6.8 kN design thrust (reference H_P =30%) taken from [121]

	Unit	Scenario No.1		Scenario No.2		Scenario No.3	
		TO	TOC	TO	TOC	TO	TOC
Thrust	[kN]	36.1	6.8	12.6	6.8	15.6	6.8
Motor Shaft Power	[kW]	6777	2116	1625	2095	2095	2095
Motor Speed	[rpm]	6428	6255	4822	6255	5183	6253
Total Efficiency	[%]	36.7	70.6	52.0	72.4	49.9	72.2
Electric Motor	[%]	99.1	98.7	99.1	99.1	99.1	99.1
PMAD*	[%]	97.8	96.6	97.9	97.7	97.8	97.5
Gear Box	[%]	99.5	98.5	99.5	99.5	99.5	99.4
Fan	[%]	38.1	75.2	53.9	75.2	51.7	75.2
Total Mass	[kg]	2151		998		1020	
Electric Motor	[kg]	270		104		122	
PMAD*	[kg]	1400		447		447	
Gear Box	[kg]	51		17		21	
Fan	[kg]	430		430		430	
Specific Power	[kW/kg]	3.15		1.63		2.05	

* include cooling

Nevertheless, the overall system mass of the EDF only increases by 2.3%. The adapted sizing point has a further implication on the electric motor sizing because the changed gear box design point to TO leads to slight efficiency changes compared to Scenario No.2. This effect forces a minor oversize of the electric motor power to meet again the torque demand during TOC.

5.3.3 Sizing of Hybrid-Electric Power Train at the System Level

Based on the findings of the previous section, the DPH power train was analyzed at the system level. For that purpose the potential sizing points of the electric motor of the EDF were linked with the GTF characteristics. Table 5.4 shows the results of the DPH system for the hybrid-electric reference aircraft with the corresponding thrust requirements for TOC, TO AEO and OEI at a H_P of 30%. The thrust requirements for OEI also include the OMI abnormal mode case that represents an inoperative EDF.

The different motor sizing options are impacting the design point of the GTF. Using motor sizing Scenario No.1, the GTF is sized for TOC conditions and is driven by the sufficient installed thrust of the EDFs. This high power sizing of the electric system is also reflected in the system mass. The EDF mass is nearly equal to the GTF mass, but is only delivering 42% of the GTF thrust in TOC conditions. The sizing thrust changes from TOC to TO conditions when downsizing the electric system via the changed electric motor sizing points as performed with Scenario No.2 and No.3. This can be recognized for Scenario No.2, where the GTF has to

Table 5.4: Hybrid-electric system performance for the different motor sizing options according to [121]

	Unit	**Scenario**		
		No.1	**No.2**	**No.3**
GTF Design Thrust[a]	**[kN]**	16.2	18.8	17.4
GTF TOC Thrust[a]	**[kN]**	16.2	16.2	16.2
GTF TO Thrust[b]	**[kN]**	70.9	82.4	76.4
EDF TOC Thrust[a]	**[kN]**	6.8	6.8	6.8
EDF TO Thrust[b]	**[kN]**	36.1	12.6	15.6
Total Installed TOC Thrust[a]	**[kN]**	46.0	51.2	48.4
Total OEI Thrust[b]	**[kN]**	143.1	107.6	107.6
Total OMI Thrust[b]	**[kN]**	177.9	177.4	168.8
TSPC TOC[a]	**[W/N]**	516	503	507
Total Mass	**[kg]**	8726	7292	6860
Total Gas Turbine Mass[c]	**[kg]**	4424	5296	4818
Total EDF System Mass	**[kg]**	4302	1996	2042

[a] Altitude 35,000 ft, Ma 0.76, ISA +10°C
[b] SL, Ma 0.2, ISA +10°C
[c] without pylon weight
grey areas mark DPH thrust sizing requirement

be oversized by 16% compared to Scenario No.1. This results in a 20% higher mass. However, the electric system architecture can be downsized and ends up in a 53.6% lower overall EDF mass. At the overall system level, this sizing scenario leads to a mass reduction of 16.4% compared to Scenario No.1. The efficiency increases by 2.5% in TOC conditions driven by the better GTF efficiency. Increasing the utilization of the electric system, as performed with Scenario No.3 via the changed motor sizing point, leads to a further reduction of the GTF sizing thrust of 7.5% compared to Scenario No.2. This reduces the GTF mass by 9.1%, but the EDF mass increases by 2.3%. Nevertheless, the overall hybrid-electric system mass can be reduced by 5.9% compared to Scenario No.2, including a decrease in system efficiency by 0.8%. Keeping the design thrust of the EDF fixed at 6.8 kN leads to a variation of the design H_P in TOC conditions due to the changed GTF sizing points. This H_P change was in marginal ranges below 1%. The previously presented results were only valid for a H_P of 30%. Figure 5.14 and Figure 5.15 open up the design space and vary the design H_P in a range between 0% and 50% to identify if the sizing thrust trends are also valid for other values of H_P.

For this approach the thrust requirements were kept constant at the reference hybrid-electric aircraft values of H_P 30%. This system sizing analysis is representing a retrofit of the reference aircraft keeping the MTOW constant and changing the design range, in the first instance. The point at H_P 0% is equal to the conventional GTF powered non-hybrid-electric aircraft at the reference thrust requirements. The total hybrid mass of Scenario No.1 is the heaviest solution for values of H_P higher than 8%. The total DPH mass for Scenario No.2 and No.3 is relative constant up to a H_P of 15%. This is driven by a balance between the GTF mass

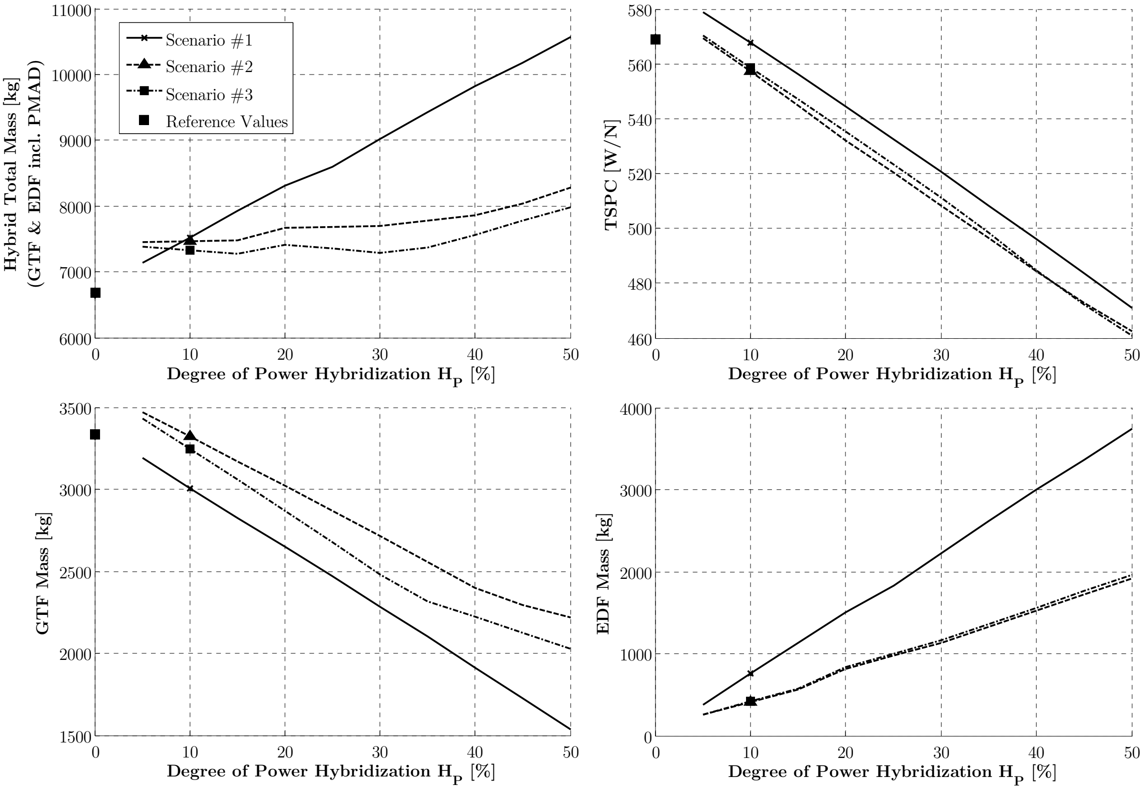

Figure 5.14: Impact of the degree of power hybridization on the single subsystems at the system level

reduction and the EDF mass growth in this range. The efficiencies are tending to getting better with increasing values of H_P. Only for values of H_P lower than 8% the conventional GTF seems to be the more efficient and lighter option at the system level. The mass difference between Scenario No.2 and No.3 is between 0.8% for low values of H_P and up to 5.6% for high values of H_P. The efficiency difference can be neglected. The higher mass gradient at higher values of H_P for Scenario No.2 and No.3 is driven by the thrust requirement change (cf. Figure 5.15). Scenario No.1 is always driven by TOC thrust requirement, while Scenario No.2 and No.3 are driven by the OEI sizing case up to H_P 40%. For higher values of H_P the requirement changes to the AEO thrust requirement. This change occur for Scenario No.3 at a lower H_P than for Scenario No.2. This is caused by the smaller gas turbine sizing of Scenario No.3.

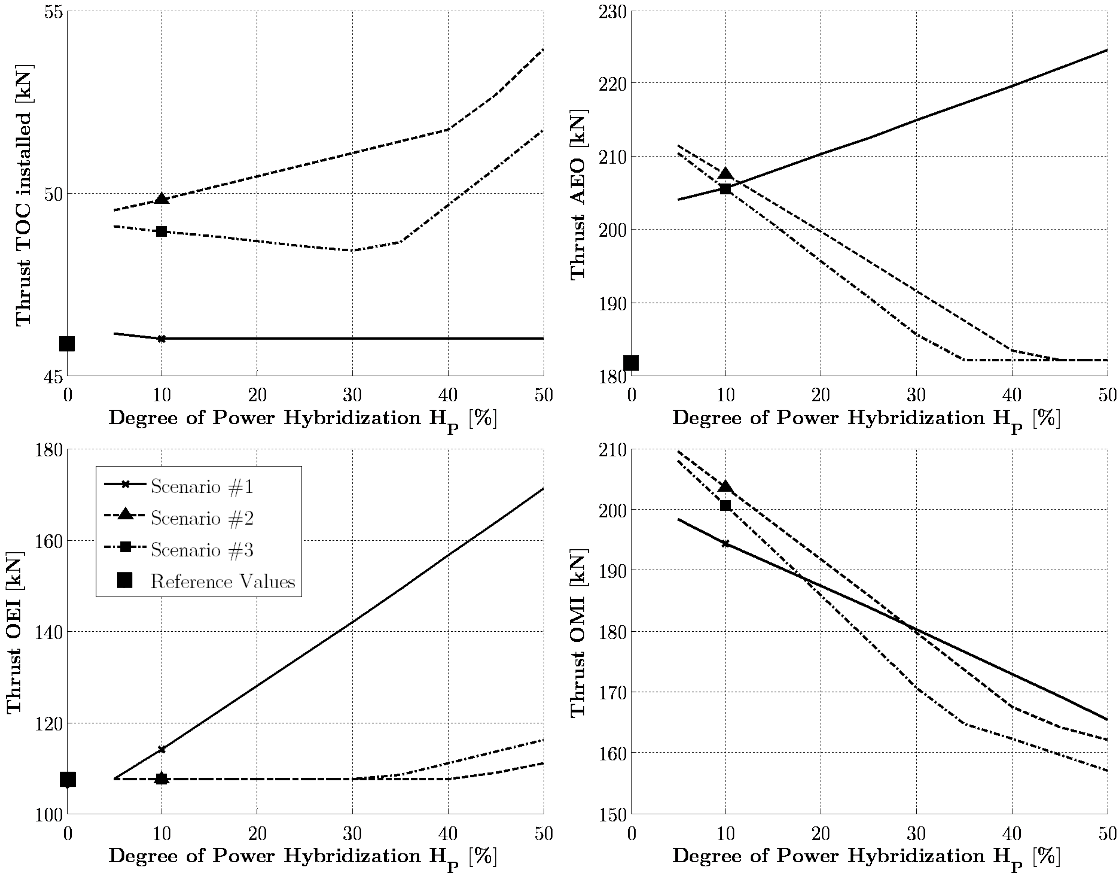

Figure 5.15: Impact of the degree of power hybridization on the resulting thrust levels at the system level

5.3.4 Sizing of Hybrid-Electric Power Architecture at the Aircraft Level

In the previous study Scenario No.3 was identified as the most suitable sizing option of the electric system architecture at the system level. This sizing scenario served as a basis in study four for a detail investigation of the DPH power train at the overall aircraft level. Furthermore, the DPH power train was analyzed with regard to four different mission hybridization options as described in Section 5.2. For that purpose, the battery system is sized with a residual SOC of 10% at the end of the mission, representing a 20% SOC at the end of the block mission. The design H_P was varied between 0% (reference aircraft) up to 45%. This value was identified as upper convergence limit for this aircraft configuration. As a result the most important aircraft and mission specific parameters have been plotted over the design values of H_P visualized in Figure 5.16 and Figure 5.17. It can be recognized that there are different optima for different mission hybridization strategies. Concerning the highest in-flight fuel reduction potential the hybrid strategy EDF_{max} is leading to the best result of the considered design space. The highest fuel demand is caused by the hybridization strategy GTF_{max}, where the GTF are delivering in all flight segments their maximum possible thrust. In this case the fuel demand is even increasing for low design values of H_P. This is caused by the increasing electric system mass and, in turn, MTOW with increasing H_P. In most cases the GTF are able to power the aircraft for this hybridization strategy. The electric system is not in use and hence, dead weight. When focusing on a minimum mission energy demand or even overall minimum CO_2 generation the operating strategy, where the gas turbines are running in their SFC optimum, are resulting in the best solution. However, due to the additional electric system mass the total mission energy demand is still higher than the reference.

Beside the different mission parameters, the aircraft design parameters are also showing different behaviors for the various design values of H_P and hybridization strategies. Figure 5.16 covers the most important design masses of the aircraft. The DPH system mass and the individual sizing points of the single thrust generating devices are shown in Figure 5.17. It can be recognized that for higher ranges of H_P and hybridization strategies, the GTFs can be downsized with regard to the TOC design thrust compared to the reference aircraft. Only for the hybridization strategy EDF_{max} the sizing thrust of the GTF is increasing with increasing values of the design H_P. This is caused by the over proportional increase of the MTOW and, in turn, the required thrust demand. The lowest gradient in mass increase is provided by the hybridization strategy GTF_{max}.

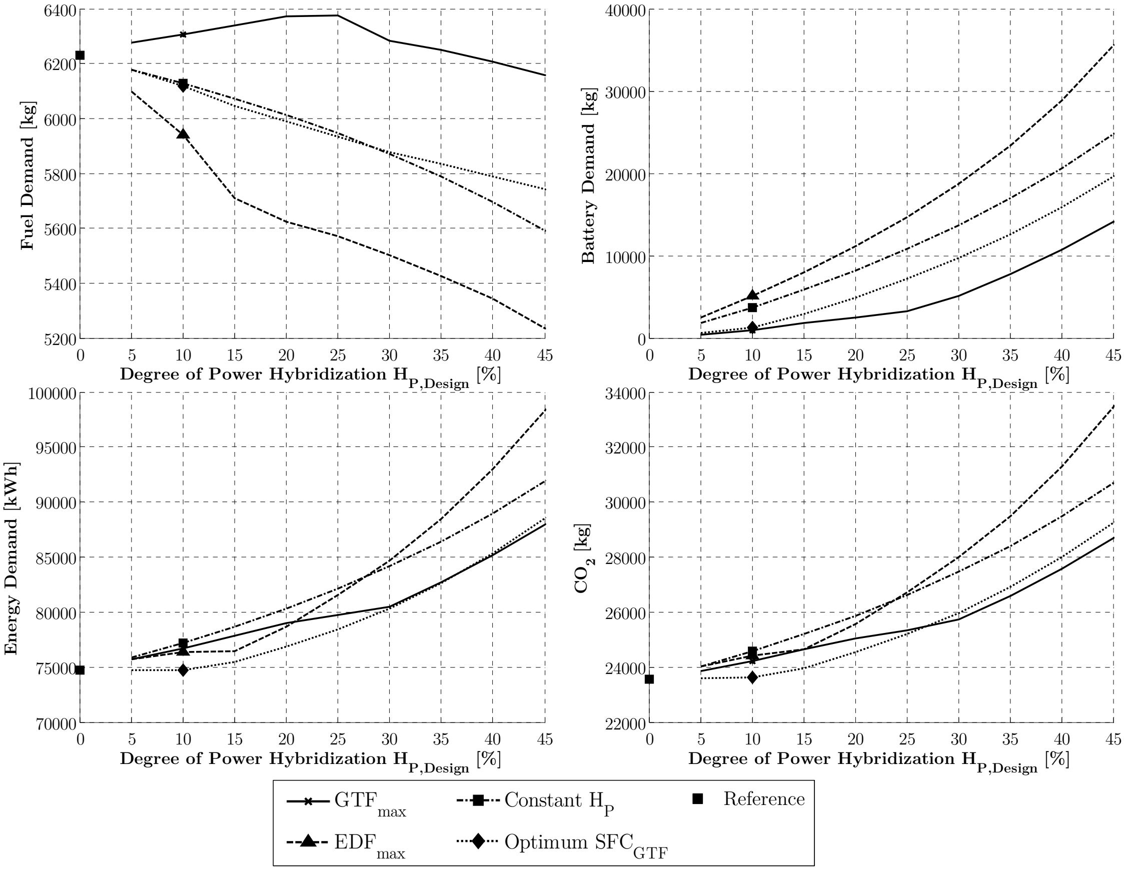

Figure 5.16: Aircraft level results of fuel, battery, total energy demand and generated CO_2 for the four various hybridization strategies

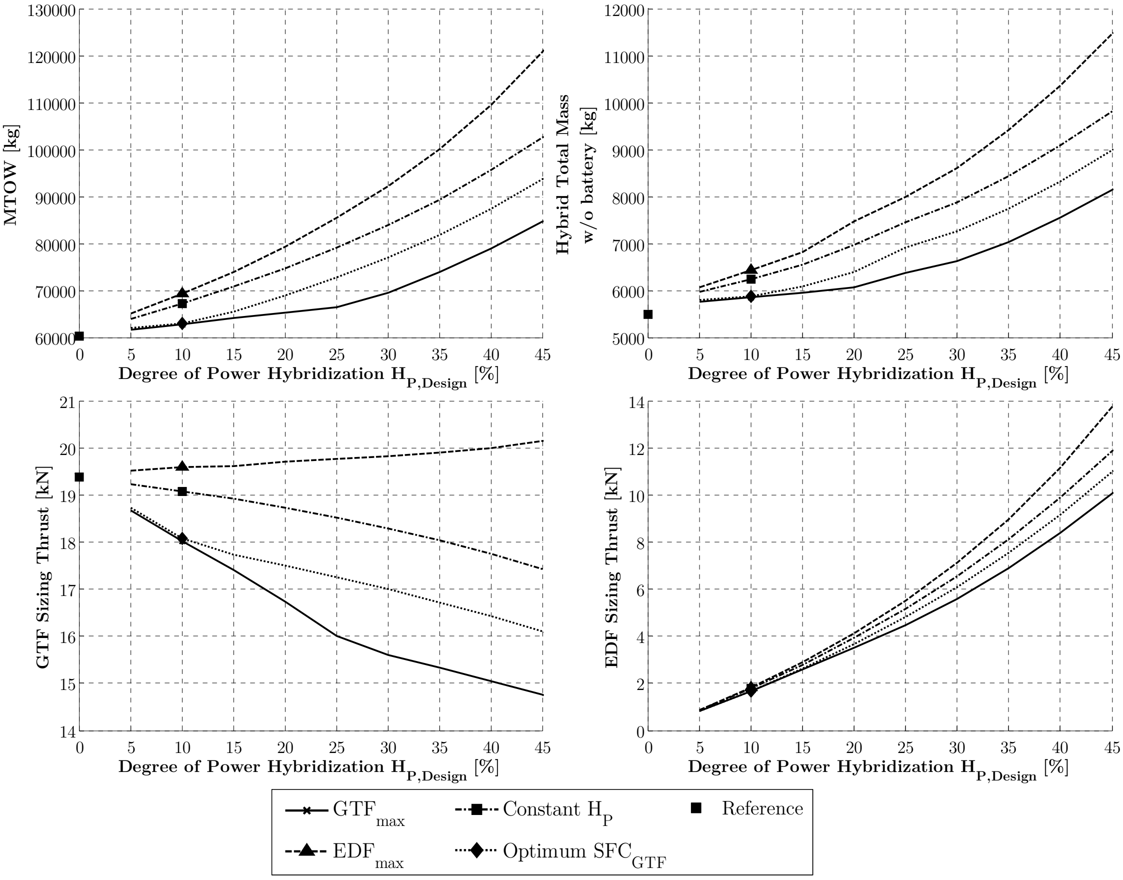

Figure 5.17: Aircraft level results of MTOW, propulsion mass and sizing thrusts of GTF and EDF for the four various hybridization strategies

Figure 5.18 compares the different hybridization strategies and design values of H_P with the 2035 non-hybrid-electric reference aircraft. The datum is always better than the hybrid-electric derivatives with regard to overall mission energy and generated CO_2 emissions with the projected electric energy mix for 2035. Only when assuming a completely renewable or CO_2-free generation of the electric energy (cf. Figure 5.18 (c)) an advantage of the hybrid-electric system can be established. In this case, the hybridization strategies EDF_{max}, constant H_P over the mission and operating the GTFs in their optimum SFC point are providing a CO_2 benefit for values of H_P greater than 5%. The hybridization strategy EDF_{max} is delivering the best results with up to 15% CO_2 reduction potential. However, as also shown in Figure 5.17 this hybridization strategy causes the highest aircraft masses.

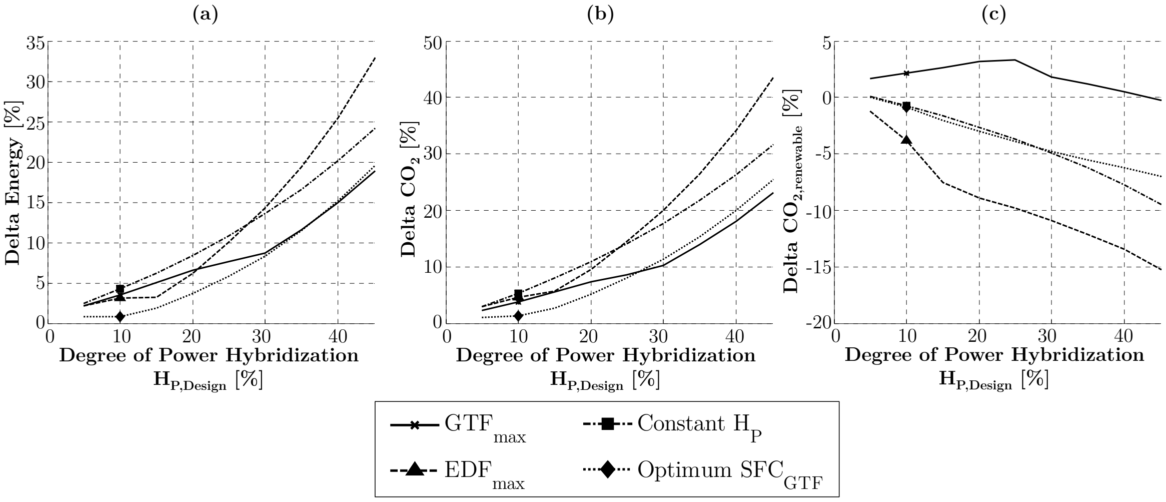

Figure 5.18: Comparison between the different hybridization strategies and the reference aircraft. (a) Energy change, (b) CO_2 change, (c) CO_2 change if CO_2-free electric energy is used

For a detailed assessment of a suitable DPH aircraft configuration the most relevant parameters were compared each other in Figure 5.19.

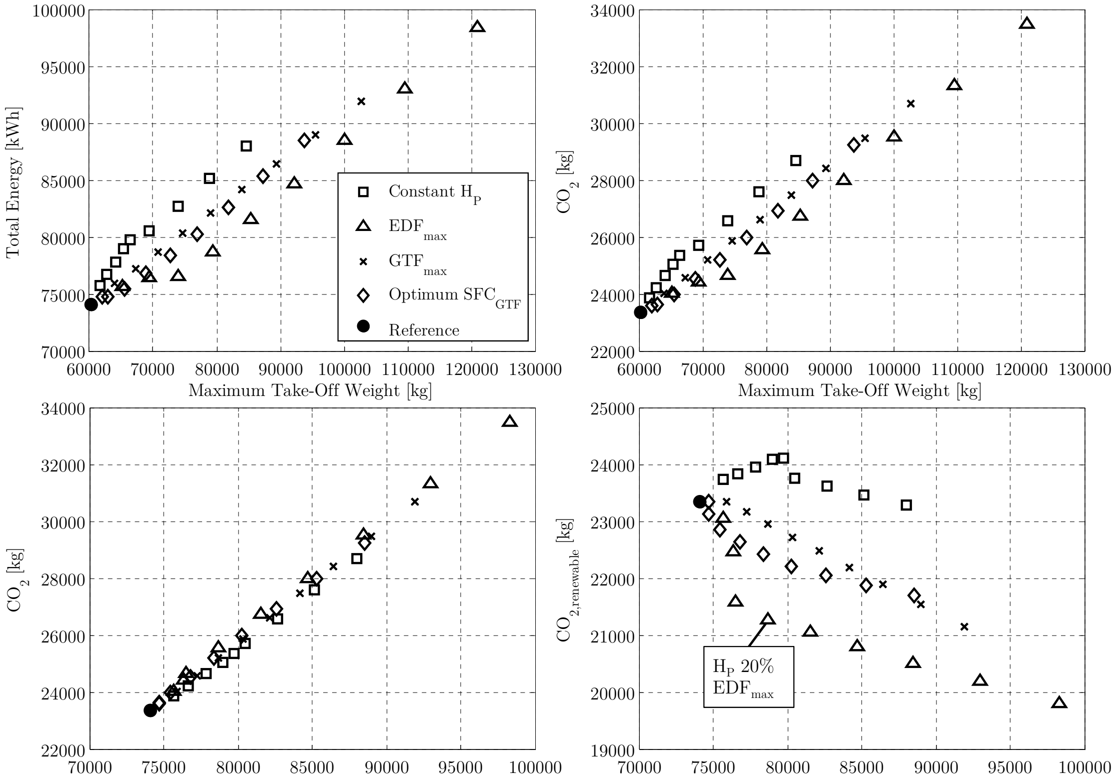

Figure 5.19: Aircraft level results for the most relevant figure of merits for different values of design degree of power hybridization and hybridization strategies of the discrete parallel hybrid-electric platform

In order to identify an optimal solution a promising hybrid-electric configuration should provide minimum value ranges of the considered objective parameters. This representation should help to identify a suitable hybrid-electric aircraft enabling a feasible trade-off between a CO_2 reduction potential and MTOW increase. Such a configuration is delivered by the hybridization strategy EDF_{max} at a design H_P of 20% resulting in a CO_2 reduction potential of about 8.9% at a moderate increase of the MTOW of 31.6%. However, the overall mission energy is about 7.4% higher than for the reference aircraft. Nevertheless, for a deeper investigation of the systems this hybridization strategy is analyzed in more detail.

The relative mass distribution of the different designs at the aircraft level, covering for example relative airframe and power plant masses based on the datum aircraft, can be gathered from Figure 5.20.

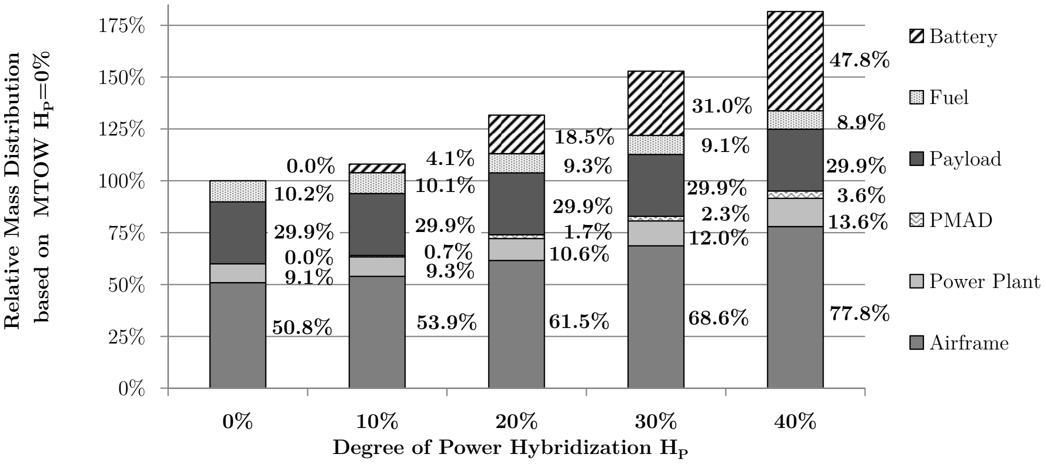

Figure 5.20: Relative mass distribution for the various hybridization values of H_P for hybridization strategy EDF_{max}

Compared to the conventional kerosene supplied aircraft the hybrid-electric aircraft with a H_P of 40% is more than 75% heavier. This corresponds to an increase in the operating empty weight of 6.9%. The main mass driver is the battery. The power plants are representing the GTFs and the equipped EDFs with electric motor and controller-inverter unit. The PMAD system covers busses, cables, protection switches and the thermal management system and accounts for maximum 3.6% of the overall aircraft mass. The entire propulsion system mass including the required fuel and battery mass accounts for 70.3% for the variant of H_P 40% based on the reference MTOW. This mass is 3.6 times higher compared to the non-hybrid-electric system. It can be also recognized that the battery mass is increasing above average with increasing H_P. Figure 5.21 gives the results of the electric system architecture performance for the entire mission and the off-design performance maps at the dedicated flight states TO, TOC and mid cruise for the design H_P of 20%.

From Figure 5.21 it can be seen that the mission was calculated in a way that the EDFs are delivering the maximum installed power in all flight phases where possible. This was the

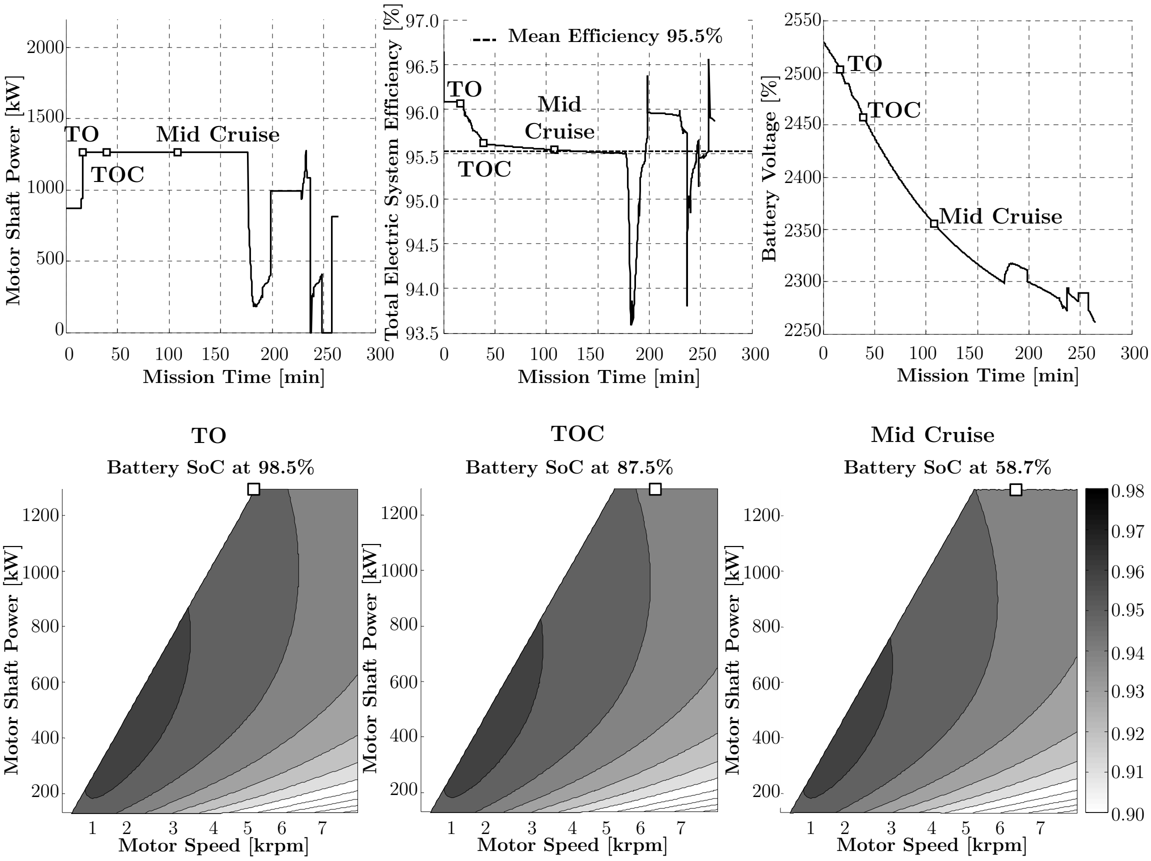

Figure 5.21: Performance of the electric system architecture during the design mission (top) and the corresponding electric system architecture maps at the three characteristic flight states TO, TOC and mid cruise (bottom) for a H_P of 20% and hybridization strategy EDF_{max}

case for the TO, climb and cruise phase. This operation mode implied that the H_P is not a control parameter but an outcome during the different flight phases. During climb the H_P varies between 8% and 20%, during cruise the H_P is higher than the design H_P at around 24%. Depending on the power demand the efficiency varies between 96.6% and 93.5% over the mission. The highest efficiency was achieved when requesting the maximum installed power during TO, climb and after go-around. The mean efficiency of the electric system architecture is around 95.5%. The maximum efficiency of the electric systems architecture was reached during part load conditions of around 40% relative power and rotational speed shown in the performance maps. With decreasing SOC the high efficiency area is shrinking. This is mainly driven by the battery efficiency. However, the efficiency of the PMAD system is increasing with decreasing battery output voltage, because the PMAD system was designed for a transmission voltage at SOC 0%. Nevertheless, the battery performance is dominating the overall systems efficiency. During normal operation the electric system operated at the maximum power demand for this hybridization strategy and did not reach the optimal efficiency area.

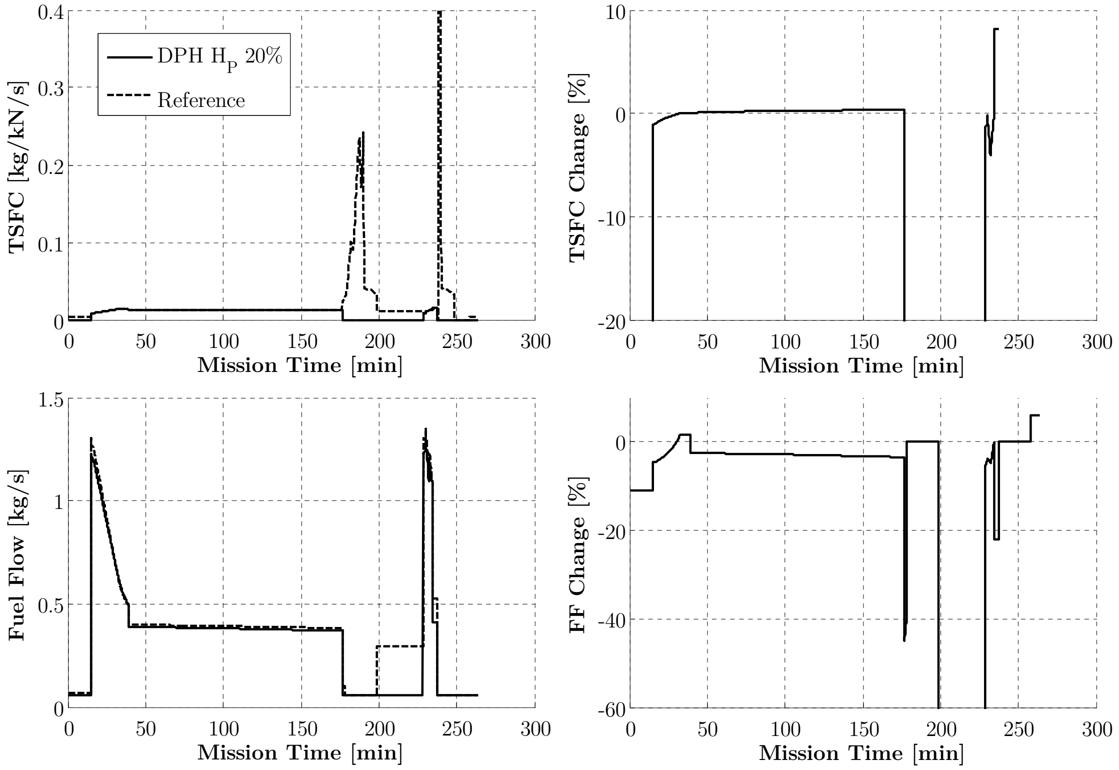

Figure 5.22: Comparison of the geared turbofan performance of the discrete parallel hybrid-electric aircraft with H_P of 20% and hybridization strategy EDF_{max} and the reference propulsion system

The mission characteristics of the single GTF are visualized in Figure 5.22. In this figure the GTF of the reference aircraft and the DPH variant are compared. It can be recognized that the TSFC of the hybrid-electric GTF was during cruise slightly higher than for the reference aircraft. This was mainly caused by the fact that the GTF run in deeper part load conditions compared to the reference GTF although the sizing thrust of the hybrid electric variant is 9.7% higher than compared to the reference aircraft (see Figure 5.17). However, during cruise the absolute thrust was lower than of the reference GTF and results in a lower absolute fuel flow as shown in the bottom plots of Figure 5.22. This is the reason why this concept offers a 9.8% reduction in in-flight fuel burn, which is equal to the same amount of in-flight CO_2 when considering a renewable electric energy source.

5.4 Discussion of Results

The following section discusses in detail the previously presented results of the electric system architecture designs, the ducted fan sizing options and the assessment at the overall aircraft level. This includes the critical assessment of assumptions of parameters. The assessment of the influence of these parameters is performed via sensitivity studies.

5.4.1 Discussion of Electric Architecture Design and Electric Ducted Fan Coupling

Different technology options were considered for the electric architecture design to identify their impact at the overall system mass and efficiency. Hereby, HTS based electric motors were identified as an eligible solution for a broad bandwidth of shaft power requirements to increase overall system performance and to reduced system mass (cf. Figure 5.7). This motor type has the disadvantage that it requires low operating temperatures around 50 K. As mentioned in Section 3.6, active cryocooler systems were used to compensate the losses of the electric motor. One effect that has not been considered is the heat transfer, when coupling a non-cryogenic system with a cryogenic system. For example, such a linkage is applied between the inverter and the electric motor. This linkage requires in reality special heat shielding to avoid quenching of the HTS coils and conductors. Furthermore, concerning the results of Figure 5.7, a transition area at around 7000 kW was identified, where HTS cables (or even full cryogenic electric architectures) could be a preferable solution with regard to overall system mass and efficiency. However, the used HTS cable model considers a constant specific mass of 5 kg/m showing no sensitivity with regard to the transmitted power. Normally, HTS cables also show a sensitivity concerning the transmitted electric current to ensure operation below the critical current density as for example investigated by Schlachter et al. [132]. Furthermore, when using a HTS transmission system for a battery supplied electric architecture, coupling systems have to be taken into account between battery and cable as shown by Allweins et al. [133]. If these open points are implemented in the design of a superconducting electric systems architecture, the mentioned transition area would shift to higher power demands, as it would increase the overall system mass. Because these devices are not free from losses, the electric system efficiency is also decreasing.

The modeling of the electric components was, in most cases, based on scaling relations using a baseline component configuration. The electric motor design is mainly scaled according to handbook methods to the targeted design parameters such as rotational speed and power. This scaling approach does not account for changes in the electric motor architecture, for example, a change in the number of pole pairs. This can influence the motor inverter-controller unit. Furthermore, the performed architectural studies only considered a fixed electric motor voltage of 1000 V and a fixed cable length of 42 m for all configurations. These settings lead to an optimal system voltage for all configurations near the electric motor voltage, U_{Mot}. In Figure 5.23, U_{Mot} and the transmission voltage, U_{Elec}, were varied to identify if this trend is also valid for different ratios of transmission voltages versus motor voltages. The focus in this sensitivity study was only set on the PMAD level because the electric motor model does not cover a design voltage variation. Nevertheless, it can be recognized that for low power demands low voltage motors seem to be a better option with regard to system mass. This effect is mainly caused by the protection switches and the motor inverter-controller unit that can be sized smaller, at efficiency changes lower than 0.2%. In general, the trend of increasing mass and decreasing efficiency with increasing voltage ratio is valid for a broad range of electric motor voltages and shaft powers.

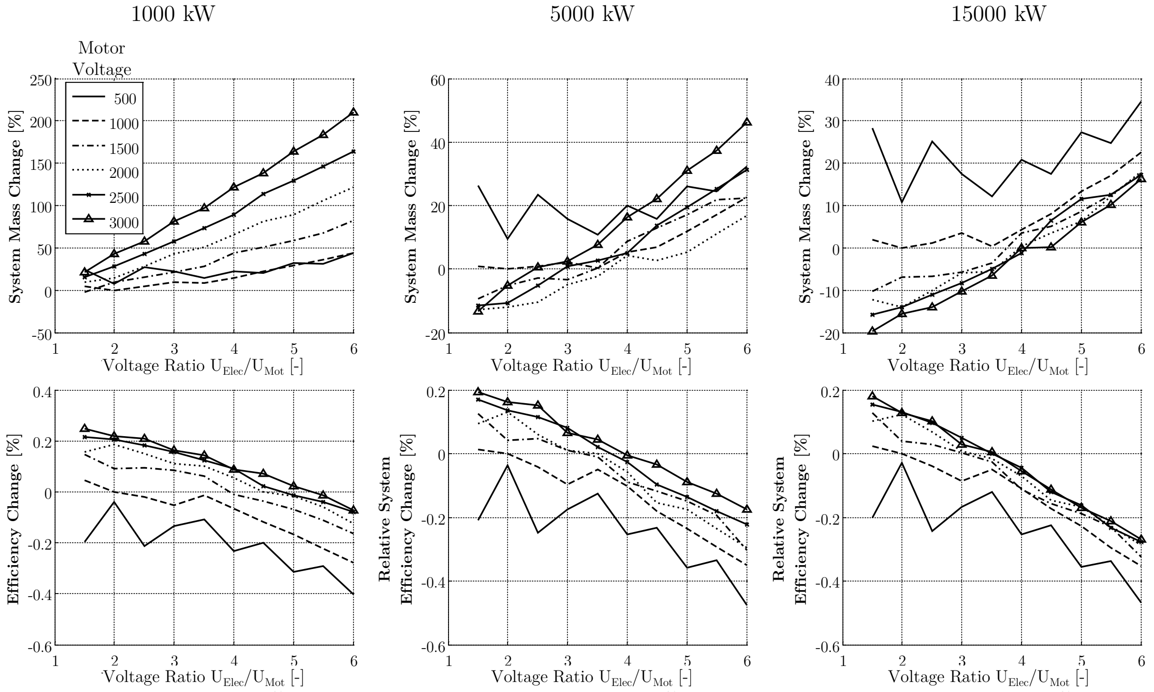

Figure 5.23: Sensitivity of the ratio of transmission voltage to the motor voltage at different motor shaft powers at constant cable length of 42 m

As shown in Figure 5.23, the optimal system voltage is near the motor voltage for a considered cable length of 42 m. Figure 5.24 shows the impact of the optimum system voltage when increasing the cable length up to 3.5 times of the baseline architecture used for the DPH aircraft. The sensitivity study also includes a variation of the electric motor shaft power. In this scenario aluminum cables were assumed for all transmission power demands. The trend indicates an increasing system voltage with increasing cable length and obviously an increasing overall system mass. The higher system voltage is forced by the reduced electric current for a constant transmission power that is the main sizing parameter for the conductor of the cables.

Another open point concerning the estimation of the system masses represents the level of detail of the thermal management system model. For example, the liquid cooling system is only covered with constant values for pressure losses within the cooling tubes and constant temperature gradients within the heat exchangers. In the present study, no altitude effects were considered such as changes in the surrounding temperature levels or air density. Fur-

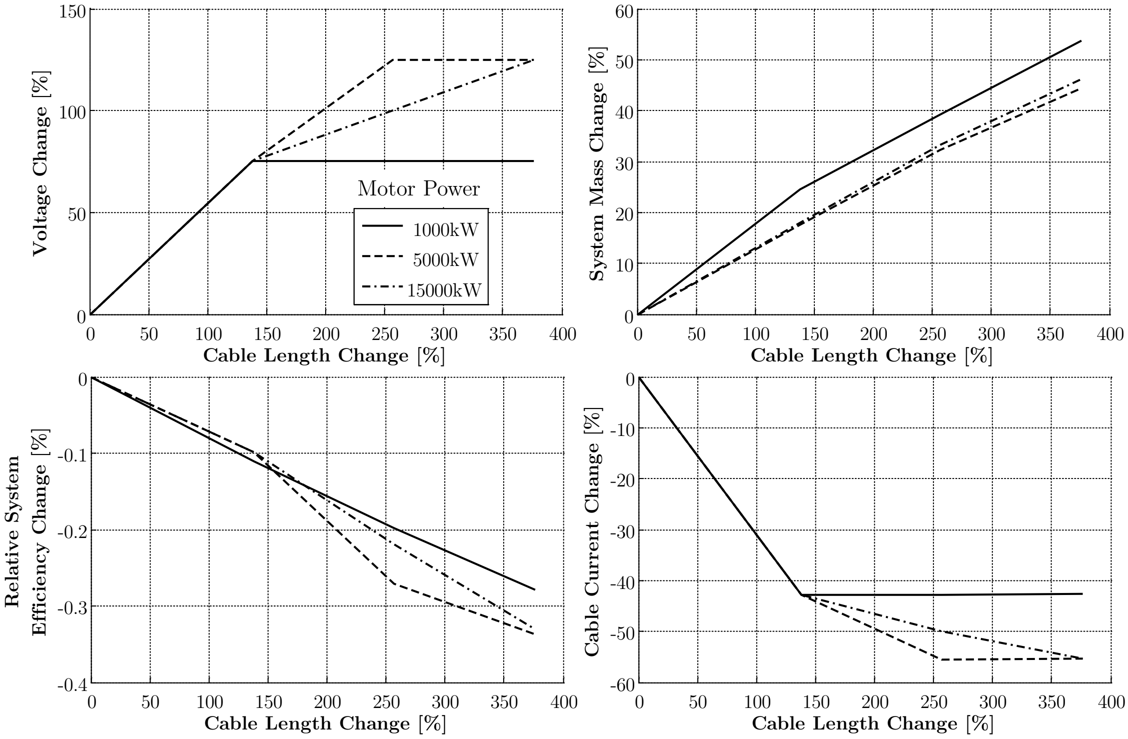

Figure 5.24: Sensitivity study of the optimal voltage for different cable lengths and motor shaft powers at fixed motor voltage of 1000 V

thermore, the considerations were only made at the system level. An important point when dimensioning the thermal management system is to find suitable cooling areas at the aircraft including the required heat exchangers and corresponding tubings. It has to be identified if the cooling areas could be a constraining parameter, when sizing the electric system. This can be also a limiting factor when defining a specific value of H_P. The thermal management system is responsible for around 50% of the total losses according to Figure 5.10. However, the losses in this figure are not directly representing the actual heat load of the system, as the required cooling power demand to operate the cooling pumps is accounted for as parasitic loss. Therefore, the actual heat load will be around 50% of the shown loss distribution for a 2100 kW system. It is expected that the impact of these heat levels for the considered power ranges can be neglected at the overall aircraft level.

The presented results of the electric architecture design are only valid for a battery supplied architecture. It has to be validated if these trends and mass ranges can be transferred to serial-hybrid electric or turbo-electric architectures, where a gas turbine is generating the main or even entire fraction of the electric power.

5.4.2 Discussion of Hybrid-Electric Aircraft

As presented in Section 2.1, there are various options to integrate a hybrid-electric power train in an aircraft context for different possible application cases. In this thesis, the focus was set on the DPH topology that allows for an increase of the overall power train efficiency without lowering the effective inner efficiency of the gas turbines due to additional conversion losses (compared to serial or turbo-electric power trains). Furthermore, this topology was chosen to use the electric power train as an assistance system to potentially downsize the gas turbine. This topology was in detail investigated by Pornet and Isikveren [21] at the aircraft level using an integrated aircraft performance simulation tool. For the purpose of this thesis, the assessment at the aircraft level was performed with the help of trade factors synthesized with the same performance simulation tool and the parameters provided by Pornet [19, 21]. This approach was based on a two-engined reference aircraft in the class of an A320 and does not account for the drag of the additional, installed nacelles of the EDFs. For that purpose, Figure 5.25 covers the impact of an aerodynamic change on the overall aircraft performance, especially on the MTOW and the required energy demand. The nacelles account approximately for 15% of the total drag [134]. Assuming, in the first instance, that the nacelle drag of the EDFs is linearly increasing with the H$_P$, the additional nacelle drag would decrease the overall lift-to-drag ratio by about 3.0%. This increased drag results in a MTOW increase of around 0.7% and an additional required overall energy demand of 3.4%.

The impact of the electric system architecture mass and efficiency at the overall aircraft level is shown in Figure 5.26. This study was performed for motor sizing Scenario No.3 at the reference H_P and hybridization strategy EDF_{max}. The change of the EDF system efficiency influences the overall aircraft mass by an order of magnitude higher than the EDF system mass change. It includes the masses of the ducted fan, the gear box system and the electric power distribution system without batteries. This effect is mainly driven by virtue of the battery supplied architecture because the efficiency does not only affect the required battery capacity and in turn battery mass, but also the single components in the electric chain that need to be sized accordingly and also influence the required cooling system. This efficiency impact can be also transferred to the entire EDF supply chain. An efficiency increase may be performed by changing the initial design pressure ratio from around 1.4 to 1.18. According to Figure 4.4, this would lead to an increase of the propulsive efficiency by 4.4%. However, this design change would also increase the EDF mass by around 25%. Nevertheless, based on the sensitivity study, this would still reduce the required energy demand by around 2% not considering the smaller sized electric system architecture. This architecture could partly compensate the increased EDF mass, and a potential higher nacelle drag caused by the bigger fan diameter for low fan pressure ratios.

The overall aircraft level assessment further indicates that the fuel demand and the TSPC is decreasing with increasing values of H_P at the considered mission range. However, the required mission energy and, in turn, the equivalent CO_2 are also increasing. This leads for this type of aircraft configuration to an optimum hybrid-electric architecture at H_P of 0% and is equal to a conventional kerosene powered aircraft. Another possibility to influence the energy demand of the aircraft is achieved with the choice of the optimal hybridization

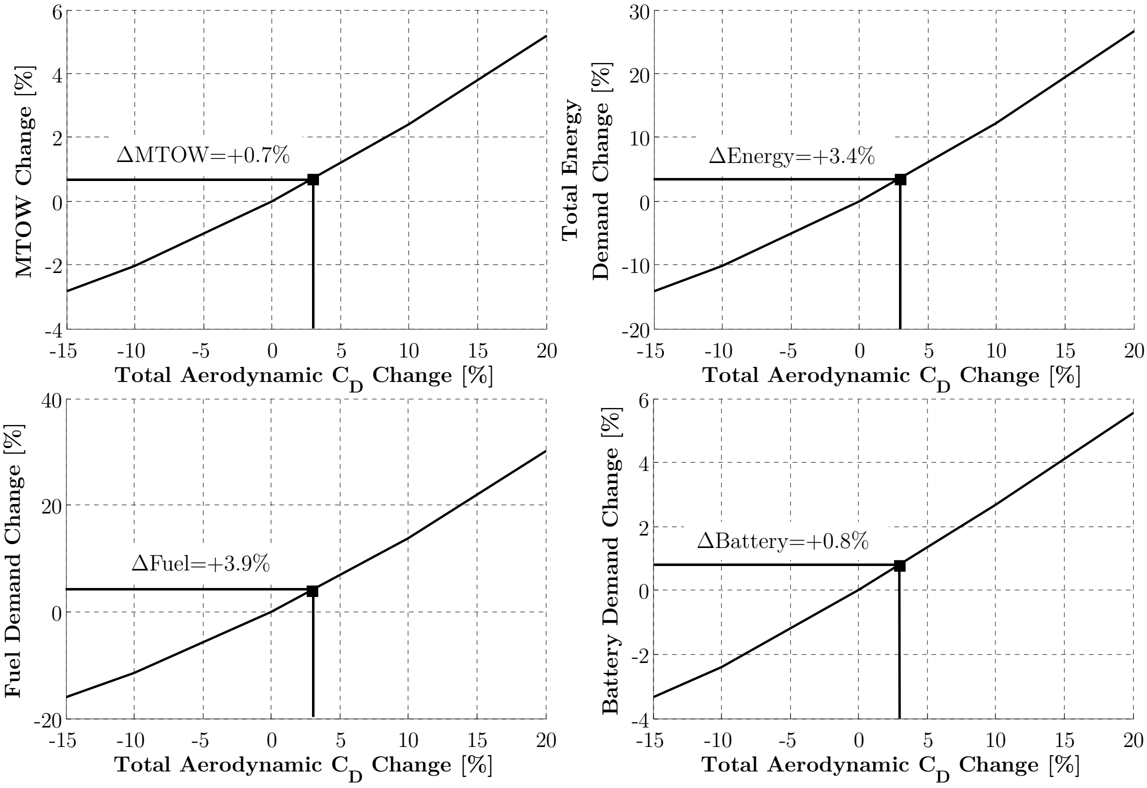

Figure 5.25: Impact of an aerodynamic drag change on the MTOW and the required energy demand (including fuel and battery) during the design mission for a H_P of 20% and the hybridization strategy EDF_{max}

strategy. It could be shown that depending on the objective, such as minimum CO_2 generation or minimum energy demand, different hybridization strategies are the optimum. When focusing on a minimum CO_2 generation, the best hybridization strategy is to operate the gas turbines in their optimum SFC point. However, this outcome is depending on the assumption of the electric energy mix. Assuming a full renewable electric energy production the best hybridization strategy is offered by the EDF_{max} case, where the electric system is always operating with its maximum power. This operation mode has the disadvantage that the MTOW is significantly increasing and has a negative impact on the cash operating costs. Nevertheless, the same effect can be also achieved using renewable drop-in fuels produced out of biomass [5] or even solar energy [135]. In this case, the original reference aircraft can be used without influencing any infrastructure on ground. From this perspective, a pure hybridization on power train level for a DPH aircraft is not a potential solution to fulfill the emission targets set by SRIA or NASA. This requires further improvements at the overall aircraft level, where one option could be to use the flexibility of such new power trains to enable synergies concerning airframe integration. This optimized integration can help to improve for example the aerodynamic or even structural efficiency. Such approaches are currently under investigation to efficiently enable technologies such as boundary layer ingestion. These technologies have the potential to significantly influence the aerodynamic efficiency and decrease

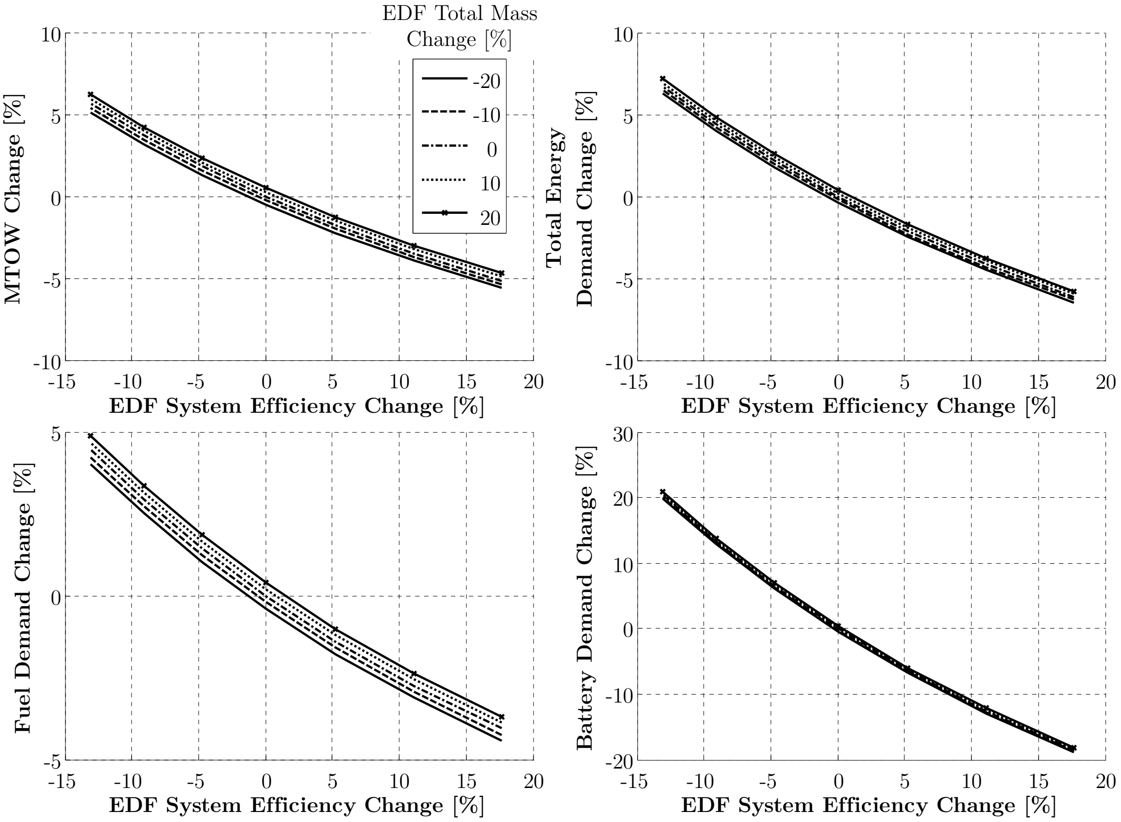

Figure 5.26: Performance of the electric system architecture during design mission for a H_P of 20% and the hybridization strategy EDF_{max}

therefore the overall mission energy. Another possibility could be to use the DPH topology to power a propulsive fuselage [41]. This concept represents an additional fan mounted at the rear of the fuselage to perform a boundary layer ingestion of the fuselage wake to reduce the zero lift drag. It could combine the advantages of the reduced aerodynamic drag and the increased transmission efficiency of the battery system. This propulsive fuselage concept has been already investigated with a partial turbo-electric topology in the EU funded project DisPURSAL [41] for long range application and for short range application by the NASA with the STARC-ABL concept [40].

6 Conclusion and Outlook

The following section summarizes the achieved results of this thesis and provides an outlook of open points concerning electric architecture designs for hybrid-electric and even universally-electric aircraft.

6.1 Summary of Findings and Results

With this thesis an important gap could be closed of battery supplied electric power architecture sizing for hybrid-electric aircraft (Table 6.1).

Table 6.1: Provided knowledge to close the gap in methods concerning electric systems architectures used for potential future power trains

Sizing Method	**Component Power Estimation**	**Component Mass Estimation**	**Thermal Management Aspects**	**Electric Off-Design Performance**	**Voltage Impact**	**Coupled Propulsor-Motor**	**Battery Supplied Architecture**	**Architecture Sizing Scenarios**	**Sensitivities at Aircraft Level**	**Source**
UEA	3	3	1	1	1	0	3	3	3	Stückl [18]
UEA	1	1	1	1	1	1	3	3	1	Vratny [52]
MIPH	1	1	0	1	0	1	1	0	3	Schmitz [39]
DPH	3	3	1	**3**	**3**	**3**	**3**	3	1	Current thesis

0 ... not covered, 1 ... partially covered, 3 ... fully covered
grey area marks closed gap

With the developed methods, the impact of the system mass and design efficiency at the overall electric power train level can be calculated for a required power, rotational speed demand and a specific design system voltage. Furthermore, the method allows for the generation of an electric architecture off-design performance map usable for mission simulation at aircraft conceptual design level. This capability was identified as a crucial open point during literature survey. The conceptual design methods cover the sensitivities of different rotational speeds, shaft power demands and system voltages including initial power requirements of the thermal management system. Moreover, the sizing approach, using batteries as main power supply, considers the impact of several component technologies such as conventional conducting, High Temperature Superconducting (HTS) or different semi-conductor materials. Different architecture combinations have been investigated, such as variable voltage or constant voltage systems. For battery supplied architectures, it was identified that full HTS electric motors offer the best performance with regard to mass and efficiency including the required cooling system. From an architectural point of view, a variable voltage architecture seems to be an optimal design option for battery supplied architectures where the changing battery output voltage is not stabilized by a converter. The system voltage was identified for all architecture optima near the operating voltage of the electric motor. A main conclusion out of this approach was that a higher transmission voltage does not automatically offer the lightest and most efficient electric power train system. With these system parameters, the overall electric systems efficiency for different design shaft powers was identified between 96.4% and 96.7%. The corresponding specific power varies between 2 kW/kg and 7 kW/kg depending on the design rotational speed of the electric motor. Due to the relative small design corridor of the electric systems efficiency, the pure electric system architecture should be designed mass optimized. An initial transition point concerning the change of a conventional conducting system to a HTS system has been identified at 7000 kW motor shaft power. However, considering also additionally required coupling systems between non-cryogenic and superconducting system, this break-even point may shift to higher power demands. It could be also identified that the optimal system voltage of the electric power architecture is a function of the motor design voltage, power and the cable length. For the considered design space with a cable length of around 40 m, the optimum system voltage has been found at 2000 V driven by the electric motor voltage.

Besides the investigations performed at the electric system architecture level, also different design options with an Electric Ducted Fan (EDF) in combination with a gas turbine have been investigated. As baseline architecture a Discrete Parallel Hybrid (DPH) power train was investigated where the electric power train was used as an assistance system. For this concept no synergy effects with regard to aerodynamics were considered. The studies performed at the EDF system level covered different design options such as direct drive, geared system and different motor sizing points. At the system level, it could be shown that a geared drive train offers the lightest system, while a direct drive system provides the highest efficiency with regard to Thrust Specific Power Consumption (TSPC). The TSPC is defined as the ratio of the supplied power per delivered thrust. Depending on the design gear ratio, the direct drive system can be nearly 1% better than the geared version, but would be also more than 10% heavier including the electric system with low rotational speed electric motors. Focusing on the motor sizing options of the electric power train system, different sizing scenarios were considered. The sizing points were defined at Top of Climb (TOC), the design point of the

EDF, at Take-Off (TO), where the maximum fan power occurs and at TO at equivalent TOC power. Using the electric power train as an assistance system for a gas turbine, the motor power rating can be used in a way that it allows for an optimal utilization of the electric system architecture. For a solely battery powered aircraft, the sizing point of the electric motor is already implicitly defined at TO conditions, as the required thrust has to be delivered in this flight state to fulfil the aircraft top level requirements. For the assistance system, where the gas turbine can be sized in a way to compensate the delta thrust, the optimal motor sizing point has been identified for TO conditions at equivalent TOC power. This sizing point ends up in a higher electric system mass compared to a pure TOC condition sizing of about 3.3%, but allows for a full usage of the electric system in all critical flight phases, where otherwise a maximum torque limitation of the electric motor would occur. The motor sizing option during TO condition was identified as a non-optimal design point, as it features twice the mass of the optimum solution with regard to power demand. This power demand is only required for a short period of the mission. From an efficiency point of view, the different sizing scenarios are in an equal range. This confirms the assumption that the focus should be set on a mass optimized electric system.

The different motor sizing options have been also investigated for different degrees of power hybridization, H_P, values in a range between 0%, covering the conventional reference aircraft, and 45% on the system and the aircraft level. Depending on the thrust split between the gas turbine and the EDF it could be identified that for different values of H_P different critical sizing cases for the hybrid-electric power train occurs. For values of H_P lower than 35%, the one-engine inoperative case is the sizing scenario for the gas turbine, while for higher values of H_P the all-engine operative case gets design driving. This trend is also valid at the overall aircraft level. At the aircraft level four different mission hybridization strategies were analyzed for a specific DPH design point. These mission hybridization strategies cover different operational modes of the DPH power trains, such as operating the GTF in their optimal SFC point in all mission points, running the electric system in all flight phases in the maximum rated power or operating the GTFs always in their maximum rated thrust. This assessment had shown that with increasing values of design H_P the maximum take-off weight (MTOW) is increasing for all mission hybridization strategies. The in-flight fuel burn is decreasing, except for the hybridization strategy where the GTFs are running with their maximum rated thrust. This strategy causes a higher fuel burn compared to the reference for design values of H_P lower than 40%. The highest fuel and CO_2 reduction potential of about 15% is achieved by the strategy, where the EDFs are running in their maximum power. However, considering also the production chain of both energy carriers, kerosene and electric energy, the equivalent CO_2 is increasing with increasing H_P. Therefore, using the equivalent CO_2 as main figure of merit ends up with an optimal hybrid-electric aircraft configuration at H_P of 0% representing the conventional powered aircraft. Only when assuming a full renewable and CO_2-free electric energy production, the hybrid-electric power train is providing a CO_2 reduction potential of 15% where the EDFs are operated with their maximum rated power in all flight phases. Nevertheless, this option would cause the heaviest aircraft with regard to MTOW. A suitable trade-off between CO_2 reduction potential and MTOW increase was identified at a design value of H_P of 20% with 8.9% CO_2 reduction potential at 31.6% MTOW increase. This reduction potential is not sufficient to fulfill the ambitious environmental reduction targets set by the European Union or the National Aeronautics Space Administration.

A main conclusion that can be drawn out of the evaluated results is that a hybridization on pure power train level does not offer a potential solution with regard to mission energy reduction at the overall aircraft level, although the inner efficiency of the propulsion system can be increased. The big challenge is, as already shown in several studies, the mass penalty caused by the battery system, notwithstanding the fact that already an advanced battery technology has been assumed with a specific energy of 1000 Wh/kg for the performed studies.

6.2 Further Work

The presented modeling approach including the sensitivity studies performed at the system and the aircraft level are only representing battery supplied architectures. For that purpose, electric component models and architecture sizing approaches have been developed to investigate basic sensitivities for mass and (off-design) efficiencies at a conceptual level. The level of detail of the component models should be extended in some cases such as for the battery, electric motor and protection devices. The battery model is only representing one potential generic discharge curve for a lithium based battery cell. Depending on the electric chemistry the discharge behavior of other types of cells can be completely different and it has to be investigated, how this change in discharge behavior is influencing the overall architecture design and performance. This also includes alternative electric energy sources such as fuel cell systems, super capacitors, generators or even a combination out of these sources for different power classes. Another open point is the sizing of the thermal management system. Within this thesis a constant temperature has been assumed for all electric components during the entire design mission. This simplification does not account for altitude effects such as decreasing outside temperature levels and air densities during the mission segments where possibly also component heating can get an issue. Nevertheless, for high power applications a further question mark is how the generated heat can be effectively transferred to the surrounding air for different flight states and if this scenario case has also a sizing impact.

The methods developed to design and size the DC architectures are based on a morphological box to identify suitable component combinations for different power levels. To increase the optimization capability of such architectures more sophisticated optimization routines could be used such as Particle Swarm Optimization or Genetic Algorithms as highlighted by Silvas et al. [22]. Furthermore, these optimization routines can be used to improve the sizing approach to consider more types of failure cases. The presented sizing approach of the architectures only includes initial estimations of potential failure cases. This approach should be extended to cover several emergency power demands for different flight states and, in a first instance, evaluate for each inoperative component the resulting power demand or change, if required, the design point of the most critical component. However, a more sophisticated fault analysis would need more detailed requirements from the aircraft to assess precisely the impact of certain failure cases at the overall aircraft level. As a next step the developed architecture designs have to be integrated in a multi-disciplinary overall aircraft design loop, where the interactions between the other disciplines such as aerodynamics or center of gravity shifts can be better evaluated. The presented approach using trade factors is only suitable, if a quick assessment of trends of electric power architecture options should be performed. In the same turn, it has to be investigated if there are sweet spots for certain design ranges and payload requirements where a specific electric power train gets more interesting than other ones. For that purpose also different component technologies should be considered to identify if particular technologies become more advantageous at specific power levels. For example, in the present study a potential change in component technology from normal conducting to cryogenic conducting has been identified at 7000 kW.

Bibliography

[1] IATA. Air Passenger Forecasts. Technical report, IATA, Geneva, 2015.

[2] Airbus. *Growing Horizons 2017/2036.* Art & Caractère, 2017.

[3] Boeing. Current Market Outlook 2016-2035. Technical report, Boeing, Seattle, 2016.

[4] European Commission. *EU Transport in Figures.* Publications Office of the European Union, Bietlot, Belgium, 2016.

[5] Advisory Council of Aviation Research and Innovation in Europe. Vision 2020 ACARE. Technical report, ACARE, London, 2010.

[6] Pratt & Whitney. PurePower Engine Family Specs Chart. Technical report, Report S16309.B-06.12, 2012.

[7] Aviation Partners Inc. Aviation Partners Launches Split Scimitar^{TM} Winglets for BBJs. Technical report, Aviation Partners, Inc., Las Vegas, 2013.

[8] M. D. Moore and B. Fredericks. Misconceptions of Electric Aircraft and their Emerging Aviation Markets. *52nd Aerospace Sciences Meeting*, (January):1–17, 2014.

[9] S. Carnot. *Reflections on the Motive Power of Heat and on Machines Fitted to Develop That Power.* John Wiley & Sons, Hoboken, New York, USA, 2nd edition edition, 1897.

[10] J. Sieber. European Technology Programs for Eco-Efficient Ducted Turbofans. In *ISABE 2015*, Phoenix, Arizona, 2015. ISABE.

[11] J. Bijewitz, A. Seitz, and M. Hornung. Architectural Comparison of Advanced Ultra-High Bypass Ratio Turbofans for Medium to Long Range Application. In *Deutscher Luft- und Raumfahrt Kongress 2014*, Augsburg, Germany, 2014. DocumentID: 340105.

[12] S. Kaiser, S. Donnerhack, A. Lundbladh, and A. Seitz. A Composite Cycle Engine Concept with Hecto-Pressure Ratio. In *51st AIAA/SAE/ASEE Joint Propulsion Conference*, Orlando, 2015.

[13] A. Seitz, O. Schmitz, A. T. Isikveren, and M. Hornung. Electrically Powered Propulsion: Comparison and Contrast to Gas Turbines. In *Deutscher Luft- und Raumfahrt Kongress 2012*, Berlin, Germany, 2012.

[14] E. Torenbeek. *Synthesis of Subsonic Airplane Design: An Introduction to the Preliminary Design of Subsonic General Aviation and Transport Aircraft, with Emphasis on Layout, Aerodynamic Design, Propulsion and Performance.* Delft University Press, Delft, The Netherlands, 1996.

[15] I. Cotton, A. Nelms, and M. Husband. Higher Voltage Aircraft Power Systems. *IEEE A&E Systems Magazine*, (February), 2008.

[16] D. P. Raymer. *Aircraft Design: A Conceptual Approach.* American Institute of Aeronautics and Astronautics, Reston, Virginia, 3 edition, 1999.

[17] S. Stückl, J. van Toor, and H. Lobentanzer. VOLTAIR - The All Electric Propulsion Concept Platform - A Vision For Atmospheric Friendly Flight. In *28th International Congress Of The Aeronautical Sciences*, pages ICAS 2012–4.7.2, Brisbane, 2012.

[18] S. Stückl. *Methods for the Design and Evaluation of Future Aircraft Concepts Utilizing Electric Propulsion Systems.* PhD thesis, Technical University of Munich, 2016.

[19] C. Pornet, C. Gologan, P. C. Vratny, A. Seitz, O. Schmitz, A. T. Isikveren, and M. Hornung. Methodology for Sizing and Performance Assessment of Hybrid Energy Aircraft. *Journal of Aircraft*, 52(1):341–352, 2014.

[20] C. Pornet, S. Kaiser, A. T. Isikveren, and M. Hornung. Integrated Fuel-Battery Hybrid for a Narrow-Body Sized Transport Aircraft. *Aircraft Engineering and Aerospace Technology Journal*, 86(5), 2014.

[21] C. Pornet and A. T. Isikveren. Progress in Aerospace Sciences Conceptual Design of Hybrid-Electric Transport Aircraft. *Progress in Aerospace Sciences*, 79:114–135, 2015.

[22] E. Silvas, T. Hofman, and M. Steinbuch. Review of Optimal Design Strategies for Hybrid Electric Vehicles. *2012 Workshop on Engine and Powertrain Control*, pages 57–64, 2012.

[23] Innovation und Technologie Bundesministerium für Verkehr. Austrian Technological Expertise in Transport - Focusing on: Hybrid and Electric Vehicles. Technical report, Austrian Federal Ministry for Transport, Innovation and Technology - BMVIT, Vienna, 2008.

[24] L. Lorenz, A. Seitz, H. Kuhn, and A. Sizmann. Hybrid Power Trains for Future Mobility. In *62. Deutscher Luft- und Raumfahrt Kongress 2013*, Stuttgart, Germany, 2013.

[25] J. E. Rucker. Design and Analysis of a Permanent Magnet Generator for Naval Applications. *Massachusetts Institute of Technology*, 2005.

[26] N. Doerry, H. Robey, J. Amy, and C. Petry. Powering the Future with the Integrated Power System. *Naval Engineers Journal*, 108(3):267–279, 1996.

[27] M. Sinnet. 787 No-Bleed Systems: Saving Fuel and Enhancing Operational Efficiency, 2007.

[28] L. Faleiro. Beyond the More Electric Aircraft. *Aerospace*, 44(September 2005):35–40, 2006.

[29] X. Xia. *Dynamic Power Distribution Management for All Electric Aircraft.* PhD thesis, Cranfield University, 2011.

[30] R. Moulton. An Electric Aeroplane. *Flight International*, page 946, 1973.

[31] T. Tomazic, V. Plevnik, G. Veble, J. Tomazic, F. Popit, S. Kolar, R. Kikelj, J. W. Langelaan, and K. Miles. Pipistrel Taurus G4: On Creation and Evolution of the Winning Aeroplane of NASA Green Flight Challenge 2011. *Strojniski Vestnik/Journal of Mechanical Engineering*, 57(12):869–878, 2011.

[32] PC-Aero GmbH. Elektra One - PC-Aero, 2017.

[33] Airbus. Vollelektrisches Flugzeug E-Fan erhält höchste Auszeichnung des Magazins "Popular Science". Technical report, Airbus, Toulouse, 2014.

[34] Siemens AG. Elektromotor stellt zweifachen Geschwindigkeitsrekord auf. Technical report, Siemens AG, Munich, 2017.

[35] A. T. Isikveren, A. Seitz, P. C. Vratny, C. Pornet, K. O. Plötner, and M. Hornung. Conceptual Studies of Universally-Electric Systems Architectures Suitable for Transport Aircraft. In *Deutscher Luft- und Raumfahrt Kongress 2012, Berlin, Germany*, Berlin, Germany, 2012.

[36] M. K. Bradley and C. K Droney. Subsonic Ultra Green Aircraft Research: Phase I Final Report. Technical Report April, NASA, Huntington Beach, California, 2011.

[37] M. J. Armstrong, M. Blackwelder, A. Bollman, C. Ross, A. Campbell, C. Jones, and P. Norman. Architecture, Voltage and Components for a Turboelectric Distributed Propulsion Electric Grid. Technical Report July, National Aeronautics and Space Administration, NASA/CR-2015-218440, 2015.

[38] European Union. Directive 2007/46/EC of the European Parlament and of the Council of 5 September 2007 establishing a framework for the approval of motor vehicles and their trailers, and of systems, components and separate technical units intended for such vehicles. Technical report, 2007.

[39] O. Schmitz. *Methodical Assessment of Electric Propulsion Systems for Transport Category Aircraft.* PhD thesis, Technical University of Munich, 2016.

[40] J. S. Gray, C. A. Mader, G. K. Kenway, and J. Martins. Approach to Modeling Boundary Layer Ingestion using a Fully Coupled Propulsion-RANS Model. *58th AIAA/ASCE/AHS/ASC Structures, Structural Dynamics, and Materials Conference*, 2017.

[41] A. T. Isikveren, A. Seitz, J. Bijewitz, A. Mirzoyan, A. Isyanov, R. Grenon, O. Atinault, J. L. Godard, and S. Stückl. Distributed Propulsion and Ultra-High By-Pass Rotor Study at Aircraft Level. *Aeronautical Journal*, 119(1221):1327–1376, 2015.

[42] O. Schmitz. Fahrzeugtriebwerk, Fahrzeug mit diesem Fahrzeugtriebwerk und Verfahren zum Betrieb dieses Fahrzeugtriebswerkes, 2012.

[43] P. C. Vratny, S. Kaiser, A. Seitz, and S. Donnerhack. Performance Investigation of Cycle-Integrated Parallel Hybrid Turboshafts. *Journal of Engineering for Gas Turbines and Power*, 139(March):031201–1 – 031201–9, 2017.

[44] A. T. Isikveren, C. Pornet, P. C. Vratny, and M. Schmidt. Conceptual Studies of Future Hybrid-Electric Regional Aircraft. In ISABE, editor, *ISABE 2015*, pages ISABE – 21 5 – 20285, 2015.

[45] O. Schmitz and M. Hornung. Simulation and Analysis of Hybrid Energy Propulsion. In *Deutscher Luft- und Raumfahrt Kongress 2013*, Stuttgart, Germany, 2013.

[46] G. V. Brown. Weights and Efficiencies of Electric Components of a Turboelectric Aircraft Propulsion System. In *49th AIAA Aerospace Sciences Meeting including the New Horizons Forum and Aerospace Exposition*, Orlando, Florida, 2011.

[47] B. A. Skinner, G. T. Parks, and P. R. Palmer. Comparison of Submarine Drive Topologies Using Multiobjective Genetic Algorithms. *IEEE Transactions on Vehicular Technology*, 58(1):57–68, 2009.

[48] M. Hepperle. Electric Flight-Potential and Limitations. In *AVT-209 Workshop*, Lisbon, 2012.

[49] J. Van Bogaert. *Assessment of Potential Fuel Saving Benefits of Hybrid-Electric Regional Aircraft.* PhD thesis, Delft University of Technology, 2015.

[50] J. Bonni, B. Burghoff, E. Dinçer, J. Felix, L. Eichler, T. Ferguson, H. Mirza, M. Nuno, M. Y. Pereda, and M. Valley. Conceptual Design of a Low Noise Hybrid Passenger Aircraft. Technical report, RWTH Aachen, Aachen, Germany, 2017.

[51] C. Perullo, D. Trawick, M. Armstrong, J. C. Tai, and D. N. Mavris. Cycle Selection and Sizing of a Single-Aisle Transport with the Electrically Variable Engine(TM) (EVE) for Fleet Level Fuel Optimization. In *55th AIAA Aerospace Sciences Meeting*, number January, Grapevine, Texas, 2017.

[52] P. C. Vratny. *A Battery Powered Transport Aircraft.* AV Akademikerverlag GmbH & Co. KG, Saarbrücken, 2012.

[53] A. Seitz, M. Nickl, A. C. Stroh, and P. C. Vratny. Conceptual Study of a Mechanically Integrated Parallel-Hybrid Electric Turbofan. In *7th EASN International Conference*, Warsaw, 2017.

[54] A. Ang, A. Gangoli Rao, T. Kanakis, and W. Lammen. Performance analysis of an electrically assisted propulsion system for a short-range civil aircraft. *Journal of Aerospace Engineering*, 0(0):1–13, 2018.

[55] GasTurb GmbH. GasTurb 12. Aachen, Germany, 2015.

[56] European Aviation Safety Agency. CS-25: Certification Specifications and Acceptable Means of Compliance for Large Aeroplanes. *Amendment 12*, (September), 2012.

[57] Federal Aviation Administration. Part 25-Airworthiness Standards: Transport Category Airplane, 2016.

[58] P. C. Vratny, H. Kuhn, and M. Hornung. Influences of Voltage Variations on Electric Power Architectures for Hybrid Energy Aircraft. *CEAS Aeronautical Journal*, 8(1):31–43, 2017.

[59] OMG. OMG Unified Modeling Language (OMG UML), Superstructure, V2.1.2. Technical Report November, Object Management Group, Inc. (OMG), OMG Document Number: formal/2007-11-01, 2007.

[60] J. B. Heywood, M. A. Weiss, A. Schafer, S. A. Bassene, and V. K. Natarajan. The Performance of Future ICE and Fuel Cell Powered Vehicles and Their Potential Fleet Impact. Technical report, Massachusetts Institute of Technology, Cambridge, MA, USA, 2004.

[61] L. Riascos and D. D. Pereira. Controlling Operating Temperature in PEM Fuel Cells. *ABCM Symposium Series in Mechatronics*, 4:137–146, 2010.

[62] S. Klink. *In-Depth Analysis of Irreversible Processes in Lithium Ion Batteries.* PhD thesis, Ruhr-Universität Bochum, 2013.

[63] C. Julien, A. Mauger, A. Vijh, and K. Zaghib. Lithium Batteries. In *Lithium Batteries*, chapter 2, pages 29–68. Springer, Cham, 2016.

[64] D. Linden and T. B. Reddy. *Handbook of Batteries.* McGraw-Hil, New York, USA, 3rd edition, 2002.

[65] I. Moir and A. Seabridge. *Aircraft Systems: Mechanical, Electrical, and Avionics Subsystems Integration-Third Edition.* West Sussex: John Wely & Sons, 2008.

[66] P. Vandenbossche, F. Vergels, J. Vanmierlo, J. Matheys, and W. Vanautenboer. SUBAT: An Assessment of Sustainable Battery Technology. *Journal of Power Sources*, 162(2):913–919, nov 2006.

[67] O. Erdinc, B. Vural, and M. Uzunoglu. A Dynamic Lithium-Ion Battery Model Considering the Effects of Temperature and Capacity Fading. *2009 International Conference on Clean Electrical Power*, pages 383–386, June 2009.

[68] H. Fisk and J. Leijgård. *A Battery Management Unit.* PhD thesis, Chalmers University, 2010.

[69] P. C. Vratny, C. Gologan, C. Pornet, A. T. Isikveren, and M. Hornung. Battery Pack Modeling Methods for Universally-Electric Aircraft. In *CEAS 2013*, pages 525–535, Linköping, Sweden, 2013.

[70] M. Chen and G. A. Rincon-Mora. Accurate Electrical Battery Model Capable of Predicting Runtime and I-V Performance. *IEEE Transactions on Energy Conversion*, 21(2):504–511, June 2006.

[71] H. Kuhn and A. Sizmann. Fundamental Prerequisites for Electric Flying. In *Deutscher Luft- und Raumfahrt Kongress 2012*, Berlin, 2012.

[72] P. C. Vratny, P. Forsbach, A. Seitz, and M. Hornung. Investigation of Universally Electric Propulsion Systems for Transport Aircraft. In *ICAS 2014*, St. Petersburg, Russia, 2014.

[73] M. Drela. First-Order DC Electric Motor Model. Technical report, MIT Aero & Astro, 2007.

[74] H. Neudorfer. *Weiterentwicklung von elektrischen Antriebssystemen für Elektro- und Hybridstraßenfahrzeuge.* Österreichischer Verband für Elektrotechnik, Vienna, 2 edition, 2008.

[75] H. K. Patel, R. Nagarsheth, and S. Parnerkar. Performance Comparison of Permanent Magnet Synchronous Motor and Induction Motor for Cooling Tower Application. *International Journal of Emerging Technology and Advanced Engineering*, 2(8):167–171, 2012.

[76] U. Vollmer and U. Schäfer. An At-All Operating Points Highly Efficient PMSM for HEV. *World Electric Vehicle Journal*, 2(4):99–107, 2008.

[77] A. Shahat El, A. Keyhani, and H. Shewy El. Sizing a High Speed PM Generator for Green Energy Applications. *Journal of Electrical Systems*, 6(4):501–516, 2010.

[78] S. S. Kalsi. *Applications of Hight Temperature Superconductors to Electric Power Equipment.* John Wiley & Sons, Inc., New Jersey, 2011.

[79] P. Barnes, M. Sumption, and G. Rhoads. Review of High Power Density Superconducting Generators: Present State and Prospects for Incorporating YBCO Windings. *Cryogenics*, 45(10-11):670–686, oct 2005.

[80] A. V. Fernández. *Reliability of the Quench Protection System for the LHC Superconducting Elements.* PhD thesis, Universitat Politècnica de Catalunya, 2003.

[81] K. Sivasubramaniam, T. Zhang, M. Lokhandwalla, E.T. Laskaris, J.W. Bray, B. Gerstler, M.R. Shah, and J.P. Alexander. Development of a High Speed HTS Generator for Airborne Applications. *IEEE Transactions On Applied Superconductivity*, 19(3):1656–1661, 2009.

[82] C. A. Luongo, P. J. Masson, T. Nam, D. Mavris, H. D. Kim, G. V. Brown, M. Waters, and D. Hall. Next Generation More-Electric Aircraft: A Potential Application for HTS Superconductors. *IEEE Transactions on Applied Superconductivity*, 19(3):1055–1068, jun 2009.

[83] J. Pyrhönen, T. Jokinen, and V. Hrabovocá. *Design of Rotating Electrical Machines*. John Wiley & Sons, Ltd., Chichester, United Kingdom, 2008.

[84] M. D. Bogomolov. Concept Study of 20 MW High-Speed Permanent Magnet Synchronous Motor for Marine Propulsion. Technical report, Eindhoven University of Technology, Eindhoven, 2013.

[85] M. Lokhandwalla, K. S. Haran, and J. P. Alexander. Scaling Studies of High Speed High Temperature Superconducting Generator. *2012 XXth International Conference on Electrical Machines*, pages 751–756, sep 2012.

[86] A. Mahmoudi, N. A. Rahim, and W. P. Hew. Axial-Flux Permanent-Magnet Machine Modeling, Design, Simulation and Analysis. *Scientific Research and Essays*, 6(12):2525–2549, 2011.

[87] R. Grune. *Verlustoptimaler Betrieb einer elektrisch erregten Synchronmaschine für den Einsatz in Elektrofahrzeugen*. PhD thesis, University Berlin, 2012.

[88] K. Haran. High Power Density Superconducting Machines for Electric / Hybrid Electric Airplanes. In *Bauhaus Luftfahrt Symposium 2015*, Taufkirchen, Germany, 2015.

[89] A. Wintrich, U. Nicolai, W. Tursky, and T. Reimann. *Application Manual Power Semiconductors*. ISLE Verlag, Ilmenau, Germany, 2011.

[90] SEMIKRON. *SemiSel 4.1*. SEMIKRON International GmbH, Nuremberg, 2014.

[91] T. Mathe and N. Raju. Comparitive Loss Evaluation of Si IGBT Versus Sic MOSFET (Silicon Carbide) for 3 Phase SPWM Inverter. *Indian Journal of Science and Technology*, 8(28), 2015.

[92] X. Fonteneau and L. Pinson. Power Converter with Built in Silicon Carbide Technology. In *Submarine Institute of Australia Science, Technology & Engineering Conference 2015*, Adelaide, Australia, 2015.

[93] J. Fedison. SiC-based MOSFETs Offer Dramatic Benefits in Automotive, Power Applications, 2016.

[94] S. Roberts. DC/DC Book of Knowledge. Technical report, RECOM Engineering GmbH & Co KG, Gmunden, 2014.

[95] H. Fan. Design Tips for an Efficient Non-Inverting Buck-Boost Converter. *Analog Applications Journal*, 3Q:1–4, 2014.

[96] D. Schelle and J. Castorena. Buck-Converter Design Demystified. *Power Electronics Technology*, (June):46–53, 2006.

[97] J. Ejury. Buck Converter Design. Technical report, Infineon, Infineon Design Note DN 2013-01, 2013.

[98] B. Hauke. Basic Calculation of a Boost Converter's Power Stage. Technical report, Texas Instruments Incorporated, Application Report SLVA372C, 2014.

[99] S. Crump. TPA2013D1 Boost Converter Component Selection. Technical report, Texas Instruments, Annual Report SLOA127, 2009.

[100] F. J. Bryan and A. J. Forsyth. A Power Dense DC-DC Converter for a Small Electric Vehicle. In *6th IET International Conference on Power Electronics, Machines and Drives (PEMD 2012)*, Bristol, UK, 2012.

[101] G. Dvorský. HBC - SERIES V7 300400-3, 400400-3. Technical report, MGM-Compro, Zlin, Czech Republic.

[102] S. Matlok. Bidirectional full SiC 200 kW DC-DC Converter for Electric, Hybrid and Fuel Cell Vehicles. Technical report, Fraunhofer Institute for Integrated Systems and Device Technology IISB, Erlangen, 2015.

[103] F. Sargos. IGBT Power Electronics Teaching System Principle for Sizing Power Converters. Technical report, Semikron, 2008.

[104] M. Mohr and F. W. Fuchs. Comparison of Three Phase Current Source Inverters and Voltage Source Inverters Linked with DC to DC Boost Converters for Fuel Cell Generation Systems. *European Conference on Power Electronics and Applications*, page 10, 2005.

[105] Infineon Technologies AG. Technical Information for Bipolar Semiconductors. Technical report, Infineon Technologies Bipolar GmbH & Co. KG, Warstein, 2012.

[106] S. Fletcher. *Protection of Physically Compact Multiterminal DC Power Systems*. PhD thesis, University of Strathclyde, 2013.

[107] C. E. Restrepo. Arc Fault Detection and Discimination Methods. In *the 53rd IEEE Holm Conference on Electrical Contacts - 2007*, Pittsburgh, 2007.

[108] Z. Liu. *Load Side Detection of Series Arcs in DC Microgrids by Simulation and Experimental Validation*. PhD thesis, Technical University of Delft, 2016.

[109] D. Chen and L. Xu. *AC and DC Microgrid with Distributed Energy Resources*. Springer International Publishing, Switzerland, 2017.

[110] B. Gunther. Evaluation of Battery and Battery Charger Short-Circuit Current Contributions to a Fault on the DC Distribution System at a Nuclear Power Plant. Technical report, Brookhaven National Laboratory, BNL-107800-2015-IR, New York, 2015.

[111] F. C. Cheng. Insulation Thickness Determination Of Polymeric Power Cables. *IEEE Transactions on Dielectrics and Electrical Insulation*, 1(4):624–629, 1994.

[112] D. R. Lide. *CRC Handbook of Chemistry and Physics, 84th Edition, 2003-2004*, volume 53. CRC Press, 84th edition, 2003.

[113] Borealis. HEP ODS Chooses for XLPE Insulation to Ensure Reliable Power Supply in Croatia. Technical report, Borealis AG, Vienna, 2014.

[114] Copper Development Association Inc. Recommended Practices for Designing and Installing Copper Building Wire Systems. Technical report, CWIS Committee, 2013.

[115] Y. Xi. Installation and Trial Operation of 35kV/121MVA HTS AC Power Cable. In *Symposium on HTS Cable Applications*, Kunming, China, 2004.

[116] J. McCall, B. Gamble, and S. Eckroad. Combining Superconductor Cables and VSC HVDC terminals for Long Distance Transmission. In *2010 IEEE Conference on Innovative Technologies for an Efficient and Reliable Electricity Supply (CITRES)*, pages 47–54, 2010.

[117] S. C. Mohapatra. An Overview of Liquid Coolants for Electronics Cooling. *Electronics Cooling*, 12(2):22–27, 2006.

[118] K.-E. Rydberg. *Energy Efficient Hydraulics - System Solutions for Loss Minimization.* National Conference on Fluid Power, Linköping, Sweden, 2015.

[119] D. Bharathan. Air Cooling Technology for Advanced Power Electronics and Electric Machines. Technical Report May, National Renewable Energy, 2009.

[120] Y. Fefermann, C. Maury, C. Level, K. Zarati, J. Salanne, C. Pornet, B. Thoraval, and A. T. Isikveren. Hybrid-Electric Motive Power Systems for Commuter Transport Applications. In *30th Congress of the International Council of the Aeronautical Sciences*, number September, Daejon, Korea, 2016.

[121] P. C. Vratny and M. Hornung. Sizing Considerations of an Electric Ducted Fan for Hybrid Energy Aircraft. In *Transportation Research Procedia*, volume 29, pages 410–426, 2018.

[122] J. Kurzke. GasTurb11, compiled with delphi 2007 on 27th January, 2010.

[123] Pace GmbH. PACE - Pacelab APD, 2011.

[124] H.-J. Steiner, P. C. Vratny, C. Gologan, K. Wieczorek, A. T. Isikveren, and M. Hornung. Optimum Number of Engines for Transport Aircraft Employing Electrically Powered Distributed Propulsion. *CEAS Aeronautical Journal*, jan 2014.

[125] A. Moreau, A.-L. Aulich, R. Jaron, H. Knobbe-Eschen, L. Enghardt, and E. Nicke. Optimization of Casing Contours in an Aero-Engine Fan Stage with Emphasis on Rotor-Stator Interaction Noise. In *International Symposium on Transport Phenomena and Dynamics of Rotating Machinery*, Honolulu, Hawaii, 2016.

[126] C. Reynolds. Advanced Propfan Engine Technology (APET) Single- and Counter-rotation Gearbox/Pitch Che Mechanism, Final Report. Technical report, NASA-CR-168114, Vol. 1 & 2, 1985.

[127] A. Stroh, G. Wortmann, and A. Seitz. Conceptual Sizing Methods For Power Gearboxes In Future Gas Turbine Engines. In *Deutscher Luft- und Raumfahrt Kongress 2017*, Munich, Germany, 2017.

[128] MathWorks. Matlab R2013b, 2013.

[129] C. Gologan. *A Method for the Comparison of Transport Aircraft with Blown Flaps.* PhD thesis, Technical University of Munich, 2010.

[130] LTH Koordinierungsstelle. Luftfahrttechnisches Handbuch, 2006.

[131] L. Miltner. *Environmental Life Cycle Assessment of Universally-Electric Powered Transport Aircraft.* PhD thesis, Karlsruhe Institute of Technology, 2016.

[132] S. I. Schlachter, W. Goldacker, B. Holzapfel, A. Kudymow, and H. Wu. DC-HTS Cables for Power Distribution in Hybrid-Electric Aircraft. In *Coated Conductors for Applications 2016*, Aspen, Colorado, USA, 2016.

[133] K. Allweins and E. Marzahn. Feasibility of HTS DC Cables on Board a Ship. In *10th EPRI Superconductivy Conference*. Nexans Deutschland GmbH, 2011.

[134] R. Halper, K. Lane, D. Marschik, D. Marschik, B. Morham, J. Pham, R. McDonald, and B. Wright. Conceptual Design of a Next Generation, 150 Passenger Commercial Transport. In *48th AIAA Aerospace Sciences Meeting Including the New Horizons Forum and Aerospace Exposition*, pages 2010–1396, Orlando, Florida, 2010.

[135] V. Batteiger, J. Bauldreay, C. Falter, P. Furler, H. Geerlings, P. Le Clercq, D. Marxer, P. Pandi, D. Reinalda, J. Scheffe, A. Sizmann, and A. Steinfeld. Progress and Perspectives of Solar Fuels. In *Aviation in Europe Innovating for growth : proceedings of the seventh European Aeronautics Days*, pages 167–173, London, 2015.

[136] A. Binder. Hochausgenutzte Permanentmagnet-Synchronmaschinen. In *Innovative elektrische Antriebe*, Vienna, Austria, 2008. OVE.

[137] S. K. Baik, Y. K. Kwon, H. M. Kim, S. H. Kim, J. D. Lee, Y. C. Kim, H. J. Park, W. S. Kwon, and G. S. Park. Electrical Parameter Evaluation of a 1MW HTS Motor via Analysis and Experiments. *Cryogenics*, 49(6):271–276, jun 2009.

A Motor Design Parameters

The following section summarizes the used parameters to design the conventional Permanent Magnet Synchronous Motor (PMSM), the partial HTS and the full HTS baseline motor.

Table A.1: Constant motor parameters used for all electric motor designs

Parameter	**Value**	**Parameter**	**Value**
Number of phases	3	Stator/Rotor density $[kg/m^3]$	7860 / 4800
Number of pole pairs p	1	Rotor Young's modulus E $[N/m^2]$	$210 \cdot 10^9$
Number of coils N	30	Rotor tensile strength $R_{p,0.2} [N/m^2]$	$250 \cdot 10^6$
Magnet angle [deg]	50	Stator yoke ratio $k_{Stator,Yoke}$ [-]	0.6
Mass service fraction k_{Serv}	0.13	Safety factor k_S	1.5
Diameter Ratio DR	0.5		

Table A.2: Constant motor parameters used for all electric motor designs

Parameter	**Conventional**	**Partial HTS**	**Full HTS**
Air gap current density J [A/m]	65000 [83]	65000 [83]	130000*
Magnet flux density B [T]	1.05	2.0 [46]	2.0 [46]
Additional parameters used for geometry and mass method according to Rucker [25]			
Magnet density $[kg/m^3]$	7400	6500	6500
Armature density $[kg/m^3]$	8900	8900	6500
Max. armature current density $[kg/m^3]$	$2.5 \cdot 10^6$	$2.5 \cdot 10^6$	$100 \cdot 10^6$
Number of slots	36	36	0 [78]
Slot fill factor	0.5	0.5	0 [78]
Slot depth [m]	0.025	0.025	0 [78]
Slot depression depth [m]	0.0005	0.0005	0 [78]
Slot depression width [m]	10^{-6}	10^{-6}	0 [78]
Peripheral tooth fraction	0.5	0.5	0 [78]
* based on a liquid water cooled stator according to Pyrhönen [83]			

Table A.3: Motor reference data for conventional electric motor with Permanent magnets at 45 kW and 1000 rpm according to [136]

Loss Type	Reference Loss [W]	Percentage [%]
Stator Core	32	1.1
Armature	1893	67.4
Stray Load	874	31.1
Windage and Friction	10	0.4

Table A.4: Motor reference data for a 1 MW partial HTS electric motor at 1800 rpm taken from [137]

Loss Type	Reference Loss [W]	Percentage [%]
Stator Core	11465	31.3
Armature[a]	12429	33.9
Stray Load[b]	1305	3.6
Windage and Friction[c]	1027	2.8
Miscellaneous	2953	8.0
Field Coil Cooling	7500	20.5

[a] for Full HTS motors armature losses set to zero

[b] for Full HTS motors stray load losses reduced by 50%

[c] for Full HTS motors nearly evacuated air gap assumed wit 1% of losses